Magnetism in Frustrated Nanostructures

A thesis presented for the

PhD degree of Imperial College London

and the

Diploma of Imperial College London (DIC)

by

Stephanie Katharine Walton

Department of Physics

Imperial College London

4TH AUGUST 2014

Except where specific reference has been made to the work of others, the work presented in this thesis is my own.

Stephanie Katharine Walton

COPYRIGHT

ABSTRACT

Artificial Spin Ice (ASI), comprised of ferromagnetic nanobars in a honeycomb geometry, attracts much attention since it is a directly imageable frustrated system which exhibits rich physics including ice-rule behaviour and magnetic monopole excitations. ASI's nanobars undergo domain wall mediated magnetic reversal in external fields. Understanding and indeed controlling the trajectories of field driven domain walls and hence the order in which ASI's nanobars are reversed is a crucial step towards mapping out ASI's full functionality for potential applications.

In this thesis, trajectories of domain walls during the early stages of ASI's magnetic reversal are studied. Data showing domain walls executing non-random walks in the transverse domain wall regime and random walks in the vortex domain wall regime is presented. The former behaviour is linked to the domain wall's chirality, and as such, attempts to control a domain wall's initial chirality via triangular injection pads are discussed. In addition, ways in which a vortex domain wall's chirality may be controlled with ellipsoidal hole obstructions are shown.

Artificial Dipolar 2D-XY, a complementary system to ASI, also promises interesting behaviour. In this new frustrated architecture, individual nanobars are replaced with single domain nanodiscs whose magnetisations can point in any in-plane direction. In this thesis, intriguing results from preliminary experiments on this new system are presented.

One of the best techniques used to study the magnetisations of nanostructures such as those described above is Lorentz Transmission Electron Microscopy (LTEM). Since the contrast yielded for unusual magnetic states was not well documented, software called Micromagnetic Analysis to Lorentz TEM Simulation (MALTS) was developed in order to aid in analysis of LTEM images. MALTS can simulate the LTEM contrast of any magnetic object of any size, shape or state. A description of its full functionality is also included in this thesis.

TABLE OF CONTENTS

LIST OF TABLES

LIST OF FIGURES

ACKNOWLEDGMENTS

First and foremost I would like to thank **Dr. Will Branford** for being an excellent supervisor with a truly encyclopaedic knowledge, and **Professor Lesley Cohen** for her inspirational leadership and advice. In addition I would also like to thank **Dr. Solveig Felton** for her help with MALTS and for being brilliantly proactive and efficient, **Dr. Katharina Zeissler** for her attention to detail in our collaborations and for being a great travelling companion, **Dr. Megha Chadha** for her superb sample fabrication and experimental work, and **Dr. Sam Ladak** and **Dr. Dan Read** for an incredibly fruitful trip to the Advanced Light Source.

Completing this thesis has been an enormous task and I am very grateful to **Dr. David Burn** and **Dr. Andrei Mihai** for reading it and providing such thoughtful and valuable feedback.

Outside my research group I would like to thank **Dr. David Ellis** for all his advice both mathematical and otherwise, **Dr. Ye Xiao** for all the lunches, bike rides and sweet breaks, **Freddie Page** for many lunches and for sharing his programming wisdom so readily, and my father, **Alastair Walton**, for providing a wonderful roof over my head for all these years. Where would I have been without you all?!

LIST OF PUBLICATIONS

Disorder-independent control of magnetic monopole defect population in artificial spin-ice honeycombs
S. Ladak, **S. K. Walton**, K. Zeissler, T. Tyliszczak, D. E. Read, W. R. Branford and L. F. Cohen
New Journal of Physics, Vol: 14, No. 4, 2012

The non-random walk of chiral magnetic charge carriers in artificial spin ice
K. Zeissler[†], **S. K. Walton**[†], S. Ladak, D E. Read, T. Tyliszczak, L. F. Cohen and W. R. Branford ([†]joint first authors)
Scientific Reports, Vol: 3, No. 1252, 2013

MALTS: A tool to simulate Lorentz Transmission Electron Microscopy from micromagnetic simulations
S. K. Walton, K. Zeissler, W. R. Branford and S. Felton
IEEE Transactions on Magnetics, Vol: 49, No. 8, 2013

SYNCHROTRON EXPERIMENTS

This thesis includes data from three synchrotron research trips. This data was acquired jointly with other members of the research team and with invaluable help and advice from the facility's beamline scientists.

Beamline 11.0.2 Advanced Light Source, June 2011
Scanning Transmission X-Ray Microscopy
Beamline Scientist: Dr. Tolek Tyliszczak
Research Team: Dr. Sam Ladak, Dr. Dan Read, Stephanie Walton and Dr. Katharina Zeissler

Beamline I06 Diamond Light Source, March 2012
Photo Electron Emission Microscopy
Beamline Scientists: Dr. Francesco Maccherozzi and Dr. Jorge Miguel
Research Team: Dr. Will Branford, Stephanie Walton and Dr. Katharina Zeissler

Beamline PolLux- X07DA Swiss Light Source, August 2013
Scanning Transmission X-Ray Microscopy
Beamline Scientists: Dr. Joerg Raabe and Dr. Ben Watts
Research Team: Dr. Will Branford, Dr. Solveig Felton, Stephanie Walton and Dr. Katharina Zeissler

CHAPTER 1 : INTRODUCTION AND THESIS OVERVIEW

Magnetism has fascinated and inspired mankind for many years, with the first reference to magnetism appearing in the 6^{th} century B.C.. Today magnetism, both innate and induced, is exploited in many different areas of life including cow rearing, transport, television and magnetic memory storage. Cassette and video tapes, both revolutionary advances in entertainment in the last century, stored data magnetically and today, credit cards and computer hard disc drives carry on the baton. Both the demand for smaller, higher density magnetic memory storage devices and the hunger for novel applications of magnetism drive a diverse field of research. The discovery of *Giant Magnetoresistance* by Fert and Grünberg in 1988 [1, 2] and its subsequent use in magnetic read heads led to both a significant increase in magnetic memory density and a Nobel Prize. A move towards *patterned magnetic media*, in which a bit of information is stored on a single patterned nanoisland as opposed to on a continuous grainy platter, also promises significant improvements [3]. As such, understanding the behaviour and controllability of different types of nanomagnetic arrays is one of today's big issues.

Artificial Kagome Spin Ice, an array of ferromagnetic nanobars in a honeycomb geometry, has attracted great interest since its first realisation in 2008 [4]. At each vertex three nanobars meet and are said to be *frustrated* because not all their dipolar interactions can be satisfied simultaneously. This directly imageable system provides a playground for studying frustrated effects and has already demonstrated rich physics including ice-rule behaviour [4], magnetic monopole defects [5] and hints of low temperature ordering [6]. In order to realise Artificial Spin Ice's full functionality, however, it is important to understand and, where possible, control its magnetic reversal. A study into the early stages of Artificial Spin Ice's field-driven domain wall reversal presented in this thesis provides a significant step forwards in this process.

Theoretically a complementary system to Artificial Spin Ice is *Artificial Dipolar 2D-XY* in which the ferromagnetic nanobars are replaced with ferromagnetic single domain nanodiscs. Currently there is some disagreement over which universality class Dipolar 2D-XY systems fall into and what type of behaviour they should demonstrate [7–10]. Preliminary investigations into Artificial Dipolar 2D-XY's behaviour presented in this thesis promise to start a much needed dialogue between experimentalists and theorists on this subject. As such, this work provides a necessary step forward towards mapping out Artificial Dipolar 2D-XY's functionality.

The work included in this thesis is ordered as follows: In **Chapter 2**, an overview of magnetism is presented with a particular emphasis on ferromagnetism and magnetic reversal. In addition, a brief introduction to Artificial Spin Ice is given. Investigative techniques, both experimental and simulational, used to study and analyse magnetic behaviour are subsequently described in **Chapter 3**. This leads directly into **Chapter 4** in which a new software called *MALTS*, which simulates expected Lorentz Transmission Electron phase contrast and aids in the analysis of experimental images, is presented. Next, experimental and simulated data showing field-driven domain wall propagation in Artificial Spin Ice is presented and analysed in **Chapter 5**. Since the study shown in this chapter suggests that the domain wall chirality plays an important role in the reversal of Artificial Spin Ice, the possibility of controlling domain wall chirality via triangular injection pads and ellipsoidal holes is discussed in **Chapter 6**. Then in **Chapter 7**, Artificial Dipolar 2D-XY, the new frustrated architecture comprised of nanodiscs in the single domain regime, is introduced. In addition, both preliminary simulated and experimental results are presented, the latter of which hint at interesting physics not yet understood. Finally, in **Chapter 8** the key results of the thesis are summarised and the future outlook is discussed.

CHAPTER 2 : MAGNETISM OVERVIEW

As discussed in the introduction, the work in this thesis focusses on investigating the behaviour of Artificial Spin Ice and Artificial Dipolar 2D-XY. Before entering into details of this work, however, it is important to understand their context within the field of magnetism as a whole.

Magnetism in materials arises due to either effects associated with isolated magnetic moments or interactions between different magnetic moments. In this chapter, an introduction to isolated magnetic effects, *diamagnetism* and *paramagnetism*, and collective magnetic effects, *ferromagnetism*, *antiferromagnetism* and *ferrimagnetism*, is provided. In addition, the behaviour of a ferromagnet is explained in detail by close consideration of its free energy. Furthermore, the formation of ferromagnetic domains and domain walls is discussed in depth and their role in magnetic reversal of thin nanobars is explored. This introduction to magnetism presented in this chapter has been written with reference to books by Stephen Blundell [11], J. Michael D. Coey [12] and David Jiles [13].

In the latter part of this chapter, the concept of *geometrical frustration* is presented. In particular, *Artificial Spin Ice*, a directly imageable array of monodomain nanobars in a honeycomb formation is introduced and its relation to both naturally occurring *Water Ice* and *Spin Ice* is discussed.

This chapter lays the necessary foundations for the novel work regarding the magnetic reversal of Artificial Spin Ice in Chapter 5, the control of domain wall chirality in Chapter 6 and the behaviour of Artificial Dipolar 2D-XY in Chapter 7.

2.1 What makes a material magnetic?

Electrons in atoms possess magnetic moments due to both their intrinsic spin and their orbital motion. (Nucleons also possess magnetic moments but these are negligibly small in comparison.) A material's atomic magnetic moment for a multi-electron atom depends on the exact configuration of its electrons. The spin and orbital components of each electron, which are goverened by quantum mechanics and simplified in Hund's rules, add vectorially (yielding S and L respectively). The total angular momentum of the atom, J, dependent on S and L, is in most cases zero leading to *diamagnetic* behaviour (see Section 2.2), with only a few transition metal atoms possessing resultant atomic moments. Typically these atomic moments macroscopically sum to zero in the absence of an applied field since they are disordered by thermal fluctuations. These materials are termed *paramagnets* (see Section 2.2). However in a small number of cases, namely for some 3d transition metals and 4d rare earth metals, collective ordering of atomic magnetic moments occurs in the absence of an external field, and a non-zero net magnetic moment may arise. This net magnetic moment per unit volume is termed its *magnetisation*, $\mathbf{M}$, and instances of spontaneous magnetisation are described in Section 2.3.

In order to differentiate between the different classes of magnetism described in the next sections it is useful to define the *magnetic susceptibility*, the degree to which a material's magnetisation, $\mathbf{M}$, responds to an applied magnetic field, $\mathbf{H}$. In a linear material, the magnetic susceptibility is a dimensionless constant, χ_m, defined as:

$$\mathbf{M} = \chi_m \mathbf{H}. \tag{2.1}$$

In a non-linear material, however, the susceptibility is not a constant but instead depends on the magnetisation, $\mathbf{M}$.

It is also useful to define the *permeability*, μ, of a material, which is the degree to which a material's magnetic flux density $\mathbf{B}$ responds to a magnetic field $\mathbf{H}$:

$$\mathbf{B} = \mu \mathbf{H}. \tag{2.2}$$

Since $\mathbf{B} = \mu_0(\mathbf{H} + \mathbf{M})$, in which μ_0 is the permeability of free space, a large susceptibility implies a large permeability and vice versa ($\mu = \mu_0(\chi_m + 1)$).

2.2 Diamagnetism and paramagnetism

Diamagnetism is the term used to describe a weak increase in a material's magnetisation in a direction opposite to an applied magnetic field i.e. a weak negative susceptibility. All materials exhibit this effect which is quantum mechanical in origin.

In materials with a net atomic magnetic moment, $\mathbf{J}$, other effects such as *paramagnetism* dominate over diamagnetism. In a paramagnetic material in zero external magnetic fields, non-zero atomic magnetic moments are distributed randomly due to thermal fluctuations. However, in the presence of an external magnetic flux density, $\mathbf{B}$, each magnetic moment, $\mathbf{m}$, has an associated potential energy, $U = -\mathbf{m}\cdot\mathbf{B}$, which is minimised when the magnetic moment is aligned with the external field. This gives rise to a positive susceptibility. In a *saturating* magnetic field, all the magnetic moments in a material are aligned and its saturation magnetisation, M_S, a property intrinsic to the material, is achieved.

Both diamagnetism and paramagnetism describe the net effect of many isolated magnetic moments. However, interactions between neighbouring moments are significant in some magnetic materials and must be considered in order to gain a more complete picture of a material's magnetism.

2.3 Collective magnetism: ferro-, antiferro-, ferri-magnetism

A *ferromagnet* is a material in which neighbouring atomic magnetic moments may spontaneously align with respect to each other (see Fig. 2.1 (a)). This can yield large macroscopic magnetisations in the absence of external magnetic fields. Conversely an *antiferromagnet* is a material in which neighbouring magnetic moments may spontaneously anti-align with respect to their nearest neighbours yielding no net macroscopic magnetisation (see Fig. 2.1 (b)). In *ferrimagnets*, like in antiferromagnets, neighbouring magnetic moments may spontaneously anti-align, however

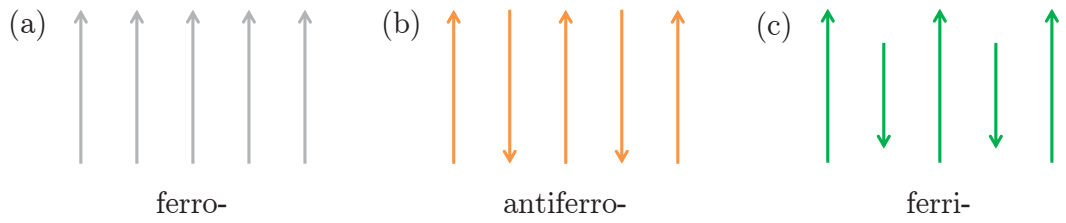

Figure 2.1: Schematic showing spontaneous ordering of magnetic moments in (a) ferro-, (b) antiferro- and (c) ferri- magnets.

a net macroscopic magnetisation may arise since the neighbouring moments are of different magnitudes (see Fig. 2.1 (c)). Since these three magnetic effects mentioned here depend on the orientation of neighbouring magnetic moments, they are said to be *collective magnetism* effects. These effects arise due to the *exchange interaction* which is described in detail in Section 2.4.1.

2.3.1 Ferromagnetic behaviour as a function of temperature

As mentioned above, ferromagnets exhibit spontaneous magnetic moment ordering in the absence of applied magnetic fields due to the exchange interaction. This ordering, however, may be reduced or destroyed by the presence of a thermal field due to finite temperature which acts to randomise the magnetic moments. If the ferromagnet's temperature is increased gradually from absolute zero in zero external field, its atomic magnetic moments experience increasing thermal agitation and the maximum possible time averaged macroscopic spontaneous magnetisation decreases. Eventually, at the material's *Curie Temperature*, the thermal effects dominate over the exchange interaction and the material starts to behave paramagnetically (see Section 2.2) as opposed to ferromagnetically. This is a reversible transition and on cooling back through the Curie Temperature the material starts to regain order. A schematic of a ferromagnet's magnetisation as a function of temperature is shown in Fig. 2.2

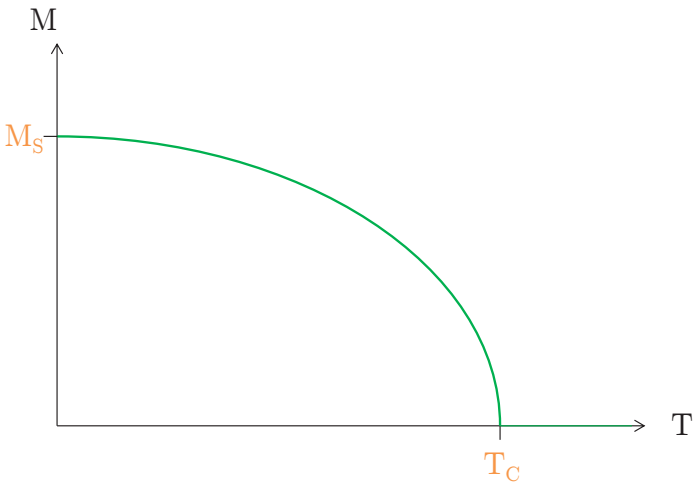

Figure 2.2: Schematic of a ferromagnet's spontaneous magnetisation as a function of temperature. At absolute zero temperature the saturation magnetisation may be achieved. As temperature is increased from absolute zero temperature, ordering is reduced until the Curie Temperature when all spontaneous ordering is lost.

2.4 Energy contributions

The different classes of magnetic materials described above emerge due to different sizes of atomic magnetic moments and different strengths of the interactions between neighbouring moments. The energetics of these interactions are now considered.

A system stabilises when its free energy is at a minimum. A material's total magnetic free energy depends on the magnitude of the *exchange*, *Zeeman*, *magnetocrystalline anisotropy*, *magnetostrictive* and *magnetostatic* energies [14, 15]:

$$E_{free} = E_{exchange} + E_{Zeeman} + E_{magnetocrystalline} + E_{magnetostriction} + E_{magnetostatic}. \quad (2.3)$$

The magnetic configuration a system supports depends on the interplay between each of these energy terms present in Eq. 2.3. The exact details of each of these energy contributions is described in detail below.

2.4.1 Exchange energy

The exchange interaction between two adjacent magnetic moments arises from Pauli's Exclusion Principle and the Coulomb Interaction. In a ferromagnet, this exchange interaction acts to align neighbouring atomic magnetic moments, minimising the exchange energy of the system. The energy cost associated with misalignment of spins can be computed by considering the total energy relating to exchange interactions:

$$E_{exchange} = \frac{A}{{M_S}^2} \int (\nabla M_x)^2 + (\nabla M_y)^2 + (\nabla M_z)^2 \, \mathrm{d}V, \tag{2.4}$$

in which A is the exchange stiffness constant (units Jm^{-1}) which is positive in ferromagnets and negative in antiferromagnets.

2.4.2 Zeeman energy

It is energetically favourable for a magnetic moment to align with an applied external magnetic field, $\mathbf{H}_{ext}$. The contribution to the total energy due to this is

$$E_{Zeeman} = -\mu_0 \int \mathbf{M} \cdot \mathbf{H}_{ext} \, \mathrm{d}V. \tag{2.5}$$

2.4.3 Magnetocrystalline anisotropy

In a magnetic crystal, there is a preference for the magnetisation to align parallel to certain crystallographic axes. This property is known as *magnetocrystalline anisotropy*. Magnetocrystalline anisotropy arises primarily from spin-orbit interactions due to anisotropic crystal-fields. The energy saving associated with the alignment of a magnetic moment with an anisotropic crystal's easy axis takes the form

$$E_{anisotropy} = -\frac{1}{M_S^2} \int K(\mathbf{n} \cdot \mathbf{M})^2 \, \mathrm{d}V, \tag{2.6}$$

in which K is the anisotropy constant (units Jm^{-3}), and $\mathbf{n}$ is a unit vector in the direction of the easy axis.

2.4.4 Magnetostriction

A crystal may deform in an external magnetic field in order to reduce its magnetocrystalline anisotropy energy. This effect is called *magnetostriction* and occurs when the saving in anisotropy energy outweighs the elastic energy cost associated with the change in shape.

The maximum magnetostriction in a given direction is defined as λ, the fractional change in length l in that direction: $\lambda = \mathrm{d}l/l$. λ is dimensionless but often expressed in terms of microstrains.

The nanostructures described in this thesis are grown on substrates with a different lattice parameter. This causes a non-uniform strain mismatch and hence a varying magnetostrictive response across the sample. This situation is far from ideal when trying to grow identical, homogeneous structures. The precise details of the energies relating to magnetostriction are complex, but it is suffice to say that materials with little to no magnetostriction are desirable in this situation.

2.4.5 Magnetostatic energy

Magnetostatic energy considerations are important for diverging magnetisations. Gauss's law for magnetism (Maxwell's second equation) states that $\nabla \cdot \mathbf{B} = 0$ in which $\mathbf{B}$ is the magnetic flux density. The magnetic flux density, $\mathbf{B}$, is related to the magnetisation, $\mathbf{M}$, the permeability of free space, μ_0, and the magnetic field strength, $\mathbf{H}$, by the constituent equation $\mathbf{B} = \mu_0(\mathbf{H} + \mathbf{M})$. Combining these two equations yields the following relationship:

$$\nabla \cdot \mathbf{M} = -\nabla \cdot \mathbf{H}, \tag{2.7}$$

i.e. a diverging magnetisation, $\mathbf{M}$, produces diverging demagnetising fields, $\mathbf{H}_{demag}$. These demagnetising fields cost energy. This is termed either the *magnetostatic* or the *demagnetisation energy* and takes the form

$$E_{magnetostatic} = -\frac{\mu_0}{2} \int \mathbf{M} \cdot \mathbf{H}_{demag} \, \mathrm{d}V. \tag{2.8}$$

This magnetostatic energy can be reduced by the formation of magnetic domains (see Section 2.6).

2.5 Shape anisotropy

In the previous section, the different energy terms affecting the magnetic state supported by a structure were discussed in detail. In particular, the magnetostatic energy was introduced which relates to diverging and hence discontinuous magnetisations. If a nanostructure is non-spherical in shape, its magnetostatic energy then depends on its direction of magnetisation. The structure is then said to exhibit *shape anisotropy* and has an axis or axes of preferential alignment. This is illustrated in Fig. 2.3 for the case of a nanobar with a large aspect ratio. Fig. 2.3 (a) & (b) show states with low and high magnetostatic energy respectively. As such the state shown in (a) is favoured over the state shown in (b).

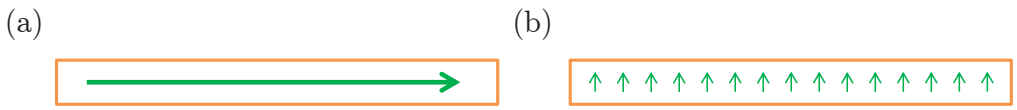

Figure 2.3: Schematic showing the shape anisotropy in a nanobar of large aspect ratio. (a) shows the magnetisation pointing along the long axis, a favourable state of low magnetostatic energy and (b) shows the magnetisation pointing perpendicular to the long axis, an unfavourable state since there is a large associated magnetostatic energy.

2.6 Magnetic domains and domain walls

As described in Section 2.4, a system stabilises when its total energy (Eq. 2.3) is at a minimum. In order to minimise its magnetostatic energy specifically, a ferromagnet may break up into multiple *magnetic domains* (see Fig. 2.4). In the rest of this thesis these *magnetic domains* will be referred to simply as *domains*. A domain is a region of magnetisation in which all adjacent magnetic moments are aligned.

In adjacent domains, however, magnetisations point in different directions, with the region between two neighbouring domains termed a *domain wall*. An abrupt change in magnetisation direction incurs a large exchange penalty so in the domain wall region the magnetic moments are rotated gradually with respect to each other. The net rotation achieved in the domain wall corresponds to the difference in magnetisation direction between the adjacent domains.

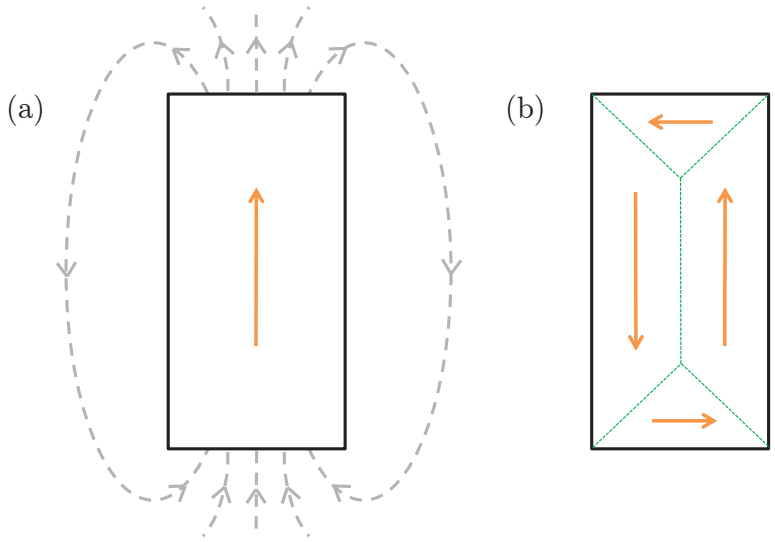

Figure 2.4: Schematic showing (a) a single domain state and (b) a four-domain flux-closure state with four 90° and one 180° domain walls shown with dotted green lines. The grey dashed lines in (a) represent the stray field due to a collinearly magnetised ferromagnet. The energy associated with this field is large so a ferromagnet may break up into multiple domains like in (b) in order to minimise its magnetostatic energy.

The type of domain wall supported by a structure is dictated by the relative energy terms described in Section 2.4. These energy terms depend on both the material's properties and its dimensions. The following discussion considers systems with negligible out-of-plane magnetocrystalline anisotropy and predominantly in-plane magnetisation. Bloch domain walls are supported in thick ferromagnets with large lateral dimensions. Here the magnetisation rotates in the same plane as that of the domain wall (see Fig. 2.5 (a) i)) and far away from the sample's edges, the magnetisation

is divergenceless. There is however a small magnetostatic energy cost at the edges associated with rotation out of the plane of the sample. In thinner structures of larger lateral dimensions, this magnetostatic energy cost associated with rotation out of the plane of the sample contributes a relatively large energy penalty to the total free energy of the sample and hence the Bloch domain wall is untenable. Instead Néel domain walls are supported. Here the magnetisation rotates in the plane perpendicular to that of the domain wall (see Fig. 2.5 (a) ii)).

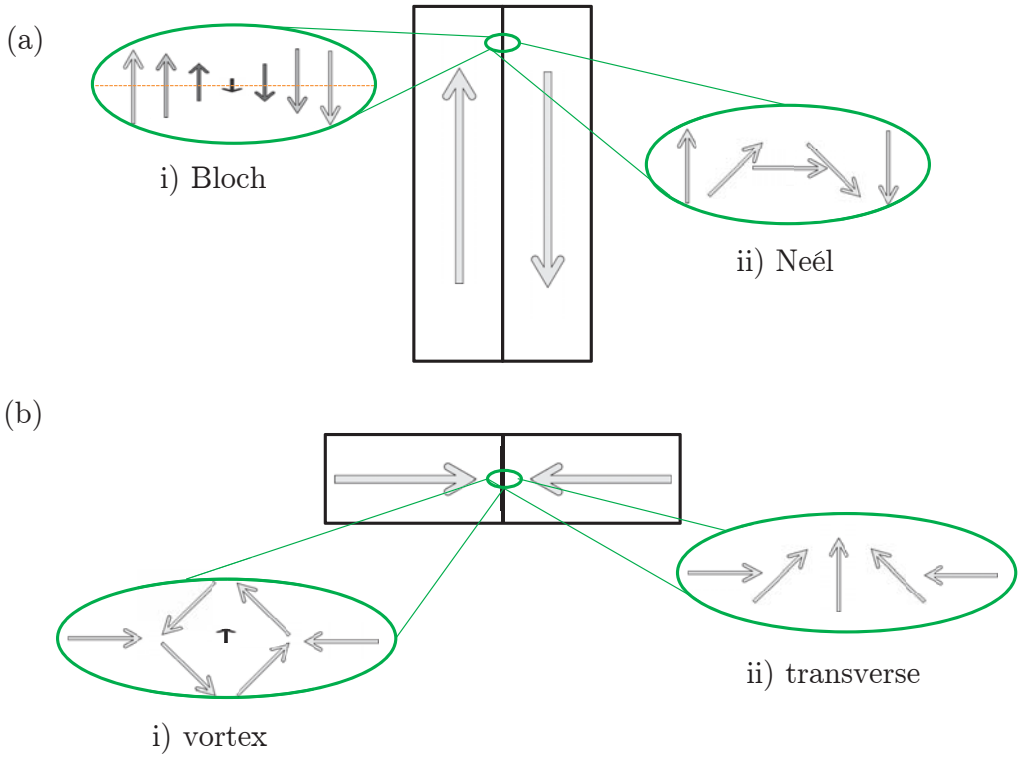

Figure 2.5: Schematic showing (a) a 180° i) Bloch domain wall in which the magnetisation rotates in the same plane as that of the domain wall, ii) Néel domain wall in which the magnetisation rotates in a plane perpendicular to that of the domain wall and (b) a 180° head-to-head i) vortex domain wall in which the magnetisation swirls around a vortex core, ii) transverse domain wall in which the magnetisation rotates in a plane perpendicular to that of the domain wall.

In thin structures of small lateral dimensions and large aspect ratio, transient or stable *head-to-head* (see Fig. 2.5 (b)) or *tail-to-tail* domain walls may be supported

in which the magnetisation points inward towards the domain wall or outwards from the domain wall respectively. Domain walls of this type may be *transverse* or *vortex*. Like in a Néel domain wall, the transverse domain wall's magnetisation rotates in the plane perpendicular to that of the domain wall (see Fig. 2.5 (b) ii)). Here there is a significant magnetostatic energy cost associated with magnetisation perpendicular to the edges. In vortex domain walls, however, this effect is reduced since the magnetisation swirls around a vortex core (see Fig. 2.5 (b) i)). There is however both a large exchange energy penalty associated with the swirling of the vortex core and magnetostatic energy associated with the core's out-of-plane magnetisation. Whether a vortex or a transverse domain wall is stabilised depends on the dimensions of the structure and on the material. Transverse domain walls are seen in narrower thinner structures and vortex domain walls in wider thicker structures [16, 17].

2.6.1 Domain wall chirality

A structure is said to be *chiral* if it cannot be superposed onto its mirror image. This is the case for both transverse and vortex domain wall structures on substrates. Therefore the two possible senses of rotation of the magnetic moments in these walls are termed *chiralities*. These two different possible chiralities for each domain wall type are degenerate in energy in the absence of an externally applied magnetic field. The transverse domain wall demonstrates an up or down chirality as illustrated in Fig. 2.6 (a). The vortex domain wall demonstrates a clockwise or anticlockwise chirality corresponding to the direction of swirling of its magnetisation. This is illustrated in Fig. 2.6 (b). In addition the vortex core can point in two different out-of-plane directions, up or down. This is called the *polarity* of the vortex domain wall.

2.7 Magnetic reversal

The magnetisation configuration supported by a material changes in an externally applied magnetic field or a sufficient thermal field. The terms *switching* and *reversal* are used to describe the process by which a structure's magnetisation direction is gradually altered from pointing in one direction (e.g. $+x$ direction) to pointing in the

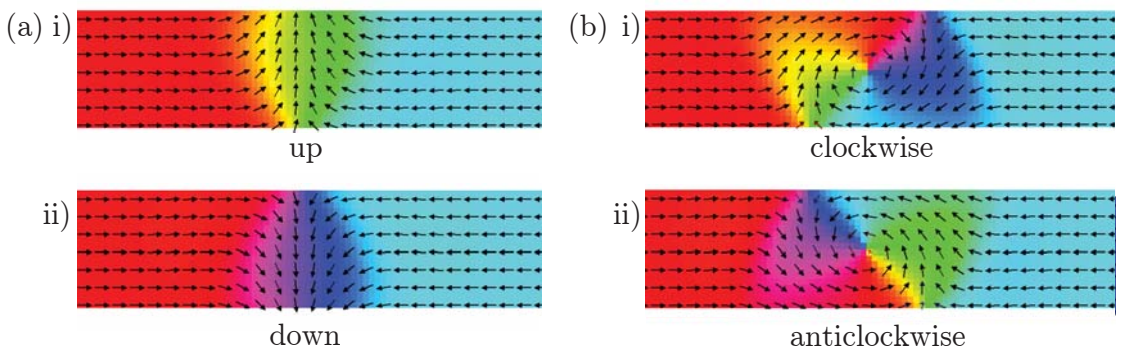

Figure 2.6: Micromagnetic simulations (see Section 3.3) showing (a) transverse i) up chirality and ii) down chirality and (b) vortex i) clockwise chirality and ii) anticlockwise chirality head-to-head domain walls. The simulations were performed using the OOMMF software [18] for permalloy with mesh size [5 nm, 5 nm, 10 nm], dimensions 1 µm × 100 nm × 10 nm and 1 µm × 100 nm × 40 nm for (a) and (b) respectively.

diametrically opposite direction (e.g. $-x$ direction). Switching, which is material and size dependent, can occur by two different mechanisms, coherent rotation and domain wall propagation. These two mechanisms are discussed in detail in the following sections.

2.7.1 Coherent rotation

If a material's magnetisation coherently rotates, the magnetic moments inside the sample retain the same alignment with respect to each other, whilst the macroscopic magnetisation rotates with respect to its environment (see Fig. 2.7 (a)). This method of switching is usually seen in samples which are too small to support domain walls [19] such as the single domain nanodiscs described in Chapter 7. The nanobars described in Chapters 5 & 6, however, do not undergo coherent rotation as there is too great a magnetostatic energy cost associated with magnetisation perpendicular to the nanobars' long axis. Instead they undergo reversal by domain wall propagation described in the next section.

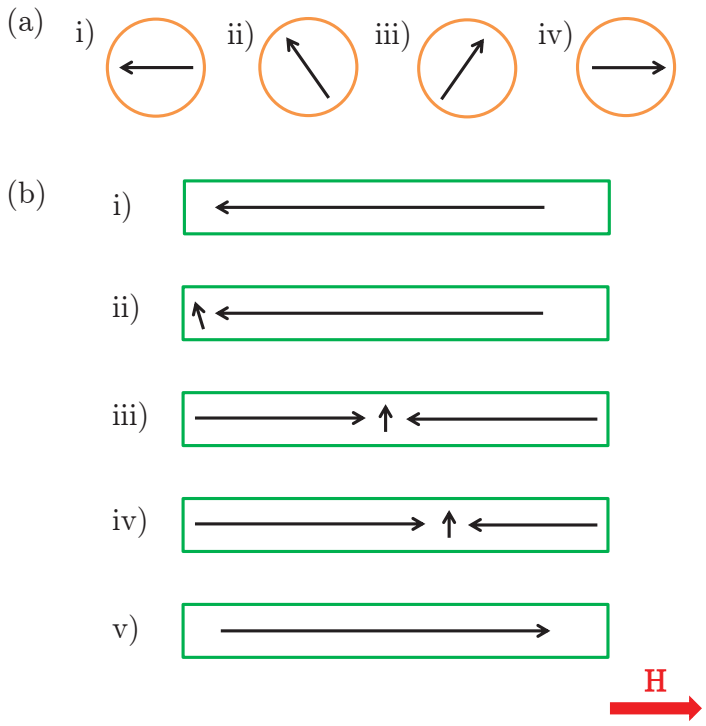

Figure 2.7: Magnetic reversal schematic showing (a) coherent rotation and (b) domain wall nucleation and propagation in the presence of an external magnetic field in the $+x$ direction. (a) i) & (b) i) show the initial magnetisation states and (a) iv) & (b) v) show the final magnetisation states after reversal.

2.7.2 Domain wall propagation and Walker Breakdown

For structures large enough to support domain walls, switching occurs by domain wall propagation (see Fig. 2.7 (b)). During domain wall propagation, the volume of magnetisation aligned most favourably with the external magnetic field grows at the expense of the volume of magnetisation on the other side of the domain wall, reducing the overall Zeeman energy. Microscopically, each magnetic moment experiences damped precessional motion around the combined externally applied field and local field direction (see Section 3.3.1). As the moments in the domain wall gradually align with the external field, some of them cease to be part of the domain wall and others on the other side join, hence the domain wall moves. It is this kind of switching behaviour that occurs in the nanobars described in Chapters 5 & 6.

If the domain wall propagates in the presence of a low external magnetic field its shape is slightly distorted but its chirality is maintained. However above a certain threshold, the *Walker Field*, H_W, the domain wall may suffer *Walker Breakdown* [20]. Here the domain wall structure becomes unstable and its chirality can change during propagation e.g. changes from up chirality to down chirality for transverse domain walls. Both the Walker Field and the frequency of Walker Breakdown depend on the dimensions and material parameters. Walker Breakdown is treated in more detail in Chapter 5.

The domain wall propagation described above may involve either a pre-existing domain wall or a *nucleated* domain wall. A domain wall may be nucleated either at the edge of a structure in an external magnetic field, or at the interface between the structure and an *injection pad* in a smaller external magnetic field, or near a current carrying wire. Domain wall nucleation and injection in Artificial Spin Ice is discussed in more detail in Chapters 5 & 6.

2.7.2.1 Pinning

A domain wall may become *pinned* during magnetic reversal if it encounters a change in energy landscape which increases the field at which it can propagate locally. A pinned domain wall is stationary occupying a local energy minima and can only resume propagation in the presence of a larger external magnetic field. Pinning may arise due to defects or geometrical constrictions, artificial [21–27] or otherwise.

2.8 Magnetic hysteresis

As discussed in Section 2.7, a structure's magnetic state may be altered in the presence of an external magnetic field. Ferromagnets are said to be *hysteretic* because the magnetic states they support depend on the external magnetic field history. For example, if a ferromagnet is magnetised in the $+x$ direction to saturation and then the external magnetic field is removed, the ferromagnet retains a remanent magnetisation in the $+x$ direction. Conversely, if the ferromagnet is magnetised in the $-x$ direction to saturation and the external magnetic field is removed, the ferromagnet's

remanent magnetisation is in the $-x$ direction i.e. the state of the system depends on its history. Hysteresis arises due to a ferromagnet's inability to access other potentially more energetically favourable states due to its complex energy landscape. Fig. 2.8 illustrates magnetic hysteresis in the context of the saturation magnetisation, M_S, the maximum magnetisation achievable under high fields, the remanent magnetisation, M_R, the magnetisation that remains after saturation on removal of the external magnetic field, and the coercive field, H_C, the magnitude of external magnetic field in the direction opposite to saturation required to demagnetise the system.

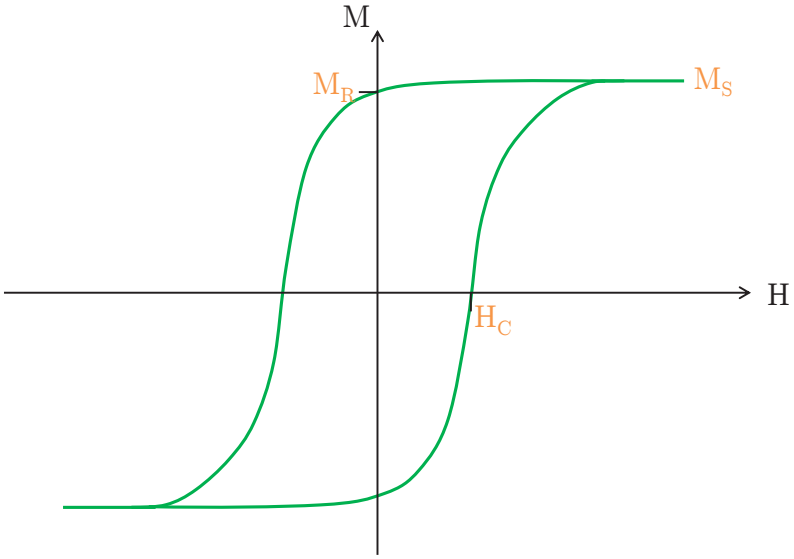

Figure 2.8: Schematic of a hysteresis loop of a typical ferromagnet showing the magnitude of the net magnetisation, M, along the same axis as an externally applied magnetic field, H. M_S, M_R and H_C correspond to the saturation magnetisation, remanent magnetisation and coercive field respectively.

The magnitude of the coercive field, H_C, reflects how readily a structure is demagnetised. If a structure is anisotropic due to its shape or crystal structure, its coercivity is dependent on the direction of the externally applied magnetic field, **H**, and is maximal when **H** is aligned along the easy axis of magnetisation. Materials which have a high coercivity are said to be *hard* and are not easily demagnetised. Most materials, however, are naturally *soft*, that is they are demagnetised in low external magnetic fields and hence have small coercivities. For the experiments described in

this thesis, a soft material is desirable so that field driven dynamics can be achieved with small laboratory external magnetic fields. Bulk permalloy, described in the next section, has a coercivity of 0.05 Oe [13] and as such is a suitable candidate for these experiments.

2.9 Permalloy

Alloys of approximately 80% nickel and 20% iron have a very high permeability (see Eq. 2.2) in low external field and as such are termed *permalloy* [28, 29]. The experiments in this thesis were conducted on permalloy at room temperature (293 K). Since permalloy's Curie Temperature is 843 K, these experiments were performed well within permalloy's regime of ferromagnetic behaviour. Permalloy is an ideal candidate for nanostructuring; its near zero magnetocrystalline anisotropy and magnetostriction together ensure that the physics is governed by the shape and not the intrinsic anisotropies of the material. Permalloy's material parameters are summarised in Table 2.1.

Saturation Magnetisation (M_S)	$830\,\mathrm{kAm^{-1}}$ [1]
Exchange Stiffness Constant (A)	$10\,\mathrm{pJm^{-1}}$ [1]
Magnetocrystalline Anisotropy (K)	$-1\,\mathrm{kJm^{-3}}$ [1]
Magnetostriction (λ)	2 μstrains [1]
Curie Temperature (T_C)	843 K [1]
Bulk Coercivity (H_C)	0.05 Oe [2]

Table 2.1: Material properties of permalloy [1] $Ni_{80}Fe_{20}$ taken from [12] and [2] $Ni_{78}Fe_{22}$ taken from [13].

2.10 Frustration and Spin Ice

In Section 2.4, many different types of magnetic interaction were introduced. If not all a system's interactions of a specific kind can be satisfied simultaneously due to geometrical constraints, the system is said to be *geometrically frustrated*. Geometrically

frustrated systems demonstrate unusual behaviour, in some cases having degenerate groundstates that scale with the system size.

In the following sections three geometrically frustrated systems namely Water Ice, Natural Spin Ice and Artificial Spin Ice are introduced and the relationship between these systems is articulated.

2.10.1 Water Ice

Water Ice (H_2O) is a frustrated system in which there is a mismatch between the crystal symmetry and the desired bonding in a water molecule [30]. The system obeys a set of lowest energy *ice rules* in which two protons sit near to the oxide ion and two protons sit far away (see Fig. 2.9 (a)). This low energy state can be achieved with six different degenerate configurations [31]. Each oxide ion is tetrahedrally coordinated with four neighbouring oxides and the degeneracy of the groundstate scales with the system size.

2.10.2 Natural Spin Ice

In *Natural Spin Ice* materials (e.g. $Ho_2Ti_2O_7$ and $Dy_2Ti_2O_7$) the magnetic moments' frustration (due to exchange and dipole-dipole interactions) at very low temperatures mimics the behaviour of proton disorder in Water Ice [30] (see Fig. 2.9 (b) and (c)). Since these natural materials only exhibit Spin Ice behaviour at temperatures of order 2 K and atomic magnetic moments due to the magnetic cations Ho^{3+} or Dy^{3+} are too small to image individually, it is hard to study them experimentally. Despite this however, Natural Spin Ices have been shown experimentally to exhibit residual entropy [31] and to support magnetic monopole excitations which are free to move within the lattice [32–35].

2.10.3 Artificial Spin Ice

In order to better understand Natural Spin Ice's frustration, much larger artificially fabricated structures called *Artificial Spin Ices* in which imageable magnetic nano-

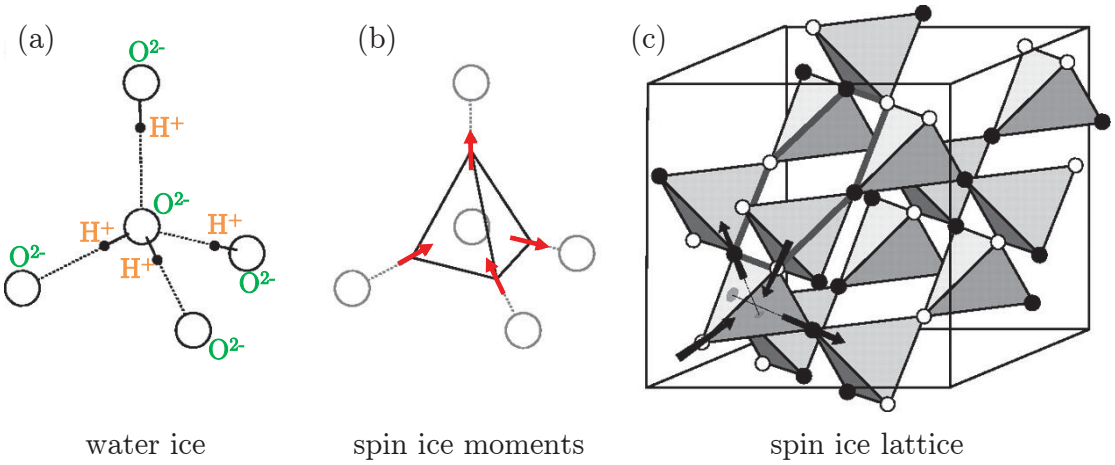

Figure 2.9: Schematic showing the relationship between Water Ice and Natural Spin Ice. This caption and figure have been adapted from Bramwell and Gingras' Figure 1 [30] and is reprinted with permission from AAAS and the authors. (a) the proton arrangement in Water Ice showing oxide ions and protons. An ice rule obeying state of two-near and two-far is shown. (b) the magnetic moment arrangement in Natural Spin Ice. Protons have been replaced with red displacement vectors located at the midpoints of the oxide-oxide lines of contact. This system obeys the ice rules of two-in one-out. (c) lattice as occupied by the magnetic rare-earth ions Ho^{3+} or Dy^{3+} in Natural Spin Ice materials. White and black denote a spin pointing into and out of a tetrahedron respectively. The entire lattice is ice-rule obeying (two black and two white sites for every tetrahedron).

bars in the single domain regime replace atomic magnetic moments have been studied. Since Artificial Spin Ice's nanobars contain many atomic magnetic moments, effects of temperature are less significant than in Natural Spin Ices and hence the system can be studied at room temperature [36]. Two different architectures of Artificial Spin Ice, *Artificial Square* [37, 38] and *Artificial Kagome* [4, 5, 39, 40] *Spin Ice* (see Fig. 2.10), exist which both share similarities with Natural Spin Ice's tetrahedral frustrated lattice. The square lattice, like Natural Spin Ice, has four magnetic moments interacting at each vertex. However, unlike Natural Spin Ice, it has a single groundstate and is therefore not truly ice-like. Conversely the kagome lattice has only three interacting magnetic moments at a vertex, and hence a net magnetostatic charge at each vertex. However, like Natural Spin Ice, each vertex is frustrated due to competing dipole-dipole interactions (the exact details of which are given later in

Eq. 7.6) giving rise to a degenerate groundstate. Since ice behaviour is of primary interest in this work, the Artificial Kagome Spin Ice lattice has been studied. In the rest of this thesis Artificial Kagome Spin Ice is referred to simply as *Artificial Spin Ice* or abbreviated to *ASI*.

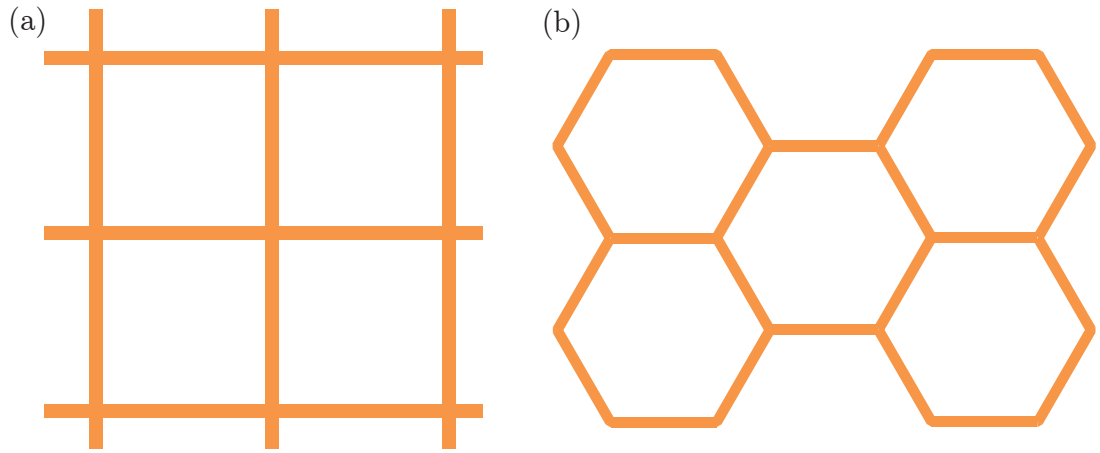

Figure 2.10: Schematic showing sections of joined Artificial (a) Square and (b) Kagome Spin Ices. Orange indicates magnetic material, white indicates empty space.

In ASI, each vertex of three nanobars is frustrated and these vertices are governed by their own set of ice rules: two-in one-out or two-out one-in [36] (see Fig. 2.11 (a) & (b)). These configurations are each three fold degenerate. Ice rule violating vertices of three-in or three-out (see Fig. 2.11 (c) & (d)) are excitations of the system and termed either *defects* or *monopoles*. It is stressed that these monopoles are sources or sinks of magnetic field strength, $\mathbf{H}$, not magnetic flux density, $\mathbf{B}$, so are neither analogous to free electric charges nor in conflict with Maxwell's Equation $\nabla \cdot \mathbf{B} = 0$.

If the spin-ice rules were the only rules that governed the lattice, the degeneracy of the groundstate would increase rapidly with the system size. However, long range dipolar interactions have been observed giving rise to two models to describe ASI; the short-range dipolar Spin Ice model in which only nearest neighbour dipolar interactions are considered, and the long-range dipolar Spin Ice model in which longer range terms are of significance [6, 39–41].

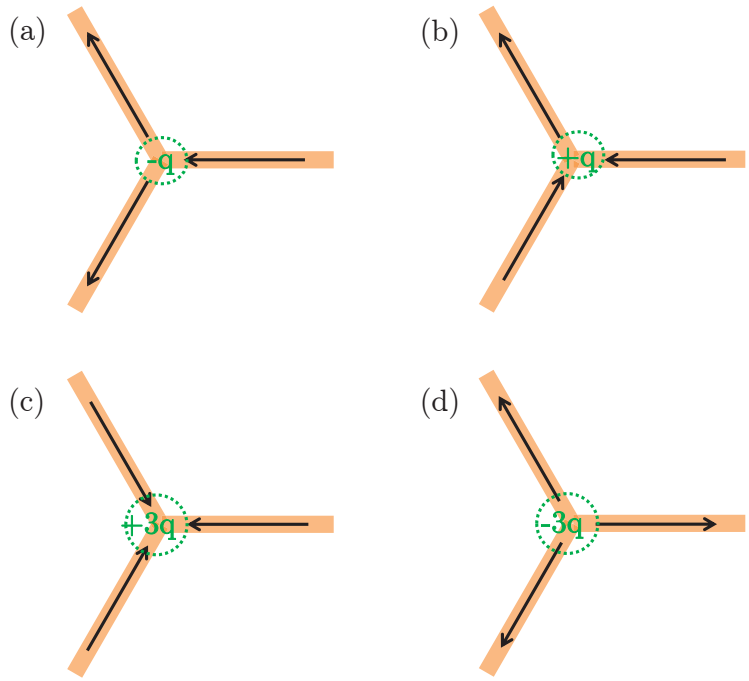

Figure 2.11: Schematic of magnetisation configurations in a single ASI vertex (a) & (b) ice-rule obeying states two-out and one-in, and two-in and one-out respectively and (c) & (d) monopole defect states, three-in and three-out respectively. Here the magnetic dipole of a nanobar is treated as a dumbbell of magnetic charge. The magnitude of both positive and negative charges in this dumbbell model, q, is determined by the magnitude of the magnetic moment of a single nanobar divided by its length. The total magnetic charge at each vertex is shown in green.

In naturally occurring Spin Ices such as those described in Section 2.10.2, the energy required to switch the magnetisation direction of a single magnetic moment is within the reaches of the thermal energy present, k_BT. As such, Natural Spin Ices can eventually reach thermal equilibrium and a groundstate. This is called *thermalisation*. In ASI, however, there are many more magnetic moments to switch in a single bar, and the energy required to switch these nanobars scales with the volume of the system. As a result, at room temperatures, the thermal energy k_BT is small compared with the energy barriers involved in switching, and the system remains static with respect to its magnetisation configuration. In order to introduce dynamics into the system, an external magnetic field must be applied prompting the nucleation and subsequent

propagation of domain walls (see Section 2.7.2).

The two different designs of ASI involving either connected (e.g. [5]) or isolated (e.g. [42]) nanobars show surprisingly similar domain wall mediated magnetic reversal behaviour. However, since electric transport measurements of interest to the research group but not described in this thesis cannot be performed on isolated structures, the connected ASI design was employed. The magnetic reversal behaviour of this connected ASI is studied in detail in Chapter 5.

2.10.3.1 Modelling nanobar coercivities in Artificial Spin Ice

A simple magnetic charge model may be used to study the field-driven domain wall mediated magnetic reversal of ASI [36, 43, 44]. In this model the magnetic charge at an ice rule obeying vertex and an ice rule violating vertex corresponds to $\pm 1q$ and $\pm 3q$ respectively, in which q is the magnetisation of a single nanobar divided by its length. In addition, the domain walls which mediate magnetic reversal are assumed to be discs of characteristic size a and of charge $+2q$ for head-to-head domain walls and charge $-2q$ for tail-to-tail domain walls (see Fig. 2.12).

In order for a nanobar in ASI to magnetically reverse, a domain wall must be nucleated and depinned. Both the domain wall type and the ease with which it is nucleated and depinned depend on the magnetic charge at its two adjacent vertices, q_1 and q_2. For nanobars in the centre of the lattice with four adjacent nanobars, there are nine possible permutations of q_1 and q_2. For edge nanobars which have only three adjacent nanobars, there are six possible permutations of q_1 and q_2. And for nanobars which have only two nearest neighbours there are four possible permutations of q_1 and q_2. These different situations are all shown at the end of this chapter in Figs. 2.13, 2.14, 2.15 & 2.16. If the nucleated domain wall and the *site charge* left behind ($q_{site} = q_1 - 2q$ or $q_{site} = q_2 + 2q$) are of the same charge, they experience Coulombic repulsion and may separate at low external magnetic fields. However, a larger external magnetic field is required to separate the nucleated domain wall from the site charge if they are of opposite magnetic charges. The magnitude of the fields corresponding to these Coulombic interactions may be estimated [36, 43, 44]. The Coulombic force

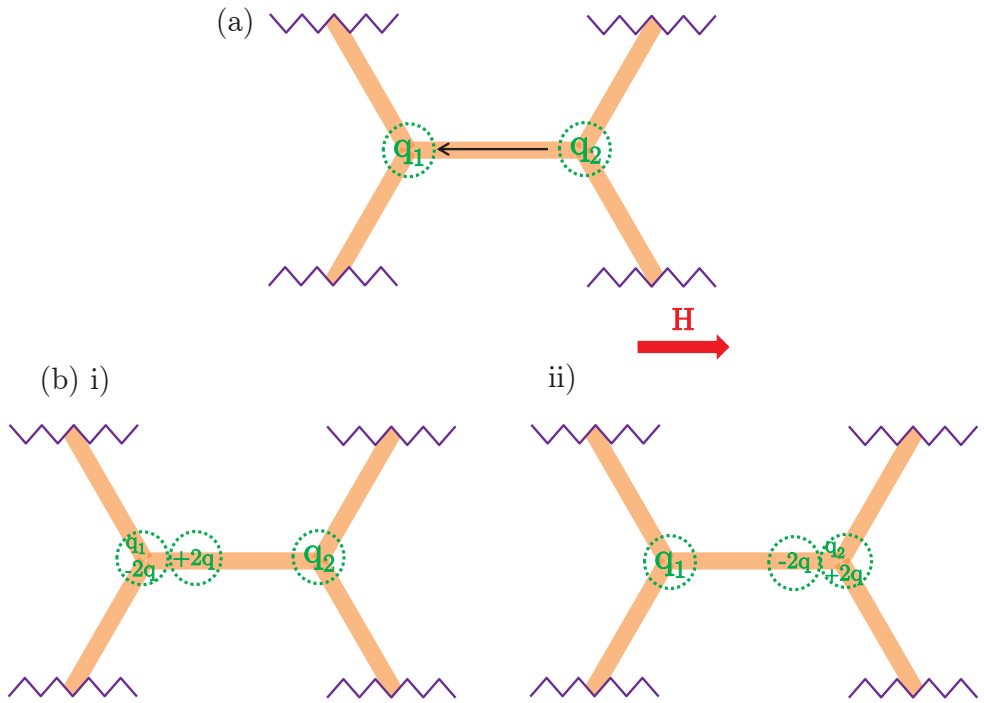

Figure 2.12: Schematic showing the nucleation of domain walls in ASI in the simple charge model. (a) shows the definitions of q_1 and q_2. (b) i) shows the nucleation of a head-to-head domain wall of charge $+2q$ and ii) shows the nucleation of a tail-to-tail domain wall of $-2q$. A head-to-head domain wall may mediate reversal if $q_1 + q_2 > 0$ and a tail-to-tail domain wall may mediate reversal if $q_1 + q_2 < 0$. If $q_1 + q_2 = 0$, the nucleation of a head-to-head and a tail-to-tail domain wall are equally likely.

between the domain wall and the site charge is $F \approx \mu_0 q_{site} q_{DW}/(4\pi r^2)$ at separations r exceeding the characteristic size of the charges a. The maximum force occurs when the charges are exactly touching but not merged i.e. at $F_{max} \approx \mu_0 q_{site} q_{DW}/(4\pi a^2)$. The force that the domain wall experiences due to the external field, H, is $\mu_0 q_{DW} H$. Therefore the magnitude of the component of the external field, H, required for the domain wall to overcome Coulombic attraction is:

$$H_{charge} = \frac{|q_{site}|}{4\pi a^2} = \frac{N M_S t w}{4\pi a^2}, \tag{2.9}$$

in which M_S is the saturation magnetisation of the nanobar and t and w are the

thickness and width. N is defined as $N = |q_{site}|/q$ in which q_{site} is the site charge left behind after domain wall nucleation and q is the magnetic moment of a single nanobar divided by its length.

Domain wall mediated reversal may start at either vertex 1 with charge q_1 or vertex 2 with charge q_2 corresponding to the preferential emission of a head-to-head or a tail-to-tail domain wall respectively. If either of the vertices is repulsive i.e. $q_1 = +3q$ (yielding $q_{site} = +1q$ and $q_{DW} = +2q$) or $q_2 = -3q$ (yielding $q_{site} = -1q$ and $q_{DW} = -2q$), reversal proceeds from this vertex. If one of the vertices is neutral i.e. if $q_1 = +2q$ (yielding $q_{site} = 0q$ and $q_{DW} = +2q$) or if $q_2 = -2q$ (yielding $q_{site} = 0q$ and $q_{DW} = -2q$) and the other is attractive, reversal is mediated from the neutral vertex. If both vertices are attractive, i.e. $q_1 < +2q$ and $q_2 > -2q$, then Equation 2.9 must be considered at both vertices; domain wall mediated reversal will proceed from the side with the smallest $|q_{site}|$ i.e. if $q_1 - 2q < q_2 + 2q$, then head-to-head reversal from vertex 1 will occur and if $q_1 - 2q > q_2 + 2q$, then tail-to-tail reversal from vertex 2 will occur. If both vertices are repulsive or neutral or attractive with the same value of $|q_{site}|$ then reversal proceeds from either vertex with equal likelihood. The types of domain walls emitted for different permutations of q_1 and q_2 and, where necessary, the corresponding values of $N = |q_{site}|/q$ are detailed in Tables 2.2, 2.3, 2.4 & 2.5.

Minor imperfections inherent from sample fabrication lead to small variations in the size and homogeneity of each nanobar giving rise to different degrees of pinning. This *quenched disorder* is usually uncorrelated across the ASI array. Incorporating the effects of local charges and quenched disorder, each nanobar's coercivity may be described as:

$$H_c = \frac{H_{charge} + H_{quenched}}{\cos\theta}, \tag{2.10}$$

in which H_{charge} is the magnetic field associated with magnetic charges, $H_{quenched}$ accounts for the quenched disorder in the sample and θ is the angle of the nanobar from the external magnetic field direction.

The coercivities of each nanobar in an ASI lattice have been modelled above. The model is successful in describing some features of ASI's reversal such as the presence of cascades in the early stages of reversal, as discussed in Chapter 5. However, since

it does not consider other important interactions such as those detailed in Section 2.4, the exact coercivities it predicts can be quantitatively inaccurate. This limitation is most prominent at the edges where the model predicts zero coercivities for nanobars next to neutral vertices, a feature not seen experimentally.

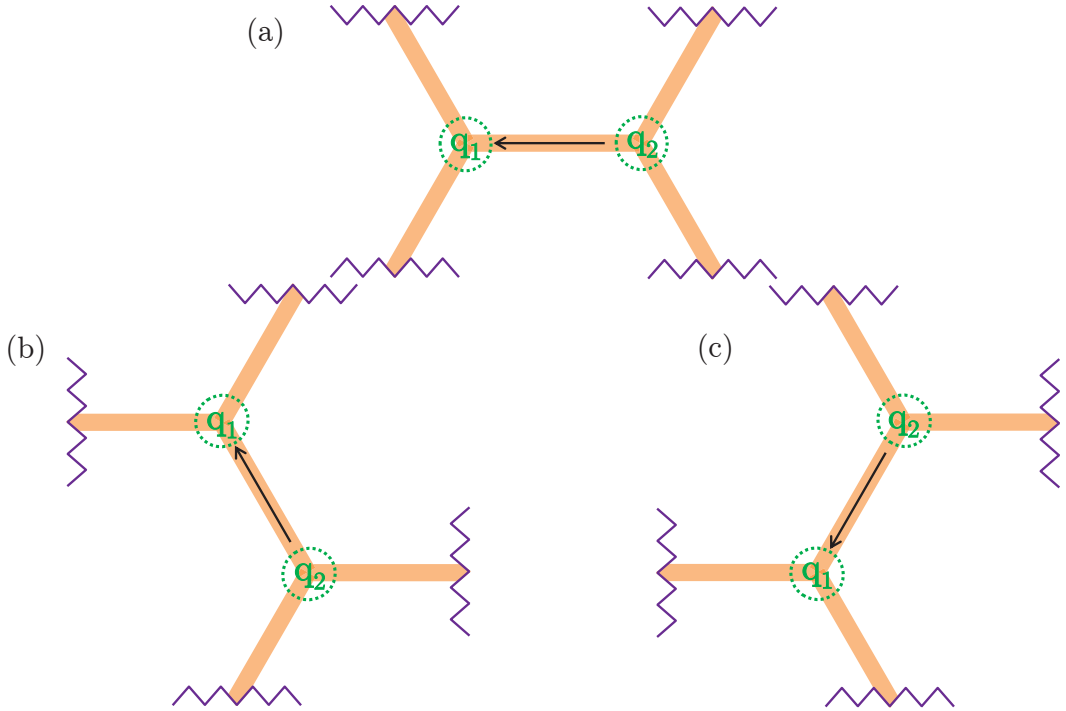

Figure 2.13: Schematic showing central nanobars which have four adjacent nanobars, two on their right hand side and two on their left. Their behaviour is described in Table 2.2.

q_1/q	q_2/q	vertex (v) types & (N)	DW type emitted
+3	+1	v1 repulsive	head-to-head
+3	−1	v1 repulsive	head-to-head
+3	−3	v1 and v2 repulsive	either
+1	+1	attractive (1)	head-to-head
+1	−1	attractive (1)	either
+1	−3	v2 repulsive	tail-to-tail
−1	+1	attractive (3)	either
−1	−1	attractive (1)	tail-to-tail
−1	−3	v2 repulsive	tail-to-tail

Table 2.2: The possible q_1 and q_2 permutations for central nanobars which have four adjacent nanobars, two on their right hand side and two on their left such as those shown in Fig. 2.13. The vertex and emitted domain wall types and, where necessary, the values of $N = |q_{site}|/q$ are shown for all nine different permutations.

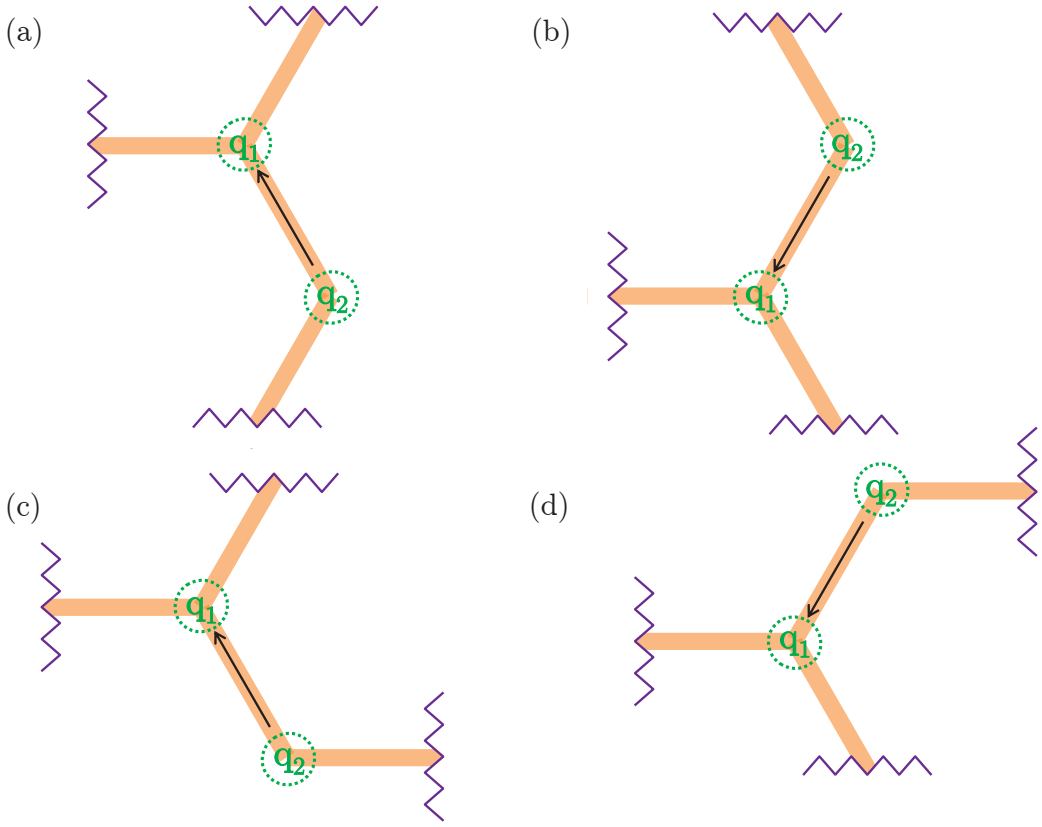

Figure 2.14: Schematic showing edge nanobars which have only three adjacent nanobars, one on their right hand side and two on their left. Their behaviour is described in Table 2.3.

q_1/q	q_2/q	vertex (v) types & (N)	DW type emitted
+3	0	v1 repulsive	head-to-head
+3	−2	v1 repulsive	head-to-head
+1	0	attractive (1)	head-to-head
+1	−2	v2 neutral	tail-to-tail
−1	0	attractive (2)	tail-to-tail
−1	−2	v2 neutral	tail-to-tail

Table 2.3: The possible q_1 and q_2 permutations for edge nanobars which have only three adjacent nanobars, two on their left hand side and one on their right such as those shown in Fig. 2.14. The vertex and emitted domain wall types and, where necessary, the values of $N = |q_{site}|/q$ are shown for all six different permutations.

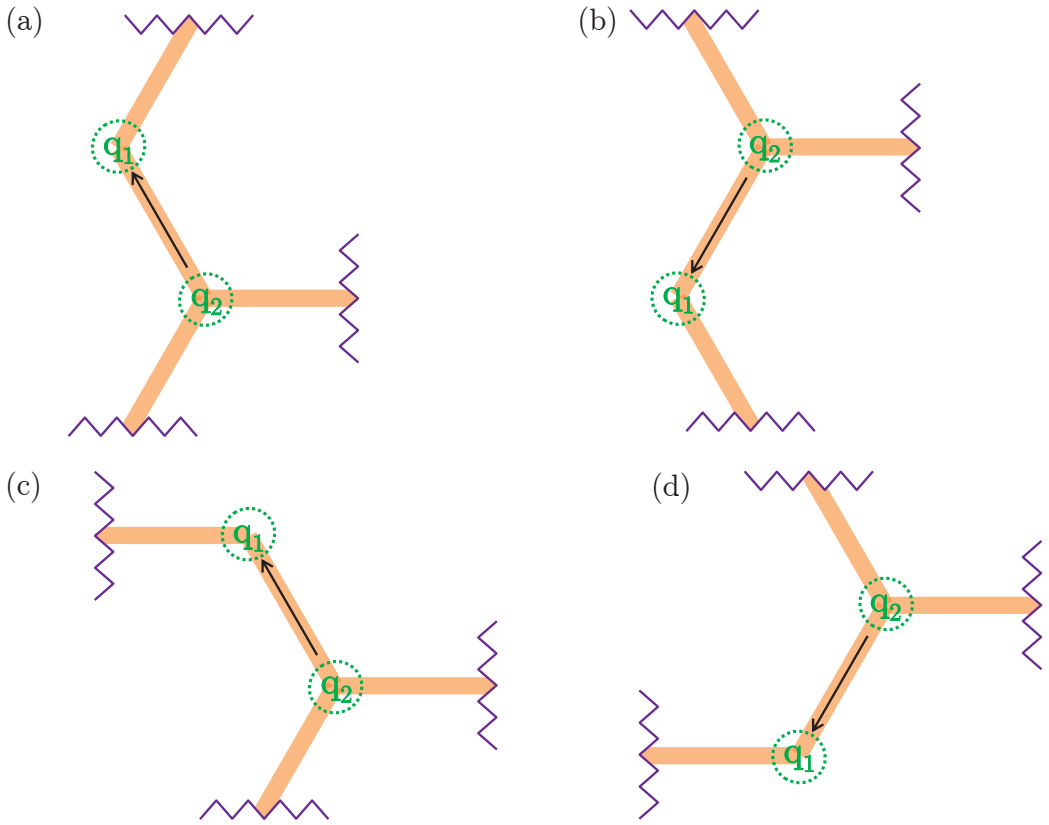

Figure 2.15: Schematic showing edge nanobars which have only three adjacent nanobars, one on their left hand side and two on their right. Their behaviour is described in Table 2.4.

q_1/q	q_2/q	vertex (v) types & (N)	DW type emitted
+2	+1	v1 neutral	head-to-head
+2	−1	v1 neutral	head-to-head
+2	−3	v2 repulsive	tail-to-tail
0	+1	attractive (2)	head-to-head
0	−1	attractive (1)	tail-to-tail
0	−3	v2 repulsive	tail-to-tail

Table 2.4: The possible q_1 and q_2 permutations for edge nanobars which have only three adjacent nanobars, two on their right hand side and one on their left such as those shown in Fig. 2.15. The vertex and emitted domain wall types and, where necessary, the values of $N = |q_{site}|/q$ are shown for all six different permutations.

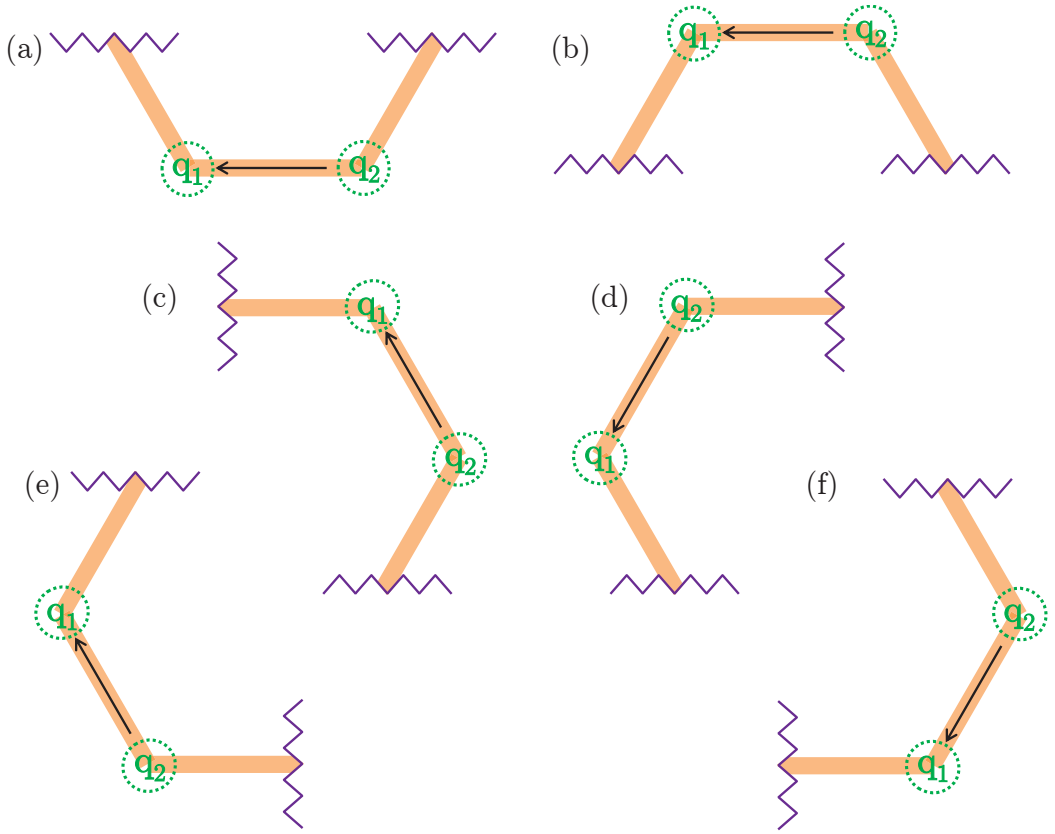

Figure 2.16: Schematic showing edge nanobars which have only two adjacent nanobars, one on their right hand side and one on their left. Their behaviour is described in Table 2.5.

q_1/q	q_2/q	vertex (v) types & (N)	DW type emitted
+2	0	v1 neutral	head-to-head
+2	−2	v1 and v2 neutral	either
0	0	attractive (2)	either
0	−2	v2 neutral	tail-to-tail

Table 2.5: The possible q_1 and q_2 permutations for edge nanobars which have only two adjacent nanobars, one on their right hand side and one on their left such as those shown in Fig. 2.16. The vertex and emitted domain wall types and, where necessary, the values of $N = |q_{site}|/q$ are shown for all four different permutations.

2.11 Summary

This chapter has provided a broad overview of magnetism and a detailed discussion of ferromagnetism. Concepts such as domain walls, chirality and magnetic reversal have been introduced in some detail due to their significance in this thesis. In addition, ASI, the primary frustrated system studied in this thesis, has been introduced, and its relationships with Water Ice and Natural Spin Ice have been documented. In addition, a simple charge model which describes the coercivities of the nanobars in ASI according to vertex charge, quenched disorder and orientation with respect to external field has been introduced.

In order to witness the interesting behaviour of ferromagnets discussed in this chapter, it is necessary to measure or image their magnetisation experimentally. The next chapter details various different investigative techniques used to probe a nanostructure's magnetic response. In addition, micromagnetic simulation, a tool used to gain further insight into a nanostructure's behaviour, is introduced. Furthermore, details of the fabrication method used to make these nanostructures are presented.

CHAPTER 3 : INVESTIGATIVE TECHNIQUES

In order to study magnetic systems like Artificial Spin Ice, magnetic elements which are small enough to support individual domains must be fabricated. An electron beam lithography and thermal evaporation technique is well suited to making submicron structures and offers easy control over the dimensions grown. As such, this technique was used to make the samples described in this thesis. Details of each of the fabrication steps and the optimisation thereof are documented in this chapter.

Once a sample has been grown optimally, its magnetic behaviour must be probed. There are many different complementary techniques for measuring magnetisation. The magnetic moment of a whole thin film or patterned thin film can be measured as a function of temperature and externally applied magnetic field. This is called *bulk magnetometry* and is instrumental in characterising a sample's overall behaviour. Additionally *imaging* techniques, which yield information about the magnetisations of individual fabricated structures, can be used to gain a more complete understanding of an array's behaviour. In this chapter, each of the experimental techniques used to study magnetisation are discussed, and in addition, their relative merits are evaluated.

The ability to predict a magnetic system's behaviour is important during both the planning of an experiment and the analysis of results. *Micromagnetics*, the study of interactions between magnetic moments over submicron distances, has been studied since 1963 [45], and *micromagnetic simulations* may be used to make these important predictions. In this chapter, the theory behind micromagnetic simulations is explained and two micromagnetic solvers, *OOMMF* and *MuMax*, are introduced.

3.1 Nanofabrication

The samples discussed in this thesis were designed and made at Imperial College. Although I was involved in the fabrication process for some pilot projects, the LTEM sample described in Chapter 4 was made by Katharina Zeissler, the Artificial Spin Ice samples discussed in Chapters 5 & 6 were made by Katharina Zeissler, Dan Read and Sam Ladak, and the Artificial Dipolar 2D-XY nanodisc samples discussed in Chapter 7 were made by Katharina Zeissler (the LTEM sample) and Megha Chadha (the rest). The design of these samples, however, was achieved collectively.

A number of processing steps are required in order to fabricate samples via an electron beam lithography and thermal evaporation technique. Firstly the nanopattern must be designed. Then, once a suitable substrate has been selected, an electron sensitive resist must be spun onto the substrate. Electron beam lithography is then performed. After lithography the sample must be developed and plasma ashed in preparation for thermal evaporation. Once the desired deposition thickness has been achieved, the sample must be soaked in acetone to achieve lift off. These steps are illustrated schematically in Fig. 3.1 and a detailed discussion of each process follows.

3.1.1 Design

Nanostructures were designed using the Graphic Database System II (GDSII) software. The GDSII design is subdivided into *write-fields*. The entire write-field area ($100\,\mu m \times 100\,\mu m$ in this thesis) can be reached by small deflections of the electron beam. If larger structures are required, however, the stage moves the sample which can be imprecise. In order to avoid this, structures were placed such that they did not cross write-field boundaries.

Alignment markers (large crosses or discs) were included at the corners of the design and identification labels were included at the edges. These markers and labels were necessary for quick navigation during imaging.

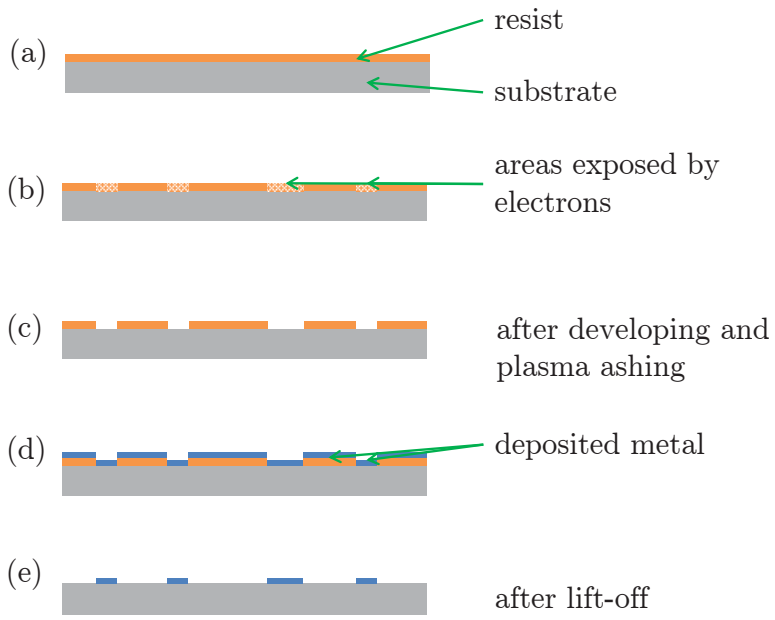

Figure 3.1: Schematic to show how a positive resist is used during nanofabrication. (a) shows the sample after the resist has been spun uniformly and baked, (b) shows the sample after electron beam lithography, (c) shows the sample post developing and ashing, (d) shows the sample post thermal evaporation and (e) shows the finished sample after lift-off.

3.1.2 Choice of substrate

Nanostructures are typically fabricated onto a *substrate*. The choice of substrate depends on the type of experiment the sample is required for. For transmission experiments a transparent membrane must be used. Agar Scientific Product Number S171-2 silicon nitride membranes were used for Lorentz Transmission Electron Microscopy. These are extremely delicate, flat and smooth membranes which are 50 nm thick and 0.5 mm × 0.5 mm in area. The membrane is stretched over a silicon support designed to fit a standard 3 mm × 3 mm Transmission Electron Microscopy holder. Scanning Transmission X-ray Microscopy (STXM) holders are larger allowing for a 5 mm × 5 mm sample support. As such, slightly more robust silicon nitride membranes from Silson Ltd. were used for STXM, 100 nm thick and 1 mm × 1 mm in area.

For experiments not requiring transmission, a more robust substrate may be used.

A silicon substrate was used for Photo Emission Electron Microscopy experiments and a silicon/silicon dioxide substrate was used for Magnetic Force Microscopy and Superconducting Quantum Interference Device measurements.

3.1.3 The spinning process

For electron beam lithography, a uniform layer of electron-sensitive *resist* must be coated on the substrate. A polymer resist, poly(methyl methacrylate) (PMMA 950 A4), dissolved in Anisole was used. PMMA can act as both a *positive* and a *negative* resist depending on the *dose* or number of electrons per cm^2. At low dose, the polymer chain length is reduced by the electrons in a process known as *scission* making it more soluble in an appropriate solvent, but at higher doses, polymerisation occurs which causes crosslinking making it very insoluble [46, 47]. A positive resist is used for a thermal evaporation and lift-off process. A negative resist is used for a top-down approach in which surplus metal is milled away from a pre-prepared thin film. The former method was used in this thesis because it yielded better definition of nanostructures' edges.

The substrate was attached to a spin coater on a spin-able chuck. The type of chuck used depended on the substrate chosen; silicon substrates were held by vacuum on to the chuck whereas membranes were secured by screws on a special bespoke chuck to avoid damaging the membrane. Resist was pipetted onto the substrate until it was covered. Care was taken to avoid air bubbles on the surface of the resist as these led to anisotropic spinning. The optimum spinning parameters varied for different substrates and different resist batches and those used in this thesis are detailed in Table 3.1.

The sample was then placed on a hot plate (see Table 3.1 for bake temperature and duration). This heating process removed the solvent from the resist.

3.1.4 Electron beam lithography

In electron beam lithography high energy electrons are focussed on to the sample under high vacuum and trace out the GDSII design. The electrons expose the resist,

	ASI & LTEM samples	**Nanodisc samples except LTEM**
spinning time (minutes)	2	1
spinning rate (rpm)	1800	5000
baking time (minutes)	5	1.5
baking temperature (°C)	155	90

Table 3.1: The spinning and baking parameters used during fabrication of samples studied in this thesis.

the degree of which depends on the dose selected. A *dose test*, in which the electron beam dwell time was varied, was performed during preliminary experiments for each resist/substrate combination in order to determine optimum exposure parameters. A greater dose corresponds to a longer beam dwell time and hence an increased resist exposure.

Electron beam lithography was performed with a RAITH e_LINE Ultra High Resolution Electron Beam Lithography and Metrology Tool. The system's maximum accelerating voltage of 20 kV was used in order to optimise resolution. At 20 kV the beam size at the focal point is 2 nm allowing the system to achieve minimum feature sizes of order 20 nm.

3.1.5 Developing and plasma ashing

After electron beam lithography, it is important that the exposed areas of resist are removed to create well-defined gaps. In order to achieve this, the sample is developed and plasma ashed.

In the work in this thesis, the sample was soaked in a developing solution of 1 : 3 methyl isobutyl ketone (MIBK) : isopropanol (IPA), a ratio chosen to optimise contrast. Then the sample was placed in a beaker of IPA. In addition, in order to remove any further residual resist from the exposed areas, the sample was then placed in an Emitech K1050X Plasma Asher. Here oxygen was bled in to the chamber and radio frequency waves ionised the O_2 to create monatomic oxygen plasma. This plasma readily reacted with the exposed resist to form an ash which was then removed

by a vacuum pump. The optimal parameters used for developing and plasma ashing varied for different samples and those used in this thesis are shown in Table 3.2.

	ASI & LTEM samples	**Nanodisc samples except LTEM**
developing time (s)	60	90
IPA time (s)	30	30
radio frequency power (W)	10	10
ashing time (minutes)	2	2
pressure (mbar)	6×10^{-1}	2×10^{-1}

Table 3.2: The developing and ashing parameters used during fabrication of samples studied in this thesis.

3.1.6 Thermal evaporation

After developing and ashing, the sample is ready for thermal evaporation. In this process a magnetic material is heated and its vapour is deposited on the sample above.

In this work, the sample was attached with Kapton tape (chosen since it does not outgas under vacuum) to a metal plate inside the E306 metal box coater evaporator. A crucible with the material required for deposition in was placed below the sample. A large boat to sample distance was necessary for uniform deposition. The crucible to sample distance was 30 cm, which was the maximum possible distance given the chamber geometry. In addition the sample was placed directly above the source in order to prevent shadowing effects. The quality of evaporated films depends on the level of contaminants such as oxygen during deposition. This was minimised through the use of vacuum systems which obtained a base pressure of 3×10^{-7} mbar. The permalloy was Joule heated and the thickness and rate of deposition on the sample were monitored with an in-situ quartz crystal monitor. This monitor was calibrated by measuring thicknesses of metal deposition on calibration samples using Atomic Force Microscopy (AFM) (see Section 3.2.7). Once a uniform deposition rate was established a shutter between the crucible and the sample was opened starting

deposition on the sample. Once the desired thickness of deposition was achieved, the shutter was used to block the passage of metal and the current was lowered, allowing the system to cool. The final film thickness was verified later through AFM.

3.1.7 Lift-off

In order to remove the remaining unexposed resist and the metal deposited on that resist, the sample was soaked in acetone for approximately 2 days. If the substrate was robust i.e. silicon or silicon/ silicon dioxide, the lift-off process was assisted with 30 seconds of ultrasonic agitation.

After soaking in acetone, any remaining residue was washed off with IPA. The sample was then blow dried with nitrogen gas.

3.1.8 Sample profiling

In order to optimise the nanofabrication process, the samples' profiles were analysed. *Scanning Electron Microscopy* yielded information about the structures' lateral dimensions in the plane of the substrate and *Atomic Force Microscopy* (discussed in detail in Section 3.2.7) provided additional information about the structures' thicknesses and roughnesses.

3.2 Experimental magnetic techniques

Various different complementary experimental techniques enable the behaviour of nanomagnetic systems to be studied. A *Vibrating Sample Magnetometer* or *Superconducting Quantum Interference Device* measures a sample's magnetic moment as a function of temperature and externally applied magnetic field. This provides information about a sample's saturation magnetisation, coercivity and Curie Temperature. Magnetocrystalline and shape anisotropies of a structure can be studied via *Magneto Optic Kerr Effect* lensing. Here, coercivities in different directions can be inferred from hysteresis loops. Magnetic imaging techniques, however, can provide information about the magnetisation directions of individual elements within an ar-

ray. Both *Scanning Transmission X-ray Microscopy* and *Photo Emission Electron Microscopy* are imaging techniques which yield different contrast for magnetisations in opposing contrast directions. This can enable the unique determination of individual structures' magnetisation directions. In addition, *Lorentz Transmission Electron Microscopy* produces electron phase contrast images which, with the help of computer simulation e.g. with MALTS (see Chapter 4), enables the magnetic structure of very small individual elements to be inferred. Furthermore, *Magnetic Force Microscopy* yields images of the magnetic charges associated with individual structures' magnetisations which may provide enough information to infer magnetisation states. In the following sections, these different techniques are discussed and their relative merits are evaluated.

3.2.1 Vibrating Sample Magnetometry (VSM)

In Vibrating Sample Magnetometry (VSM) a magnetic sample is oscillated sinusoidally within a static coil set in a uniform field (see Fig. 3.2) [11,13]. The changing magnetic field, $\mathbf{B}$, due to the moving magnetic sample induces an electric field, $\mathbf{E}$, in the coil set (described by Maxwell's Equation $\nabla \times \mathbf{E} = \partial\mathbf{B}/\partial t$). This induced electric signal in the coil set is amplified and detected by a lock-in amplifier. The signal measured is proportional to the magnetic moment of the sample. By varying the magnitude of the uniform field and measuring the sample's magnetic response, a hysteresis loop (see Section 2.8) for the whole sample may be generated. In addition, the sample space may be cooled allowing for magnetisation vs. temperature measurements at constant external fields.

A Quantum Design Physical Property Measurement System was used for Vibrating Sample Magnetometry. The system has external magnetic fields capabilities of up to 9 T, temperature capabilities of 2 K to 380 K and is able to resolve magnetisation changes of order 10^{-6} emu (1×10^{-9} Am^2) [48].

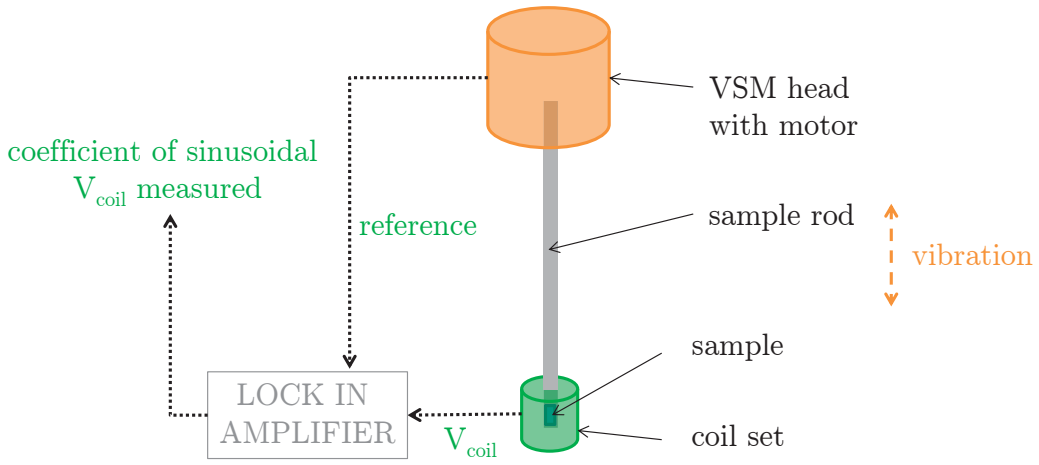

Figure 3.2: Schematic of Vibrating Sample Magnetometry. The magnetic sample is driven sinusoidally within a coil set. The induced voltage is amplified and its sinusoidal coefficient, which is proportional to its magnetisation, is measured.

3.2.2 Superconducting Quantum Interference Device (SQUID)

A Superconducting Quantum Interference Device (SQUID), comprised of two superconducting loops with Josephson junctions, can be used for high sensitivity bulk magnetometry. SQUIDs can detect changes in magnetisation of the order 10^{-8} emu (1×10^{-11} Am^2).

The SQUID measurements in this thesis were performed by Megha Chadha at the London Centre for Nanotechnology.

3.2.3 Magneto Optic Kerr Effect lensing (MOKE)

If polarised light is reflected off a magnetic material, the plane of polarisation of the light is slightly rotated. This is called the *Kerr effect* and is exploited in Magneto Optic Kerr Effect (MOKE) lensing in which measurements of the light's polarisation versus applied fields enables hysteresis loops (see Section 2.8) to be mapped out. A NanoMOKE^{TM}2 from Durham Magneto Optics Ltd. was used for sample characterisation [49]. The experimental setup is shown in Fig. 3.3 and was as follows. 1.348 mW of 635 nm light from a laser was collimated and linearly polarised by optical compo-

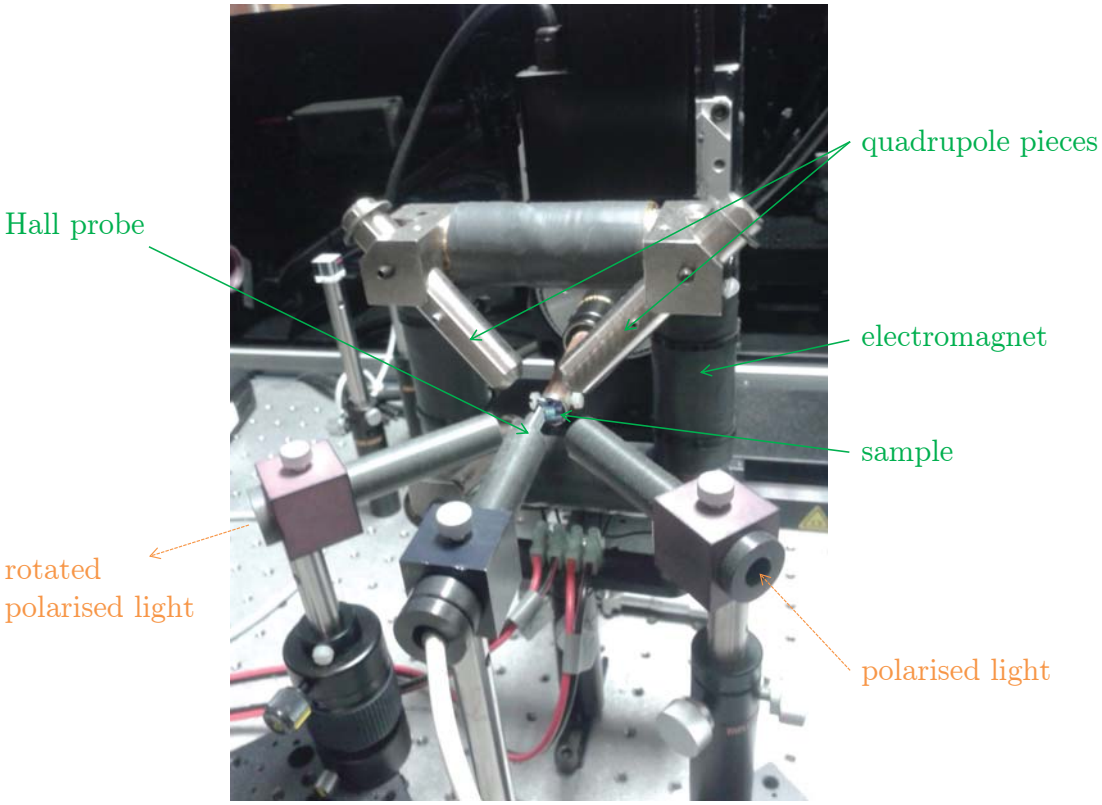

Figure 3.3: Photograph of the Magneto Optic Kerr Effect lensing setup. Incoming polarised light is reflected off a magnetic sample and its plane of polarisation is rotated. An electromagnet and quadrupole pieces provide in-plane magnetic fields, the magnitude of which are measured by a Hall probe.

nents. This light was then focussed onto the sample to a spot with a 5 µm footprint and underwent Kerr rotation and Kerr ellipticity, the degrees of which depended on the local magnetisation. This reflected light was analysed and then measured by a photodetector. A quadrupole magnet was situated around the sample and as such, magnetic fields in the plane of the sample were applied. These fields were applied with a user defined frequency and magnitude and measured by a Hall probe. As the field changed, the Longitudinal Kerr signal arriving at the detector was recorded and in this way a hysteresis loop was swept out. The average of hundreds of these loops was typically computed in order to counter the effects of noise on the data.

3.2.4 Scanning Transmission X-ray Microscopy (STXM)

Scanning Transmission X-ray Microscopy [50, 51] is a magnetic imaging technique which gives element specific in-plane magnetisation contrast by exploiting *Magnetic Circular Dichroism* (MCD); depending on the local magnetisation direction in the specimen, left or right handed circularly polarised light is absorbed more than the other. The direction of the magnetisation can be inferred by looking at the difference in the transmission of the left and right handed circularly polarised X-rays (see Fig. 3.4 schematic).

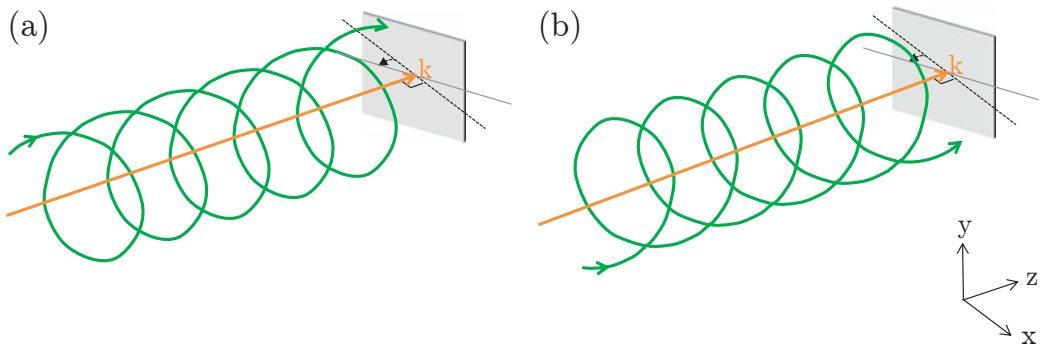

Figure 3.4: Schematic showing how MCD is exploited in STXM and PEEM magnetic imaging. (a) & (b) depict the incidence of right and left handed circularly polarised light (defined with respect to the source) on the sample respectively. The wave vector, k, shows the axis of light propagation and the green spiral depicts the rotation of the electric field. In order to probe the in-plane magnetic contrast, the sample must be tilted into the incoming beam direction. This tilt is labelled with the black dotted line. For permalloy, if the incident light is tuned to the nickel L_3 edge at 850 eV, differences in the absorption in situations (a) & (b), detected either by transmission (STXM) or secondary electron collection (PEEM), yield magnetic contrast.

In STXM, left or right handed circularly polarised light is focussed onto the specimen. For permalloy, these circularly polarised photons are designed to resonate with the nickel L_3 edge which is at 850 eV. This edge is chosen since it yields the highest differential absorption (there are 79 nickel atoms to every 21 iron atoms in permalloy ($Ni_{79}Fe_{21}$)). As the X-rays raster across the sample some of them are absorbed and some are transmitted through the sample. The transmitted intensity is measured via

a photomultiplier tube or photodiode for comparison with the equivalent measurement with the opposite handedness of circularly polarised light. Since the specimen must be partially transparent to X-rays, the structures of interest must be thin and prepared on a silicon nitride membrane (see Section 3.1.2).

STXM was performed at both the Molecular Environmental Science Beamline 11.0.2 at the Advanced Light Source, Lawrence Berkeley National Laboratory, Berkeley, California (see Chapters 5 & 6) and at the PolLux- X07DA Beamline at the Swiss Light Source, Paul Scherrer Institute, Villigen, Switzerland (see Chapter 7). Scanning TXMs were used in preference to full-field TXMs due to an ongoing collaboration with STXM Beamline Scientist Tolek Tyliszczak at the Advanced Light Source.

3.2.5 Photo Emission Electron Microscopy (PEEM)

Photo Emission Electron Microscopy [52,53] is an imaging technique which also makes use of Magnetic Circular Dichroism (see Fig. 3.4). In PEEM, circularly polarised synchrotron X-rays are incident on the sample and some of these X-rays excite 2p electrons to the conduction band leaving holes in the valence band behind. Secondary electrons excited to the conduction band near the sample surface are subsequently collected. In order to minimise the attenuation of these secondary electrons between the sample and the detector, PEEM is performed in ultra-high vacuum ($\approx 1\times10^{-9}$ mbar). The intensity of these secondary electrons is proportional to the X-ray absorption cross-section which again depends on the handedness of the incoming X-rays. By taking a difference measurement between the intensity profiles of secondary electrons emitted for left and right handed circularly polarised light, MCD contrast may be seen.

PEEM was performed at Beamline I06 at the Diamond Light Source, Harwell Science and Innovation Campus, Oxfordshire (see Chapter 6). PEEM samples were designed to be high vacuum compatible. In addition, sample surfaces were coated with a conductive layer in order to prevent *arcing* due to charge build up.

3.2.6 Lorentz Transmission Electron Microscopy (LTEM)

Transmission Electron Microscopy (TEM) is a tool used in order to achieve higher resolution images (potentially sub Angstrom in an aberration corrected system) than a normal optical microscope can offer ($\approx 300\,\text{nm}$) [54]. In addition a TEM can be used to achieve a diffraction pattern similar to an X-ray diffraction pattern but for much smaller areas of interest. Unlike the optical microscope which uses light, the TEM uses high energy electrons ($\approx 300\,\text{kV}$ accelerating voltage) which have much smaller associated wavelengths (at $300\,\text{kV}$, $\lambda = 1.97\,\text{pm}$). In addition, instead of using optical lenses to focus the beam, electromagnetic lenses are used, the strength of which can be adjusted.

A TEM consists of an electron gun which generates the high energy electrons, electron lenses which collimate the electrons such that they are parallel when incident on the sample, an objective lens to focus the electron beam from the sample and two further lenses to magnify the image of the sample. The electrons can be collected on a screen coated with a phosphorescent material such as zinc sulphide (ZnS) which emits light in the visible range forming a direct viewing screen. The room must be dark in order to see the phosphorescence from the screen. Alternatively an electronic image can be obtained with a Charge-Coupled Device (CCD) detector. Because of the great depth of focus of the electron microscope, the screen and the CCD detector can sit at physically different positions in the microscope column but still both yield in-focus images.

The magnetic structure of a sample can be probed in a TEM through Lorentz Transmission Electron Microscopy (LTEM). As the electrons move through the sample in imaging TEM mode they pick up a quantum mechanical phase due to local electric and magnetic fields. This phase can be probed via two different modes, *Fresnel* mode and *Foucault* mode. Fresnel mode yields contrast of domain walls and Foucault mode yields contrast of domains [55]. The discussion of LTEM from now onwards refers to Fresnel mode due to its availability at Imperial College London. Since isolated phases cannot be measured, in Fresnel mode the interference between electrons of different phases is measured. Classically one can consider the electrons

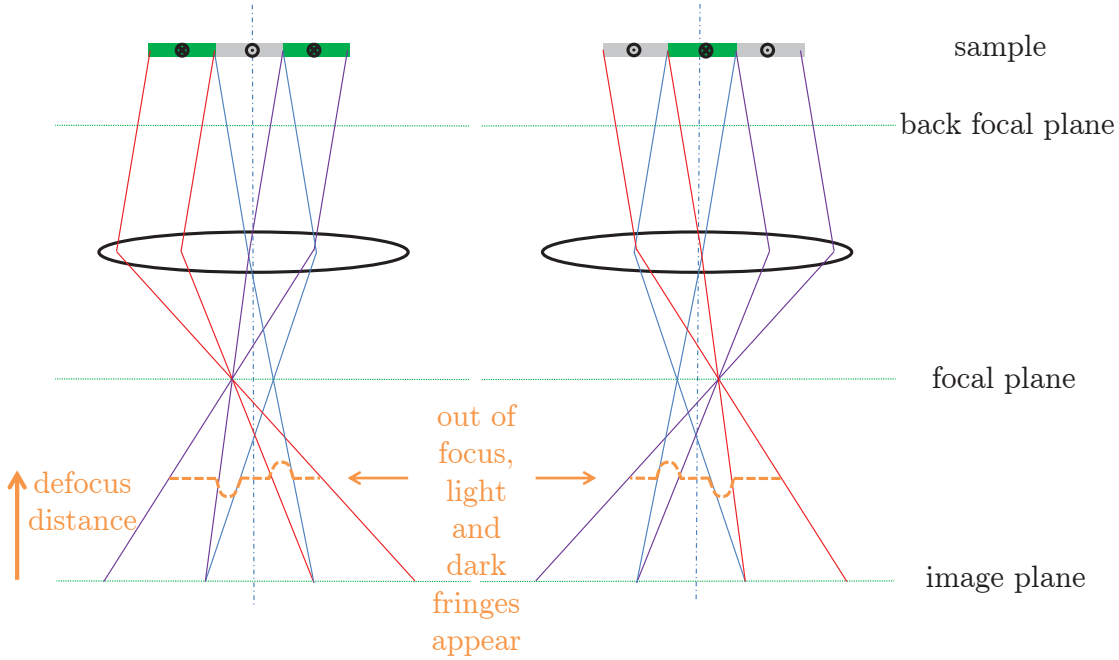

Figure 3.5: A classical ray-optics depiction of how LTEM electron phase contrast gives information about magnetisation directions. Green and grey colours in the sample depict domains pointing into and out of the page respectively. The angle of deflection and distance of defocus in this schematic have been exaggerated. In reality a defocus of $\approx 1600\,\mu m$ is sufficient to see dark and light fringes of good contrast.

being deflected by a Lorentz force due to electric and magnetic fields; regions with opposite magnetisation separated by a domain wall deflect electrons in opposite directions giving rise to regions of constructive and destructive interference, the locations of which depend on the orientation of the domain wall. This contrast is only present out-of-focus as demonstrated in Fig. 3.5. Optimal images are taken at defocuses large enough to achieve discernible magnetic contrast but small enough to avoid significant image distortion.

A FEI TITAN 80/300 in the Materials Department at Imperial College was used to perform Fresnel mode LTEM. When moving from TEM to LTEM mode, the objective lens was switched off due to its close proximity to the sample. The objective lens is the strongest lens and as such has a large magnetic field which can saturate the sample. Instead of using the objective lens for collecting the electrons from the sample, the

aberration corrector was used which gives lower resolution of the image but does not affect the sample's magnetisation. The Fresnel mode LTEM image at the screen was taken at a defocus of $\approx 1600\,\mu m$ in order to see the interference caused by magnetic structure. If in-situ magnetic fields were required for in-field measurements the objective lens was excited weakly. This excitation produced a magnetic field parallel to the electron beam direction and perpendicular to the sample. As such the sample had to be tilted in order to achieve a component of the external magnetic field in-plane.

3.2.7 Atomic and Magnetic Force Microscopy (AFM and MFM)

Atomic Force Microscopy is a tool used to probe the height and roughness of nanostructures. It works on the following principles. A piezo stack excites a cantilever vertically causing the cantilever to oscillate. A laser beam reflects off the back side of the cantilever into a photodetector [56, 57]. A small tip attached to the cantilever has a long axis perpendicular to the sample surface. When the cantilever approaches the sample, the amplitude of oscillation of the cantilever decreases due to the Van der Waals' forces and capillary forces (due to thin layers of water present in ambient conditions) which the tip experiences. This change in oscillation amplitude is then detected as a change in the reflected laser signal. The system then responds via a proportional integral feedback loop and retreats from the sample surface until the amplitude is constant again. The user selects this *amplitude setpoint* which corresponds to the constant amplitude of oscillation of the cantilever. A small amplitude setpoint means that the tip is close to the sample and experiences large repulsion from the sample surface. This corresponds to the quickest response times of the feedback system and as such small amplitude setpoints are favoured for high resolution images. Since the amplitude of the cantilever oscillation is constant, a constant separation between the cantilever and the sample is maintained. Thus the height profile of the cantilever matches the height profile of the actual sample (see Fig. 3.6). The exact landscape can be monitored by measuring the piezo height needed to maintain a constant amplitude for the cantilever oscillation.

Veeco RTESP14 phosphorus (n) doped silicon tips were used for AFM in this thesis.

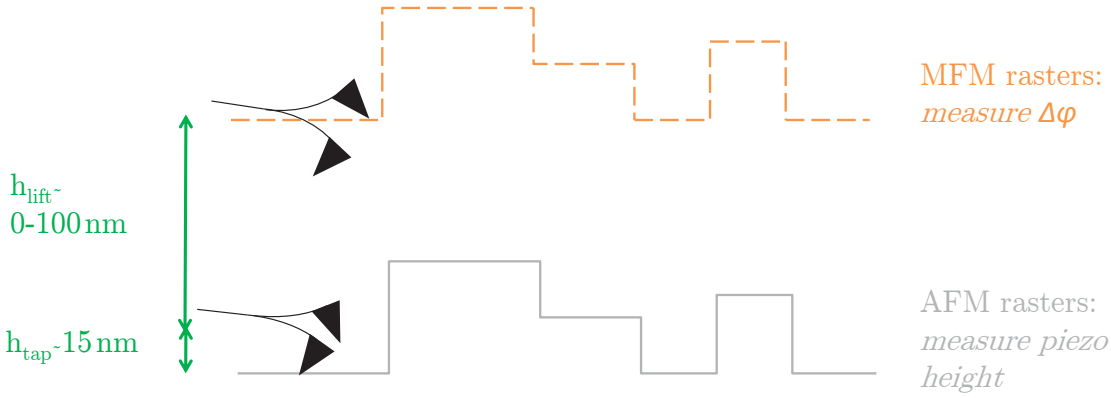

Figure 3.6: Atomic and Magnetic Force Microscopy schematic. The solid grey line shows tapping mode Atomic Force Microscopy. Here the cantilever oscillates with a constant amplitude enabling the height profile of the sample to be mapped. The dashed orange line represents the subsequent rastering of a magnetic tip at a constant larger tip to sample separation. This extra step is necessary in Magnetic Force Microscopy in order to map out the sample's magnetic charge landscape.

Magnetic Force Microscopy works in conjunction with Atomic Force Microscopy and requires a magnetic coated tip [56, 57]. This tip is magnetised along its long axis such that its magnetisation is perpendicular to the sample; the tip is sensitive to the sample's out-of-plane magnetic fields. It is important that the coercivity of the tip is high enough not to be switched by the sample's magnetic field. After the cantilever rasters over the sample in tapping AFM mode to create a topological profile, an extra raster scan occurs at a much higher tip to sample separation (e.g. 60 nm above the AFM rastering, see Fig. 3.6). At this height the tip tracks exactly the same topological profile as recorded in the AFM so that the Van der Waals' forces seen by the tip are constant. In the absence of magnetic forces, the cantilever has a resonant frequency, f_0, which depends on the lift height selected. This is shifted in the presence of magnetic fields by Δf which is proportional to the vertical magnetic gradients. The shifts in resonance frequency are small relative to the resonant frequency itself and can be measured via *phase detection* since a resonant shift, Δf, gives rise to a phase

shift, $\Delta\phi$. Here the lag between the drive voltage and the cantilever response is measured. In this way a sample's magnetic charge landscape is mapped out.

The tips used for MFM were Bruker MESP antimony (n) doped silicon with a cobalt/chromium coating which were magnetised in a direction perpendicular to the plane of the sample. Bruker MESP tips have magnetic moments of 1×10^{-13} emu and coercivities of ≈ 400 Oe.

3.2.8 Summary of experimental techniques

A range of different magnetic techniques have been discussed in this section. The advantages and disadvantages of each technique are summarised in Table 3.3.

Technique	**Information Gained**	**Limitations**
VSM	Magnetic moment as a function of temperature and external magnetic field.	Very small nanostructures do not give a large enough signal (sensitivity 10^{-6} emu).
SQUID	Magnetic moment as a function of temperature and external magnetic field. High sensitivity (10^{-8} emu).	Not available at Imperial College London.
MOKE	Angular measurements of magnetisation of $\approx 20\,\mu m^2$ area as a function of external magnetic field.	Hard to locate small structures. Acquisition of hysteresis loops of wide arrays of small structures is hard.
STXM	Element specific magnetisation images in external magnetic fields.	Only available at synchrotrons abroad. Contrast is hard to achieve on small structures and may be ambiguous.
PEEM	Element specific magnetisation images in external magnetic fields.	Only available at synchrotrons. Sample breaks if too much charge builds up.
LTEM	Element specific electron phase contrast in external magnetic fields.	Cannot apply pure in-plane fields. Membranes are very delicate and break easily. Electron phase contrast can be hard to interpret.
MFM	Location and relative magnitude of magnetic charges.	Cannot unambiguously determine in-plane magnetisation directions. Cannot measure low coercivity structures.

Table 3.3: A comparison of the merits of the experimental techniques used to probe magnetisation.

3.3 Micromagnetics

In order to predict and better understand the magnetic state supported by a structure, *micromagnetic simulations* may be performed. Here the Landau Lifshitz Gilbert (LLG) equation is solved in discretised meshes via numerical integration yielding an approximate dynamic solution to the magnetisation.

In the following sections computational details of micromagnetic simulations are addressed. In addition, the limitations of micromagnetic simulations are explored. And finally, two micromagnetic softwares OOMMF and MuMax are introduced and their operation discussed.

3.3.1 The Landau Lifshitz Gilbert Equation and discretisation

The Landau Lifshitz Gilbert (LLG) equation describes the time-varying damped precession of a material's magnetisation, $\mathbf{M}$, in a magnetic field, $\mathbf{H}_{eff}$, at absolute zero temperature (see Fig. 3.7):

$$\frac{d\mathbf{M}}{dt} = -\gamma \mathbf{M} \times \mathbf{H}_{eff} + \frac{\alpha}{M_s} \mathbf{M} \times \frac{d\mathbf{M}}{dt}, \tag{3.1}$$

in which γ is the gyromagnetic ratio, α is the dimensionless material dependent damping parameter and M_S is the material's saturation magnetisation. The Landau Lifshitz Gilbert equation is a differential equation describing the time evolution of a continuous function, the magnetisation, $\mathbf{M}$. In order to find an approximate solution to this equation, a finite difference method is employed in which the structure of interest is discretised into cuboidal meshes (see Fig. 3.8 i)) [58]. Within each mesh the magnetisation is assumed to be homogeneous (see Fig. 3.8 ii)), an approximation which is valid so long as the mesh size is significantly smaller than the material's exchange length. The LLG equation is then solved in each individual mesh via a numerical integration method.

In this finite difference method, the effective magnetic field, $\mathbf{H}_{eff}$, in Eq. 3.1 includes contributions not only from the externally applied magnetic field, but also from the neighbouring meshes' magnetic fields. $\mathbf{H}_{eff}$ depends on the energy E, the

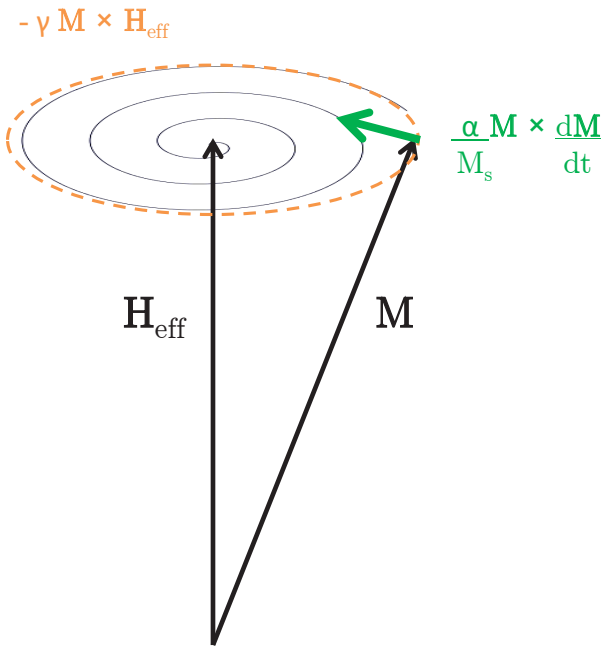

Figure 3.7: Schematic showing the motion of a magnetisation vector, $\mathbf{M}$, in a magnetic field, $\mathbf{H}_{eff}$, as described by the Landau Lifshitz Gilbert equation (Eq. 3.1). The circular precessional term is shown in orange and the damping term is shown in green. The path which the damped magnetisation follows over time is depicted in grey.

magnetisation, $\mathbf{M}$, and the permeability of free space, μ_0 [18, 58]:

$$\mathbf{H}_{eff} = -\frac{1}{\mu_0}\frac{\partial E}{\partial \mathbf{M}}, \tag{3.2}$$

in which E is a function of $\mathbf{M}$, which includes exchange, magnetostatic, magnetocrystalline anisotropy and Zeeman terms, as described in Section 2.4.

As described above, the LLG equation is solved in each individual mesh via a numerical integration method. Here the magnetisation in each mesh evolves for a given timestep after which the effective field, $\mathbf{H}_{eff}$, is recalculated for each individual mesh. The choice of timestep is important in the numerical integration; small timesteps allow for the most accurate computation and guard against missing interesting dynamics, whilst large time steps dramatically reduce simulation time. For a

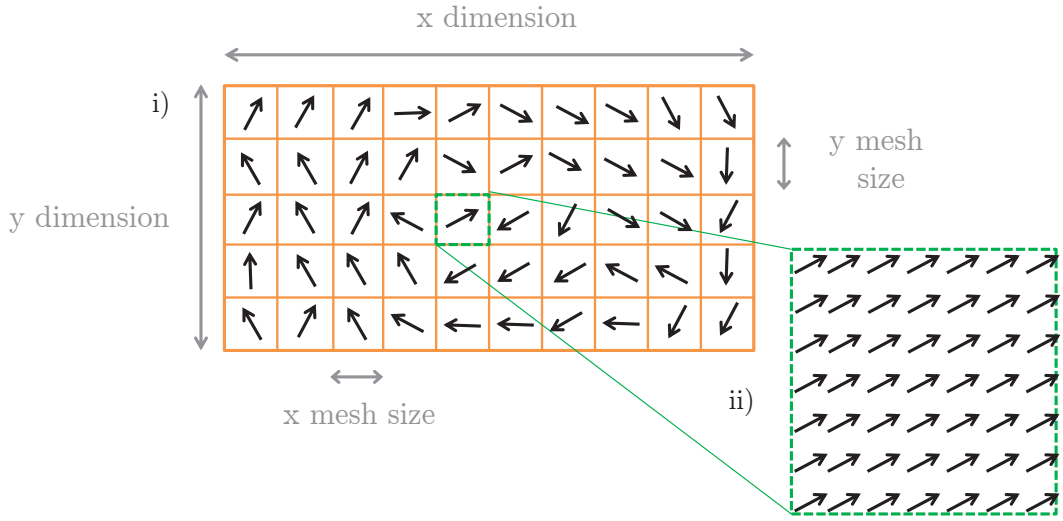

Figure 3.8: Discretisation into finite difference cuboidal meshes shown here via projection in the xy-plane i) user defined meshes within which the magnetisation direction is presumed homogeneous ii) atomic magnetic moments within each mesh, which are assumed to be aligned with respect to each other.

single stage of computation, e.g. evolution under a specific applied external magnetic field, the simulation evolves for a number of timesteps until one of three criteria has been met. If a torque criterion is used, the stage of the simulation ends when $|\mathrm{d}\mathbf{M}/\mathrm{dt}|$ decreases below a certain value in each mesh ($|\mathrm{d}\mathbf{M}/\mathrm{dt}| = 0$ only at $t = \infty$). Typically a torque criterion of between 0.01 and 1 degrees per nanosecond is used. If a time criterion is used, the simulation evolves for a fixed amount of time before moving on to the next stage. And if a stage iteration limit is imposed, only a certain amount of successful evolver steps are allowed per stage.

Another important consideration in micromagnetic simulation is temperature. The LLG equation is effective at absolute zero temperature. However, in experimental situations at finite temperature, thermal perturbations exist. These may be simulated by adding uncorrelated *white noise* via an extra magnetic field in the $\mathbf{H}_{eff}$ term of the LLG equation (Eq. 3.1) [59]. The extra fluctuating magnetic field takes the form of a Gaussian distribution centered on zero with variance directly proportional to temperature.

3.3.2 Limitations

Micromagnetic simulations give an excellent insight into micromagnetic behaviour for structure's of any geometry and size in any external magnetic field sequence. However due to some limitations of micromagnetic simulations, the simulated magnetic structure may not correspond to experimental observations. Some possible sources of error in micromagnetic simulations are described below.

Micromagnetic simulation assumes a perfectly homogeneous sample with smooth edges and surfaces. This is unlikely to be the case in practice and both roughness and defects can cause small changes in the magnitude of the coercive field. In addition, if simulations are performed at absolute zero, since the simulation of temperature effects rarely yields a converged state, the switching fields may be overestimated compared with those observed in room temperature experiments. Further inaccuracies may arise if the structure's edges do not coincide with the cuboidal mesh boundaries. In this situation, the edges of the structure take a step-like profile and the stray field computed differs significantly from the field produced from an ideal edge [60]. This effect can be minimised by reducing the mesh size, but this also lengthens the simulation time considerably.

3.3.3 The Object Oriented Micromagnetic Framework (OOMMF)

The Object Oriented Micromagnetic Framework (OOMMF) [18] is a freely and publicly available micromagnetic solver. The original software from OOMMF, however, does not consider thermal effects, but a temperature add on has been provided by a group at the University of Hamburg [59]. All OOMMF simulations described in this thesis were performed by the eXtensible solver (Oxs) in version 1.2.0.4 at $T = 0\,K$. The time evolver uses a first order forward Euler method with a timestep optimisation feedback system.

3.3.3.1 Simulation input

The software requires the input of a *.mif* file and a *.bmp* file. The *.mif* file contains information about the sample of interest and the external field sequence. The *.bmp* file gives information about the geometry of the structure and represents its projection in the xy-plane (typically black areas define magnetic regions, white areas define non-magnetic regions).

The material dimensions, magnetisation saturation, exchange constant and magnetocrystalline anisotropy, must be recorded in the *.mif* file. In addition, the dimensions of the sample and the size of the cuboidal meshes must be defined. When choosing the mesh size, the dimensions of the structure should be considered since there must be an integral number of meshes in every direction. If a smaller mesh size is chosen, the simulation is more accurate but suffers from a longer computation time. A lateral mesh size in the x and y directions of 5 nm for permalloy is typically used as a compromise between speed and accuracy. In addition, an α damping parameter must be selected. The α damping parameter is small for materials such as permalloy (0.008 [61, 62]) and as such the simulation time may be lengthy. If only the final state and not the dynamics, i.e. how the system gets to the final state, is of interest, however, α is increased to 0.5 in order to speed up the simulation. Finally the external field sequence and magnitude of the field steps must be defined. An external field of any magnitude may be applied in any direction, and is defined in terms of its projection on the x, y and z axes.

The structure's initial magnetisation direction may be defined in a second *.bmp* file via a (r, g, b) colourmap. Here the magnetisation direction described by spherical polar angles θ and ϕ must be transformed into Cartesian coordinates using a radius of 1. Then the following linear transformation must be applied in order to achieve the corresponding (r, g, b) values (see Fig. 3.9 for examples):

$$\begin{pmatrix} r \\ g \\ b \end{pmatrix} = \left(\begin{pmatrix} x \\ y \\ z \end{pmatrix} + 1 \right) \times \frac{255}{2}. \tag{3.3}$$

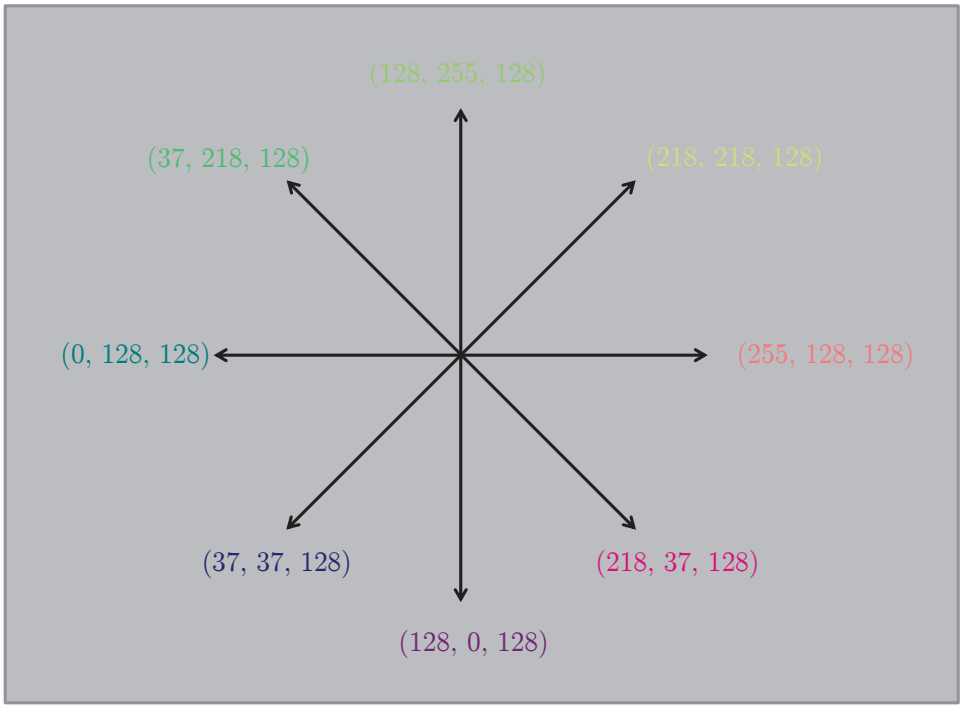

Figure 3.9: The colourmap used to intialise magnetisation in OOMMF simulations. Eight different initial magnetisation directions in the xy-plane are shown. Possible (r, g, b) values for each of these directions are shown in their corresponding (r, g, b) colour.

This colourmap method enables the user to start the simulation with a complex magnetic structure present like a domain wall with a user defined chirality.

3.3.3.2 Simulation output

The user may watch the OOMMF simulation evolving over time and *.txt* and *.omf* files may be outputted as the simulation proceeds. The *.txt* file contains information about the variation of the magnitude of the different energy terms as the simulation evolves. The *.omf* file displays the magnetisation vector of each mesh (in this thesis with contrast defined in Appendix B) and can also be used as a starting magnetisation configuration for a new simulation. The *.omf* file is useful for comparison with X-ray Magnetic Circular Dichroism images. In addition, the divergence of the magnetisation vectors in the *.omf* may be displayed enabling comparison with Magnetic Force

Microscopy images. However, electron phase contrast for comparison with Lorentz Transmission Electron Microscopy cannot be achieved readily from the *.omf* file. Instead a series of Fourier transform operations must be performed in a software such as MALTS (see Chapter 4).

3.3.4 MuMax

Another micromagnetic software, MuMax, was created by Arne Vansteenkiste and Ben Van de Wiele and released in 2011 [63]. MuMax is similar conceptually to OOMMF however it runs on graphical processing units (GPUs) rather than central processing units (CPUs) allowing the simulation to be sped up by a factor in excess of 100. Whereas CPU jobs can run on personal PCs, GPU jobs are run on the Imperial College High Performance Computing (HPC) system .

In MuMax, eight different Runge Kutta methods are available to solve the LLG equation. In addition, the software has inbuilt functionality for finite temperature simulation.

The input file, which is written in Python, contains information about the material, dimensions and magnetic field sequences and is similar to the *.mif* file used in OOMMF. A projection of the structure's geometry in the xy-plane is also required in *.png* form.

3.3.4.1 Relative merits of OOMMF and MuMax

As described above, OOMMF and MuMax are similar softwares for effective micromagnetic simulation. However, there are some minor operational differences between the two softwares. Firstly there is a restriction on the number of meshes allowed in the x, y and z directions in MuMax whereas there is no restriction in OOMMF. This restriction may be awkward if a certain mesh size is needed for comparison of structures of different dimensions. Another disadvantage of using MuMax is that colour maps (e.g. Fig. 3.9), the most intuitive way of defining initial magnetisation states especially chiralities (see Chapter 5 & 6) and available in the OOMMF software, cannot be used. Instead initial magnetisation must be defined in the input file.

Another drawback of MuMax is that, unlike with OOMMF, simulations cannot be visualised whilst running. These three disadvantages, combined with the fact that MuMax was only released part-way through this work, mean that the simulations shown in this thesis have been performed in OOMMF, despite its significantly longer processing time. There are numerous other micromagnetic solvers available but it was only feasible to evaluate two in this work.

3.4 Summary

In this chapter details of the nanofabrication method used to make the samples described in this thesis have been provided. In addition, seven different experimental magnetic techniques used to probe a sample's magnetic behaviour have been introduced. Furthermore, the possibility of simulating a structure's magnetisation state via micromagnetic simulations has been explored. Two micromagnetic solvers, OOMMF and MuMax have been introduced and their operation discussed.

Simulating electron phase contrast from the experimental magnetic technique Lorentz Transmission Electron Microscopy is not possible with micromagnetic softwares OOMMF or MuMax. As such, in the next chapter *MALTS* is introduced which, when used in conjunction with OOMMF or MuMax, provides a much needed platform for the simulation of this Lorentz TEM Fresnel electron phase contrast for structures of any geometry, shape and material.

CHAPTER 4 : MICROMAGNETIC ANALYSIS TO LORENTZ TEM SIMULATION (MALTS)

The OOMMF and MuMax micromagnetic softwares discussed in Section 3.3 can be used to simulate both X-ray Magnetic Circular Dichroism and Magnetic Force Microscopy contrast. However Lorentz Transmission Electron Microscopy Fresnel contrast (electron phase contrast) cannot be simulated directly. Although the electron phase contrast for common magnetic states such as single domain nanobars is well understood, the contrast for less common magnetic states such as single domain nanodiscs is neither well documented nor intuitive. Therefore *MALTS*, *Micromagnetic Analysis to Lorentz TEM Simulation*, was developed to provide a platform for the effective analysis of Fresnel electron phase contrast of magnetic structures of arbitrary shape and size. MALTS is used in conjunction with OOMMF and MuMax micromagnetic softwares and its full functionality is detailed below. This chapter's discussion and Figs. 4.1, 4.3, 4.4, 4.5, 4.6 & 4.7 are ©2013 IEEE and are adapted and reprinted, with permission, from S. K. Walton, K. Zeissler, W. R. Branford & S. Felton, MALTS: A Tool to Simulate Lorentz Transmission Electron Microscopy From Micromagnetic Simulations, IEEE Transactions on Magnetics, Aug. 2013 [64].

4.1 Demand for Lorentz TEM Simulation

The sensitivity of electrons to local magnetic fields enables Lorentz Transmission Electron Microscopy (LTEM) (see Section 3.2.6) to probe magnetic microstructure [4, 55, 65–78]. The LTEM contrast patterns which result from simple magnetic structures are well established, with the borders between domains showing up as bright or dark lines in the Fresnel or defocus mode [55, 65, 66]. As such LTEM has been

used effectively at Imperial College London to image single domain nanobars in Artificial Spin Ice. However for more complex magnetic structures such as single domain nanodiscs in Artificial Dipolar 2D-XY (see Chapter 7), the LTEM contrast is not so intuitive or easy to understand, rendering simulation important. Several different groups [4, 68–74, 78, 79] have published simulations of LTEM contrast obtained using code based on similar equations. However, this code is not generally available, making comparison between different simulations hard. For example Qi et al. [4, 68] use a simple MATLAB program which works on structures uniformly magnetised in the x direction, while McVitie and Cushley [69] have a more complex simulator capable of studying multiple domain structures. Therefore MALTS (Micromagnetic Analysis to Lorentz TEM Simulation) [64] was developed to serve as a transparent and easy-to-use software that computes Fresnel mode LTEM contrast images for thin magnetic nanostructures of all complexities.

The publicly available Object Oriented Micromagnetic Framework (OOMMF) [18] (see Section 3.3.3) and MuMax [63] (see Section 3.3.4) software enable the states supported by magnetic structures to be computed as a function of applied magnetic field. The result can be saved as an *.omf* file and displayed either showing the magnetisation direction of each mesh, allowing comparison with X-ray Magnetic Circular Dichroism images, or showing the divergence of the magnetisation, useful for comparison with Magnetic Force Microscopy images. However, a representation of a corresponding Lorentz TEM image is not available. Here it is shown how MALTS can convert the outputted *.omf* file from OOMMF or MuMax into a corresponding LTEM image. Similar software called GENIUS was presented by Haug et al. [79] in 2003, but it could not be obtained. MALTS is provided both as precompiled executables and as open source code, allowing users to expand and improve on its functionality.

4.2 Method

In Lorentz TEM, some of the incident high energy electrons are transmitted through the sample. These electrons experience a Lorentz force due to both local magnetic and electric field components. These interactions can be expressed in terms of a phase

via the Aharonov-Bohm expression [80]:

$$\phi = \phi_e + \phi_m = C_E \int V \, \mathrm{d}z - \frac{\pi}{\Phi_0} \int A_z \, \mathrm{d}z, \tag{4.1}$$

in which ϕ_e is the electric phase, ϕ_m is the magnetic phase, C_E is the accelerating voltage constant, Φ_0 is the magnetic flux quantum, V is the inner potential of the material and A_z is the z-component of the magnetic vector potential, where the axes are defined in Fig. 4.1.

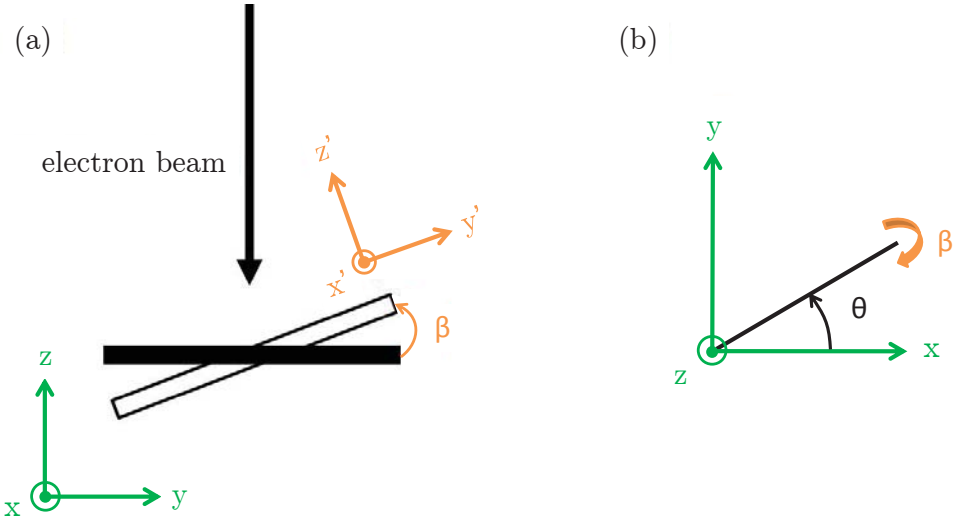

Figure 4.1: Schematic showing the coordinate systems used: x, y, z for the electron beam in green and x', y', z' for the sample in orange. The angles β and θ are also illustrated. β is the angle of tilt towards the incoming electron beam, as shown in (a) in which the solid rectangle represents the sample perpendicular to the beam and the unfilled rectangle shows the sample tilted by an angle β. θ defines the axis in the xy-plane about which this rotation is performed as shown in (b).

The electric phase term can be rewritten as $\phi_e = C_E V_0 t$, in which V_0 is the mean inner potential of the material and t is the thickness. The magnetic term, however, is more complex. Assuming that the x- and y-components of magnetisation vary only with the x- and y-coordinates, the magnetic phase component can be simplified in

reciprocal space [81] to

$$\widetilde{\phi}_m = \frac{i\pi\mu_0 M_S t}{\Phi_0}\left(\frac{\widetilde{m}_x k_y - \widetilde{m}_y k_x}{k_x^2 + k_y^2}\right), \tag{4.2}$$

in which μ_0 is the permeability of free space, M_S is the saturation magnetisation of the material, $\widetilde{m}_x$ and $\widetilde{m}_y$ are the magnetisation unit vectors in reciprocal space, and k_x and k_y are the x- and y-components of the reciprocal space k vector. This assumption holds over a single mesh in the z direction. MALTS deals with multiple meshes in the z direction via the linear addition of magnetic phases accrued through each individual mesh. For most TEM specimens, however, a single mesh in the z direction is a reasonable assumption since the film thickness is generally much smaller than the lateral dimensions. As such, all MALTS simulations shown in this chapter have a single mesh in the z direction.

The sample may be tilted in order to detect out-of-plane magnetisation. A sample tilt may also be used in experimental LTEM to apply an in-plane magnetic field. If the sample is tilted β degrees about the x-axis, the magnetisation unit vectors must be computed in a different coordinate system via $m_y = m'_y \cos\beta - m'_z \sin\beta$ and $m_x = m'_x$, see Fig. 4.1 (a). Proceeding in this manner, this can be generalised to a tilt of β degrees about an arbitrary axis in the xy-plane, θ degrees from the x-axis towards the y-axis, see Fig. 4.1 (b):

$$m_x = {m'}_x(\cos^2\theta + \sin^2\theta\cos\beta) + {m'}_y(\sin\theta\cos\theta)(1-\cos\beta) + {m'}_z\sin\beta\sin\theta, \tag{4.3}$$

$$m_y = {m'}_x(\sin\theta\cos\theta)(1-\cos\beta) + {m'}_y(\cos\beta\cos^2\theta + \sin^2\theta) - {m'}_z\sin\beta\cos\theta. \tag{4.4}$$

In addition, the sample has a new effective thickness due to the tilt, $t = t'/cos\beta$, and its new projection on the xy-plane is accounted for by resizing the sample via a bicubic interpolation method. Once the Fourier transform of the reciprocal magnetic phase shift has been calculated, the two phase terms can be added linearly, resulting

in a net phase.

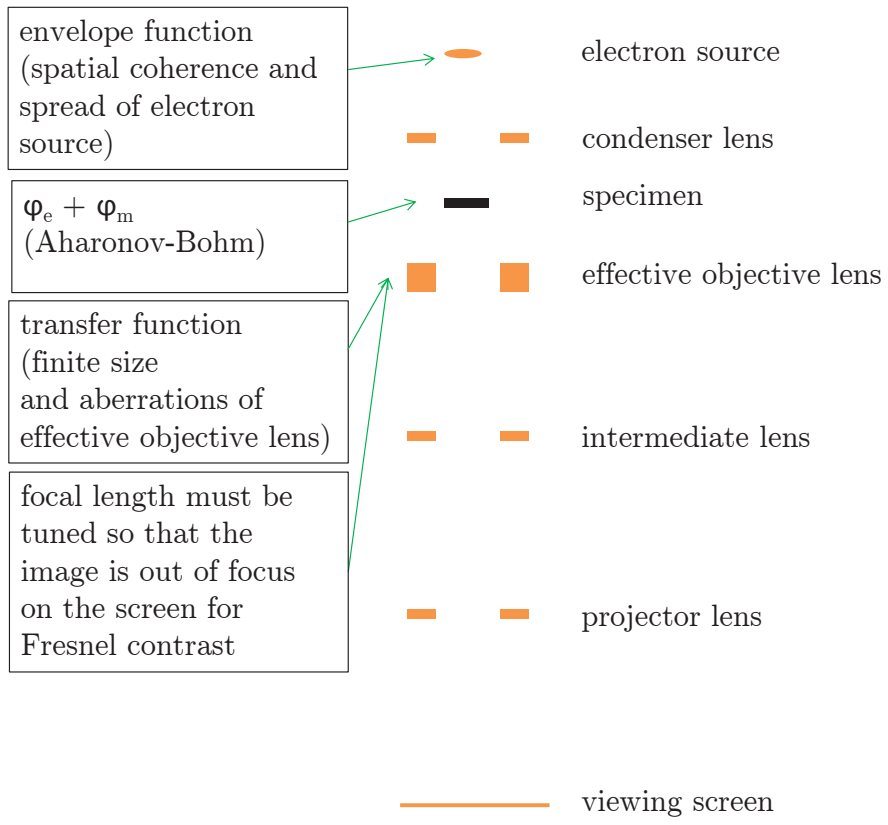

Figure 4.2: Schematic of the experimental setup of Lorentz Transmission Electron Microscopy. The electron beam passes through both the sample and a series of lenses before it is collected on a screen. The origins of the envelope function, Aharonov-Bohm phase and transfer function are described in the text.

When the electrons have passed through the structure acquiring both a magnetic and an electric phase, they reach the back focal plane of the objective lens (see Fig. 4.2). Here the electron disturbance can be computed by performing a Fourier transform on the wave function of the transmitted electron beam:

$$g(k_x, k_y) = \int\int f(x, y) \exp(-2\pi i(k_x x + k_y y))\, \mathrm{d}x\, \mathrm{d}y. \tag{4.5}$$

Since all electron lenses are finite in size and are subject to aberrations, the electron

wave is modified to $g(k_x, k_y)t(k_x, k_y)$ by the *transfer function* [55],

$$t(k_x, k_y) = A(k_x, k_y) \exp\left\{-2\pi i \left(\left[\frac{C_S\lambda^3({k_x}^2 + {k_y}^2)}{4}\right] - \left[\frac{\Delta z\lambda({k_x}^2 + {k_y}^2)}{2}\right]\right)\right\}, \tag{4.6}$$

in which $A(k_x, k_y)$ is the pupil function accounting for finite aperture size, λ is the relativistic wavelength of the electrons, C_S is the spherical aberration coefficient of the (effective) objective lens and Δz is the defocus. In MALTS the pupil function $A(k_x, k_y)$ is assumed to be constant for all reciprocal space. Since Fresnel mode LTEM involves using a large defocus, the term involving the spherical aberration is small compared to the defocus term and usually has a negligible effect. Therefore most of the simulations were performed at $C_S = 0$. However, since spherical aberration varies from instrument to instrument, the user is able to input their instrument's spherical aberration for simulations.

For a real microscope the fact that the resolution is limited by the spatial coherence and spread of the electron source also needs to be considered. MALTS uses an envelope function describing the spread of the source as a Gaussian distribution [54],

$$E_S(k) = \exp\left[-\left(\frac{\pi\alpha}{\lambda}\right)^2 (C_S\lambda^3 k^3 + \Delta z\lambda k)^2\right], \tag{4.7}$$

in which α is the beam divergence angle and $k = ({k_x}^2 + {k_y}^2)^{1/2}$. The envelope function acts to dampen the electron signal at high scattered angles. Finally an inverse Fourier transform is required to get the final intensity at the screen:

$$I(x', y') = \left| \int\int g(k_x, k_y)t(k_x, k_y)E_S(k) \exp\left[-2\pi i(k_x x' + k_y y')\, \mathrm{d}k_x\, \mathrm{d}k_y\right] \right|^2. \tag{4.8}$$

The input file into MALTS is an *.omf* file specifying the x, y, and z magnetisation components at each mesh. Since Fourier Optics is required and Discrete Fourier Transforms are best performed on vectors of 2^N size where N is an integer, it is necessary to then *zero pad* the magnetisation matrix to a larger matrix of size 2^N. The user is able to decide the matrix size, provided that it exceeds the size of the inputted file, and hence can dictate the amount of zero padding. Zero padding is

considered physical if the electrons are incident on an area far larger than the magnetic structure actually occupies. In this case, larger amounts of zero padding are therefore in general more similar to the actual Lorentz TEM situation. Increasing the amount of zero padding leads to increased computational time, but even for a large matrix size of 2048 the entire image simulation process takes less than a minute.

The source code is provided for users who wish to study structures that are macroscopic in size i.e. larger than the simulation window. They are advised to implement their own boundary conditions carefully and they are referred to [82] and [83].

4.3 Validation

In order to test MALTS, comparisons were made with both experimental LTEM images and published LTEM simulations from other groups [4, 68, 69, 73, 74].

Fig. 4.3 shows the LTEM simulations from MALTS for exactly the same dimensions as specified in Qi's thesis [68] and displayed in Figure 3 of Qi et al. [4], i.e. a bar of permalloy, 512 nm long, 100 nm wide, and 22 nm thick, uniformly magnetised along its long axis as shown in Fig. 4.3 (a) & (b). Three different simulations were performed with different amounts of zero-padding of the matrix: 1) no zero-padding where the magnetisation extends to the left and right hand edges of the matrix (Fig. 4.3 (c) & (d)); 2) zero-padding to make the matrix twice as wide as the magnetic pattern (Fig. 4.3 (e) & (f)); and 3) zero-padding to make the matrix four times as wide as the element (Fig. 4.3 (g) & (h)). The zero-padding case in Fig. 4.3 (c) & (d) corresponds to the simulations performed by Qi et al. [4, 68]. The MALTS simulation without zero-padding shows good agreement with Qi et al.'s [4] simulation. It is striking that the inclusion of zero-padding such that the magnetic structure of interest is clear of the image edges significantly changes the simulated images Fig. 4.3 (e) & (f), compared to Fig. 4.3 (c) & (d). Once the magnetic structure is well within the image boundaries (at twice the largest dimension of the magnetic element), further zero-padding does not significantly alter the simulated images in Fig. 4.3 (g) & (h). All three cases exhibit the principal contrast feature of bright contrast on the upper and lower parts of the bar when the bar is magnetised to the left and right respectively,

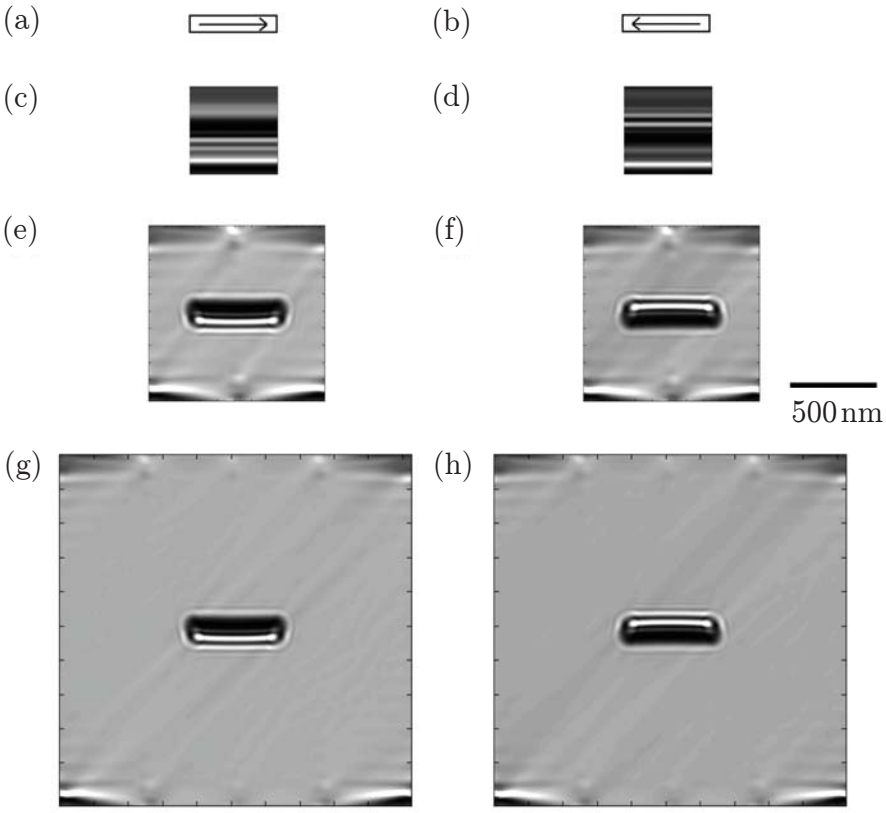

Figure 4.3: MALTS simulations of Lorentz TEM images showing the effects of zero padding for a uniformly magnetised permalloy bar of thickness 22 nm, lateral dimensions 512 nm × 100 nm and a mesh size of 1 nm, as specified in Qi's thesis [68]. (a) & (b) show the magnetisation directions of the bars used for the simulations. (c) & (d) show the corresponding LTEM simulations for a matrix size of 512 × 512 (corresponding to an area of 512 nm×512 nm), (e) & (f) for matrix size 1024 × 1024 and (g) & (h) for 2048 × 2048. When the bar is magnetised in the right (left) direction, bright contrast is seen on the lower (upper) side of the bar. An accelerating voltage of 300 kV, a defocus of 1600 µm, a spherical aberration of 0 m, and a beam divergence of 0.01 mradians were used for the simulations.

which is sufficient to correctly attribute the LTEM image in such a simple case. However in the analysis of more complex structures it is important to place the features of interest well away from the edges of the matrix to avoid confusing real contrast with edge effects arising due to the assumption of periodicity in the fast Fourier transform.

MALTS was also used to obtain LTEM simulations of four domain flux closure

states in a 1 µm × 2 µm rectangular element of 20 nm thickness. Four defocus values, 5 µm, 100 µm, 1500 µm, and 10000 µm, were chosen to facilitate comparison between MALTS (see Fig. 4.4) and the simulations of McVitie and Cushley's Figure 9 [69].

For defocus values of 5 µm (Fig. 4.4 (c) & (d)) and 100 µm (Fig. 4.4 (e) & (f)) the MALTS simulations are in excellent agreement with McVitie and Cushley's [69]: filamentary bright or dark fringes mark the borders between domains of differently oriented magnetisation for the cases of clockwise or anticlockwise rotation of the magnetisation respectively. As expected for Fresnel mode LTEM, inverting the sign of the magnetisation changes bright lines to dark and vice versa. This agreement between MALTS' and McVitie and Cushley's simulations [69] does not extend to the largest defocus of 10000 µm (Fig. 4.4 (i) & (j)). However, similar contrast between MALTS' simulation at a defocus of 1500 µm (Fig. 4.4 (g) & (h)) and theirs at 10000 µm was seen. The disparity at this very large value of defocus could be due to the use of different values for the beam divergence; McVitie and Cushley [69] do not state what value they use. Another possible reason for this discrepancy is the use of different approximations in the respective software, e.g. the envelope function used, which again McVitie and Cushley [69] do not specify.

Phatak et al. [73] reported that tilting the sample enabled the study of a vortex core's polarity in nanodiscs (described later in Section 7.2.1.1), i.e. the direction of the out-of-plane magnetisation, something the electrons would otherwise be insensitive to. Simulations were carried out with MALTS under similar conditions, excluding the introduction of local magnetocrystalline anisotropy in the vicinity of the core.

Fig. 4.5 (a) - (d) show the contrast obtained from anticlockwise chirality up polarity, anticlockwise chirality down polarity, clockwise chirality up polarity and clockwise chirality down polarity nanodiscs respectively, at a tilt of 34° about the x-axis. (Up and down polarity are defined as being in the positive and negative z-direction respectively, see Fig. 4.1.) These images have a dark or bright core for anticlockwise or clockwise chirality, in agreement with the results of Phatak et al. [73]. Differences in the contrast can be seen for the same chirality but different polarity configurations. The plots of the intensity variation along a line through the core shown in Fig. 4.5 (e) & (f) show that the polarity affects both the position of the core and the profile of

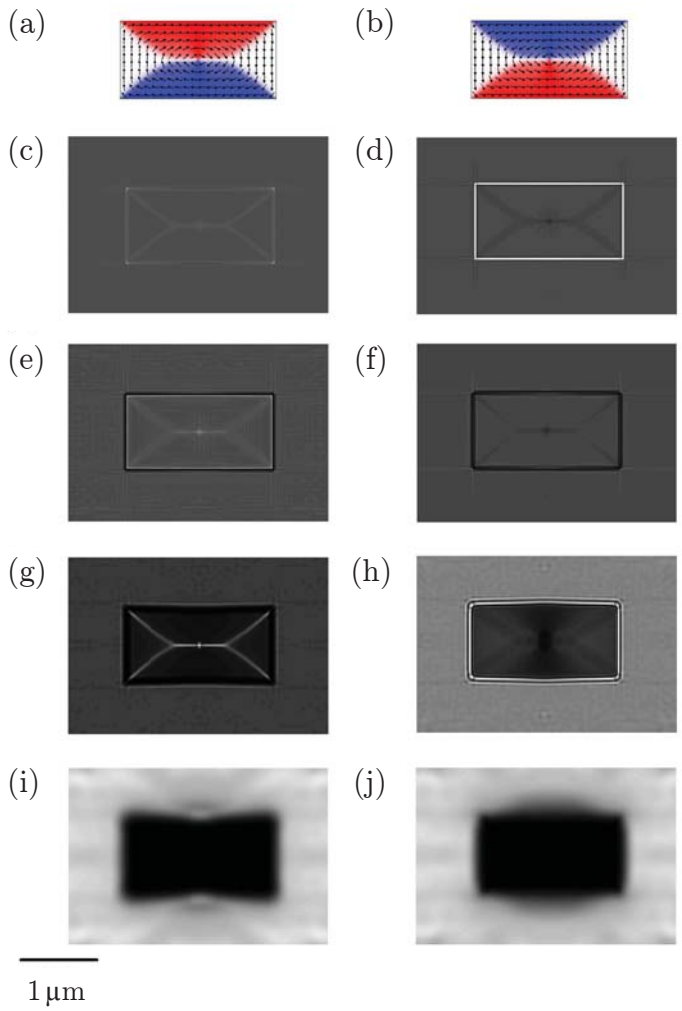

Figure 4.4: Micromagnetic simulation of (a) clockwise and (b) anticlockwise four-domain flux-closure states in rectangular 1 µm × 2 µm × 20 nm thick permalloy nanostructures, corresponding to the dimensions used by McVitie and Cushley [69]. The red and blue colours indicate magnetisation in the positive and negative x-directions respectively. (c) - (j) MALTS LTEM simulations for the magnetic state in (a) & (b) in the left and right hand columns respectively. For comparison with Figure 9 of [69], images at defocus (c) & (d) 5 µm, (e) & (f) 100 µm, (g) & (h) 1500 µm and (i) & (j) 10000 µm were produced. An accelerating voltage of 200 kV, a C_S of 8000 mm, and a beam divergence of 0.01 mradians were used. The mesh size was 5 nm and the matrix size used for zero padding was 1024.

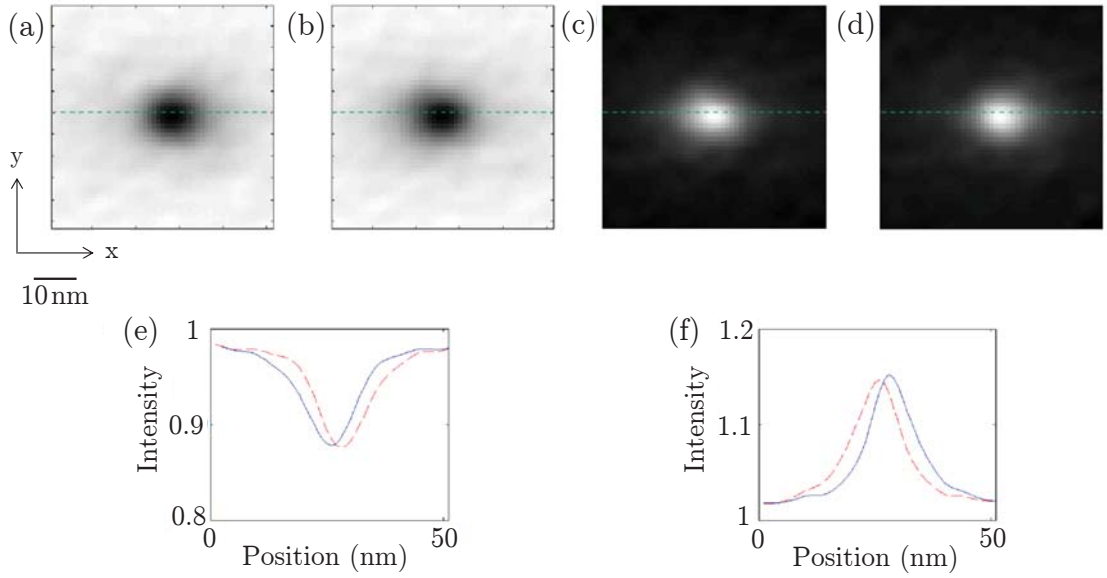

Figure 4.5: MALTS simulations of LTEM images for a 15 nm thick nanodisc of 250 nm radius with exchange constant $A = 30.2\,\mathrm{pJm^{-1}}$, $M_S = 1592\,\mathrm{kAm^{-1}}$ (2 T), and mesh size 1 nm, matching the parameters for similar simulations performed by Phatak et al. [73]. An accelerating voltage of 200 kV, a C_S of 1 m, a beam divergence of 0.01 mradians and a defocus of 5 µm were used. The matrix size was 1024 × 1024. (a), (b), (c), and (d) show the contrast obtained at a 34° tilt about the x-axis when an anticlockwise vortex with up polarity, an anticlockwise vortex with down polarity, a clockwise vortex with up polarity and a clockwise vortex with down polarity respectively are simulated. The green dotted line indicates where the cross sections of intensity in (e) & (f) have been taken. The red dashed and blue solid lines in (e) & (f) indicate the cross sections through (a) & (b) in (e) and (c) & (d) in (f) respectively.

the intensity peak. The latter effect was also observed by Phatak et al. [73]. However, they do not mention any shift of the core and it is difficult to tell from their figures whether their simulations also produced this effect [73]. However Ngo and McVitie [74] illustrated a new approach to determining the core polarity in nanodiscs, albeit of slightly different dimensions (600 nm diameter and 20 nm thick) to Phatak et al. They suggested that, by subtracting the contrast of an LTEM image taken at negative tilt from one taken at positive tilt, the core's polarity could easily be ascertained: this created a white-and-black spot in which the relative positions of the white

and black contrast depend on the polarity. MALTS simulations in Fig. 4.6 support this methodology; Fig. 4.6 (a) & (b) show the difference images for nanodiscs of the same anticlockwise chirality but different polarity ((a) up, (b) down) between +30° and −30° tilt, clearly demonstrating the inversion of the black-and-white contrast for different polarity cores. The relative position of the black and white spots for a given polarity is reversed for the MALTS simulation compared to Ngo and McVitie [74]. It is assumed that this is due to a different assignment of the positive tilt direction. Fig. 4.1 shows MALTS' definition of positive tilt direction. Ngo and McVitie [74] do not explicitly define theirs. Fig. 4.6 (c) & (d) show the intensity profiles across the core in the situations of no tilt, +30° tilt and −30° tilt, as well as the difference between the latter two tilts.

Comparison of MALTS simulations with experimental Fresnel mode LTEM images of two more complex nanostructures taken by Solveig Felton was also carried out. The first structure is a set of five nanobars (100 nm × 1000 nm), relaxed in a saturating field in the negative x-direction, in a double-Y shaped geometry (Fig. 4.7 (a)) and the second is a cross structure consisting of four 1 µm × 3 µm rectangular elements connected by 100 nm wide lines (Fig. 4.7 (b)). MALTS simulations are shown in Fig. 4.7 (c) & (d). Both structures were manufactured using e-beam lithography, thermal evaporation of a 20 nm thick permalloy layer, and lift-off on a 50 nm thick membrane for TEM from Agar Scientific (see Section 3.1) by Katharina Zeissler (Fig. 4.7 (e) & (f)). A 5 nm layer of Au was sputtered onto the sample to avoid charge build up under the electron beam. Good agreement between simulation and experiment was achieved in both cases, although the simulation images were sharper. This may be explained by the fact that the simulation only takes into account the magnetic permalloy layer, while in the experimental case further scattering of the electron beam may take place in the membrane and the Au film.

The five nanobar structure (Fig. 4.7 (c)) showcases the ability of MALTS to reproduce single domain contrast, such as that simulated by Qi et al. [4,68] in more complex structures. The cross structure (Fig. 4.7 (d)) takes this one step further demonstrating that MALTS can simultaneously produce the traditional domain-boundary contrast associated with Fresnel mode LTEM as well as single domain contrast in

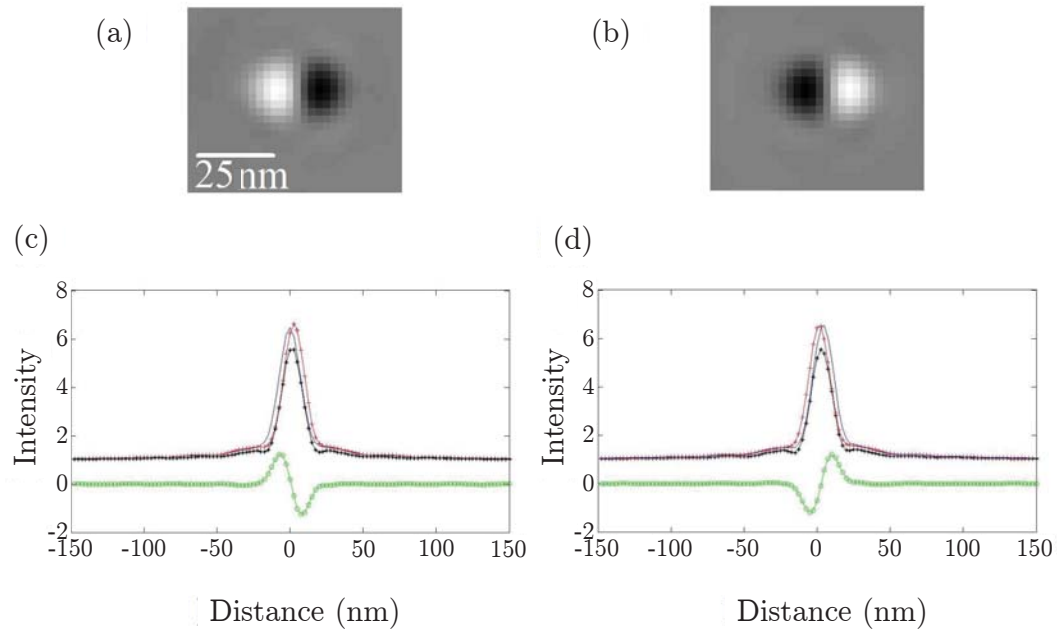

Figure 4.6: MALTS simulations of LTEM images for 20 nm thick nanodisc of 600 nm diameter with exchange constant $A = 13\,\mathrm{pJm^{-1}}$, $M_S = 860\,\mathrm{kAm^{-1}}$ ($\approx 1\,\mathrm{T}$), and mesh size 2.5 nm, matching the parameters for similar simulations performed by Ngo and McVitie [74]. An accelerating voltage of 200 kV, a C_S of 8000 mm, a beam divergence of 0.01 mradians and a defocus of 250 µm were used. The matrix size was 1024×1024. (a) & (b) show the difference contrast obtained between a $+30°$ and a $-30°$ tilt about the x-axis when (a) an anticlockwise vortex with up polarity and (b) an anticlockwise vortex with down polarity are simulated. (c) & (d) show the intensity profiles across the core for an anticlockwise vortex with up polarity and clockwise vortex with down polarity respectively. The black asterisked line shows the intensity profile at zero tilt. The red crossed line and the blue line show the profiles at $+30°$ and at $-30°$ tilt respectively. The green line with open circles shows the difference between the intensity profile at $+30°$ and at $-30°$ tilt. The relative position of the black and white spots for a given polarity is inverted in these simulations compared to those of Ngo and McVitie [74], which is assumed to be due to a different definition of positive tilt direction.

relatively large structures. For the cross structure a mesh size of 10 nm was used in the OOMMF simulation. It is recognised that this is on the large side but this choice of mesh size was due to the limitation of memory for the installation of OOMMF. Since the resulting MALTS simulation reproduces the experimental contrast well, this mesh size was considered acceptable in this particular case. As a general comment,

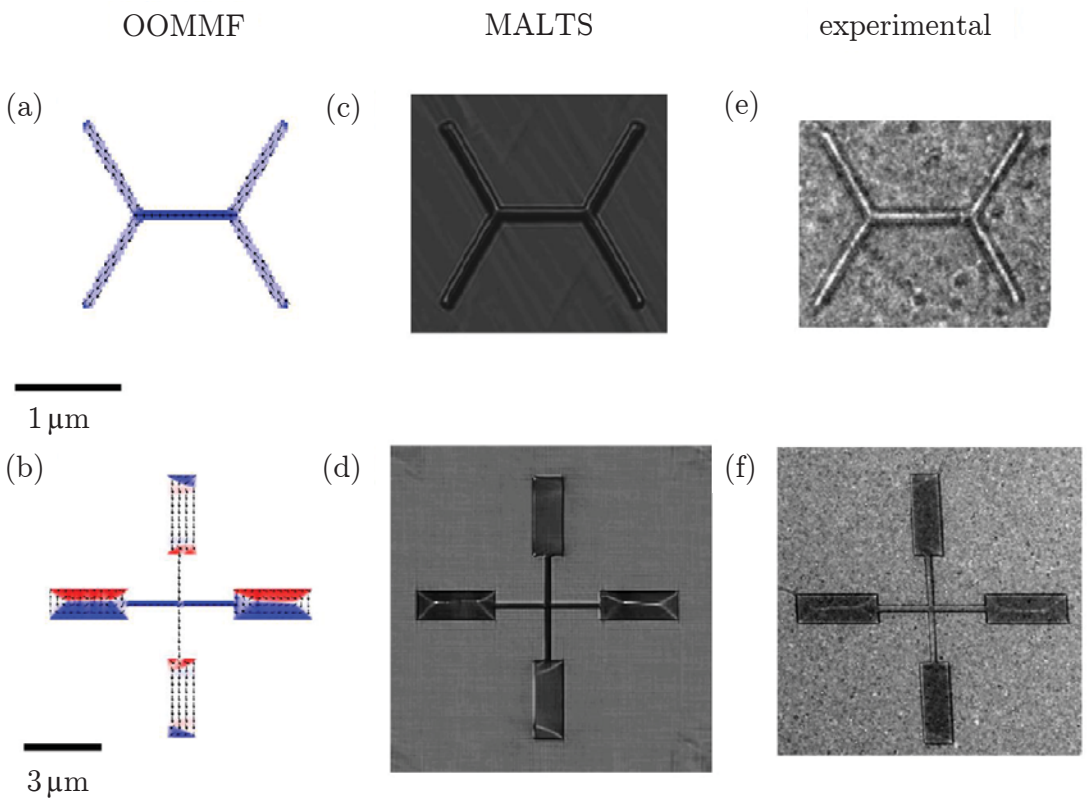

Figure 4.7: Comparison of experimental LTEM data with images simulated by MALTS for 20 nm thick permalloy nanostructures. The micromagnetic states of (a) five bars saturated in the negative x direction and (b) a cross structure with both single domain and flux closure behavior, were simulated using OOMMF. The red and blue colours indicate magnetisation in the positive and negative x directions respectively. (c) & (d) LTEM simulations using an accelerating voltage of 300 kV, a defocus of 1.5 mm, a C_S of 0 m, and a beam divergence of 0.01 mradians and a matrix size of 2048. Mesh sizes of 2.5 and 10 nm were used for the five bars and the cross structure respectively. (e) & (f) experimental LTEM images obtained using an accelerating voltage of 300 kV and a defocus of 1.5 mm. Experimental contrast was analysed by eye or, where necessary due to ambiguity, with intensity cross sections.

the memory limitation does not carry through to MALTS, which could simulate the larger matrix required for a finer mesh.

4.4 Using MALTS

MALTS is a standalone executable which is used in conjunction with the publicly available OOMMF [18] or MuMax [63] software. MALTS is available as a 32 or 64 bit compiled version at *http://www3.imperial.ac.uk/people/w.branford/research* with an accompanying user manual and MCR installer, as well as MATLAB source code. Supplying MALTS as open source enables users to extend the functionality of the software, including adding other imaging modes such as Foucault should this be desired. MATLAB was chosen as the programming language because it is designed for matrix manipulation and has inbuilt graphing functions. MALTS requires one input text file from OOMMF or MuMax as well as the user defined values used to compute this file: material thickness, mesh size and number of meshes. In addition experimental values, *beam divergence*, *defocus*, *spherical aberration* and *accelerating voltage* specific to individual experiments may be varied. The user can also choose the size of the calculation matrix and thereby the amount of zero padding of the magnetic structure. The sample may be tilted in the simulation about any axis in the xy-plane. The resulting LTEM contrast is displayed on the Graphical User Interface and saved automatically. To aid in determining the origin of the LTEM contrast, images can also be simulated using only the electric or only the magnetic phase by selecting the *Electric Component LTEM* button or by setting the mean inner potential to zero respectively.

4.5 Summary

In this chapter the development of MALTS, a tool to simulate Lorentz Transmission Electron Microscopy contrast, has been documented. The computational methodology behind MALTS has been detailed in full, and a rigorous comparison with both experimental images and simulated LTEM contrast obtained from other groups has been made. In addition, information about how to obtain and use MALTS has been provided.

In the following chapter, the field-driven magnetic reversal of Artificial Spin Ice

is explored via Scanning Transmission X-ray Microscopy. However further examples of MALTS' usefulness are shown in Chapters 6 & 7 in which the LTEM contrast of vortex domain walls at ellipsoidal holes is predicted and the LTEM contrast from single domain nanodiscs is interpreted respectively.

CHAPTER 5 : DOMAIN WALL TRAJECTORIES IN ARTIFICIAL SPIN ICE

An introduction to Artificial Spin Ice (ASI), an array of ferromagnetic nanobars in a kagome geometry, was provided in Section 2.10.3. ASI undergoes magnetic reversal via domain wall nucleation and propagation. The simple charge model presented in Section 2.10.3.1 can be used to explain some features of this magnetic reversal, specifically cascade behaviour. This model however assumes that the charge carrying domain wall is a perfectly symmetrical disc. This, however, is not the case since the domain wall has a distinctive non-symmetrical shape. As discussed in Section 2.6, domain walls typically employ a transverse or vortex shape depending on the dimensions of the nanobar. If the domain wall employs a transverse shape it has one of two chiralities, up or down and if it employs a vortex shape, it has one of two chiralities, clockwise or anticlockwise. In this chapter experimental evidence that suggests that the domain wall chirality affects the direction of propagation of domain walls in the early stages of magnetic reversal in the transverse domain wall regime is presented. The discussion surrounding this very attractive result is adapted from a paper published in *Scientific Reports* written jointly by myself, Katharina Zeissler and Will Branford [84]. In addition, in light of the recent publication by Pushp & Phung et al. [85], an analysis of experimental data in the vortex domain wall regime is also presented. This discussion is adapted from a paper written by myself, Katharina Zeissler, David Burn, Will Branford and Lesley Cohen which is to be submitted for publication soon.

5.1 Decisions at Y-shaped junctions

In Section 2.10.3.1 a simple charge model was introduced in which the ASI nanobars' coercivities are described in terms of the charge configuration at their adjacent vertex, their quenched disorder and their orientation with respect to an external magnetic field. With finite quenched disorder, the nanobars in ASI all have different coercivities. Magnetic reversal in ASI starts with the reversal of the nanobar with the lowest coercivity. In this chapter the situation in which magnetic reversal proceeds under the influence of a magnetic field aligned parallel to one of the ASI sublattice directions after an initial saturation in the opposite direction is considered. With reference back to the tables in Section 2.10.3.1, in the limit of negligible quenched disorder, it can be seen that the external field required to nucleate a domain wall at an arbitrary position within the lattice is significantly greater ($H_c = 3 \times \frac{M_S tw}{4\pi a^2}$ for horizontal nanobars or $H_c = 2 \times \frac{M_S tw}{4\pi a^2}$ for non-horizontal nanobars) than both the external field required to nucleate at an edge site ($H_c = 0 \times \frac{M_S tw}{4\pi a^2}$ for non-horizontal nanobars) and the external field required to transmit a pre-existing domain wall down a nanobar ($H_c = 1 \times \frac{M_S tw}{4\pi a^2}$ for horizontal nanobars or $H_c = 0$ for non-horizontal nanobars). While there will always be hysteresis in a real ferromagnetic material, it is clear from this model why the majority of the nanobars in the array switch by the edge nucleation and subsequent propagation of a small number of domain walls. This mechanism, which results in cascades of switched nanobars, is illustrated in Fig. 5.1.

In the cascades described above and illustrated in Fig. 5.1, the propagating charged domain wall repeatedly arrives at Y-shaped junctions where it is forced to select between two apparently equivalent paths. In the simple charge model one would expect the domain wall to take the upward and downward path with equal probability and hence execute a random walk. The following sections describe the investigation into whether these two different paths are indeed equally favoured by the domain wall in both the transverse and vortex domain wall regimes. The exact experimental and simulational details of this investigation are given below.

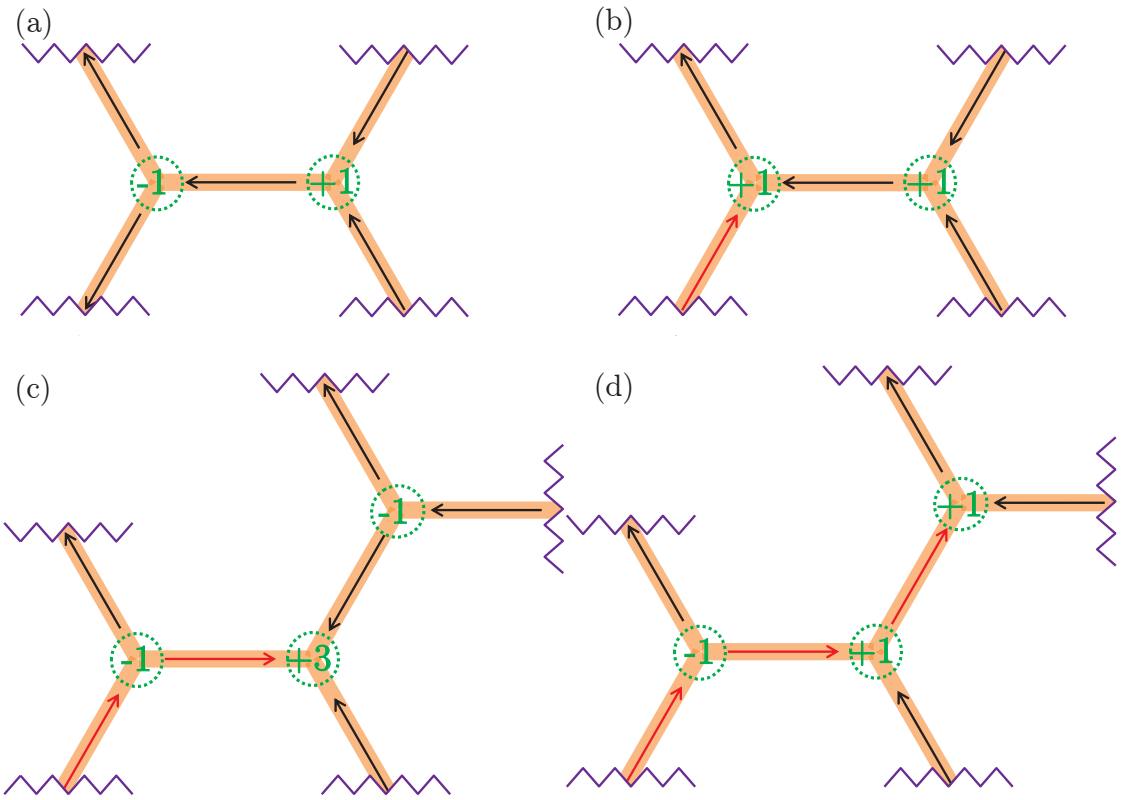

Figure 5.1: Cascade behaviour schematic for magnetic field parallel to one ASI sublattice direction. (a) shows the initial magnetisation state after saturation in the left hand direction. The field required to reverse the horizontal bar is large in (a) ($H_c = 3 \times \frac{M_S t w}{4\pi a^2}$) but reduced in (b) ($H_c = 1 \times \frac{M_S t w}{4\pi a^2}$) once an adjacent non-diagonal nanobar has been switched. The horizontal bar then switches, shown in (c), causing the subsequent switching of a further adjacent non-horizontal bar shown in (d).

5.2 Investigative details

5.2.1 Sample fabrication

ASI samples were fabricated by electron-beam lithography on SiN membranes, thermal evaporation of permalloy, $Ni_{81}Fe_{19}$, and a lift-off processing technique (see Section 3.1). Atomic Force Microscopy (AFM) (see Section 3.2.7) was used to measure the sample's thickness. Samples were fabricated at thicknesses of 18 ± 1 nm and 36 ± 1 nm,

in order to probe the reversal of systems in the transverse and the vortex domain wall regime respectively.

5.2.2 Scanning Transmission X-ray Microscopy

Scanning Transmission X-ray Microscopy experiments (see Section 3.2.4) were carried out at Beamline 11.0.2 of the Advanced Light Source, Berkeley, CA, USA. The membrane was mounted between the pole pieces of an electromagnet allowing for an in-plane field of ±250 mT in situ. This system was placed approximately 30° with respect to the X-ray propagation vector in order to see in-plane MCD contrast. The chamber was pumped down to 100 mTorr before filling with helium gas to reduce absorption [86]. An elliptically-polarising undulator delivered photons in the range 80 eV to 1900 eV to the branchline. A fast shutter between the exit slit and STXM was used to minimise sample radiation damage. X-rays of energy 852.6 eV were focussed by diffraction to a spot size of 30 nm via Fresnel plates.

Room-temperature STXM studies were carried out on the two samples. In order to study the magnetic reversal of the ASI arrays, the sample was first saturated in the positive x direction, and then incrementally increasing smaller fields were applied in the negative x direction.

5.2.3 Micromagnetic Simulations

Micromagnetic simulations (see Section 3.3) were performed with the OOMMF [18] software with a lateral mesh size of 5 nm unless otherwise stated. The simulations were performed at absolute zero temperature. The magnetocrystalline anisotropy of $Ni_{81}Fe_{19}$ was assumed to be zero, the exchange constant was taken to be $1.3 \times 10^{-11}\,Jm^{-1}$, and the saturation magnetisation was taken to be $800\,kAm^{-1}$. Where necessary, domain walls were introduced into the OOMMF simulation and their chirality preconditioned via a colour map. In Section 5.4, the Gilbert damping parameter was taken to be $\alpha = 0.5$ in order to minimise simulation time. In Section 5.5, however, accurate dynamical simulations were required for direct comparison with the literature [85]. Therefore in these simulations the Gilbert damping parameter was

taken to be $\alpha = 0.01$.

5.3 Method

Domain wall propagation directions were studied during the magnetic reversal of permalloy ASI. Individual switching chains were identified in stepwise reversed ASI arrays. Fig. 5.2 (a) shows a typical ASI array mid-reversal. White and black XMCD contrast identifies magnetisation along the positive and negative x-axis respectively. The origin of an individual chain was defined as $(0, 0)$ and the y displacement was tracked until the chain terminated or branched out (see Fig. 5.2 (b)).

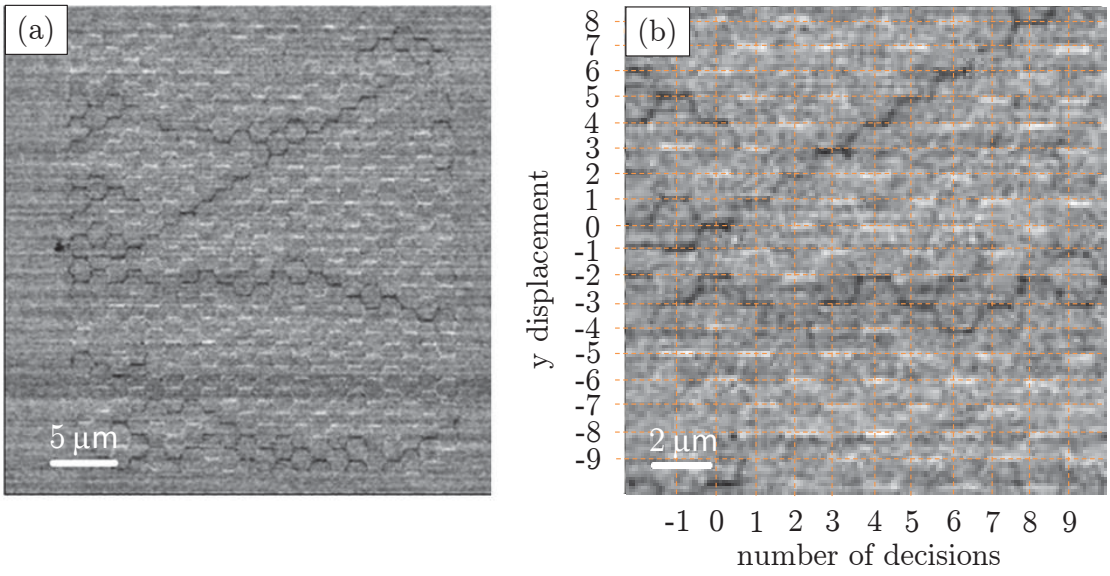

Figure 5.2: Mapping the paths of domain walls. (a) a typical STXM image for a partially switched 18 nm thick ASI with 100 nm wide and 1 µm long bars. The array was initially saturated along positive x and then a -9.25 mT field was applied in the negative x direction. White contrast indicates magnetisation in the positive x direction, black contrast indicates magnetisation in the negative x direction. (b) a magnified region of (a) illustrating the counting method used. The beginning of the chain, the first identifiable horizontal bar, was defined as $(0, 0)$. The coordinates of each other bar in the chain were defined with respect to this origin as shown on the axes.

5.3.1 Exact binomial test

In order to test for correlation between two sequential decisions, the number of incidences in which the domain wall took the same path, i.e. up then up ($\Delta y = +2$) or down then down ($\Delta y = -2$), and different path, i.e. down then up ($\Delta y = 0$) or up then down ($\Delta y = 0$), was noted. In an entirely random walk situation this result should be binomially distributed with probability 0.5. As such, an *exact binomial test* was performed on the data in order to see if the domain walls performed random walks. The one-tailed *p-value* achieved from this test quantifies the probability that the random walk model would produce a data set for the total number of observations as far, or further, from the expected $50:50$ ratio. The null hypothesis that the domain walls followed a random walk was accepted if this *p-value* was less than 0.05 i.e. with a confidence interval of 5%. The results of these tests for nanobars with dimensions in both the transverse and vortex domain wall regimes are presented below and discussed in light of micromagnetic simulations performed on single ASI vertices.

5.4 Transverse domain wall regime: the non-random walk

Permalloy ASI arrays comprising nanobars of thickness 18 nm, width 100 nm, and length 1 µm and 2 µm were studied according to the method described above. Nanobars with these dimensions fall into the transverse domain wall regime. Each switched bar in an identified chain was labelled with an x (number of decisions occurred) and y (y displacement) coordinate according to Fig. 5.2 (b). The frequency of observations at each (x, y) coordinate, $N_{(x,y)}$, was noted. This was then divided by the number of observations at that (x, y) coordinate expected in a random walk scenario, $N_{RW(x,y)}$. This result, $N_{(x,y)}/N_{RW(x,y)}$, is displayed in Fig. 5.3 (a) & (b). If the random walk correctly describes the system a flat $N_{(x,y)}/N_{RW(x,y)} \approx 1$ distribution should be seen illustrated in a whitish colour. Instead a red colour is seen frequently at the edges where $|y|$ is large indicating more observations than expected there, and a blue colour is often seen at the centre where $|y|$ is small indicating fewer observations than expected there.

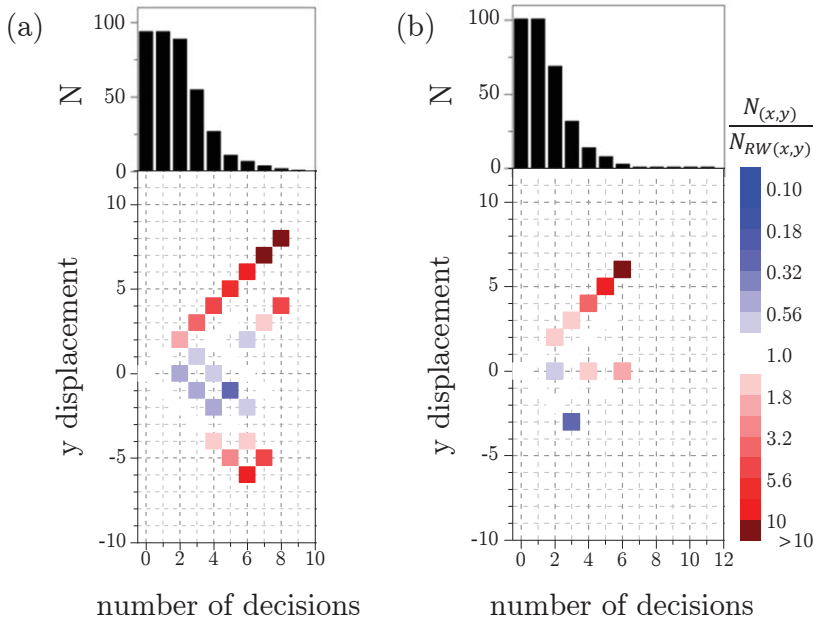

Figure 5.3: Distribution of observed domain wall paths during 180° magnetic reversals in 18 nm thick ASI nanobars of bar length (a) 1 µm and (b) 2 µm and width 100 nm. The black bar charts show the total numbers of switched bars, N, observed in the data sets after a given number of decisions. The frequencies of switched bars at each each (x, y) coordinate (corresponding to a y displacement after x decisions), $N_{(x,y)}$, divided by the number of switched bars expected at that coordinate in the random walk scenario, $N_{RW(x,y)}$, i.e. $N_{(x,y)}/N_{RW(x,y)}$, is shown here. $N_{(x,y)}/N_{RW(x,y)}$ is colour coded such that $N_{(x,y)}/N_{RW(x,y)} > 1$ and $N_{(x,y)}/N_{RW(x,y)} < 1$ are shown in red and blue and highlight more or fewer observations than expected for a random walk scenario.

When the two decision correlators were studied according to the method described in Section 5.3.1 it was found that, in the 1 µm long ASI nanobars, the domain walls retained their directions ($\Delta y = +2$ (up to up) or $\Delta y = -2$ (down to down)) in 124 out of 171 events, and in the 2 µm long ASI nanobars, the domain walls retained their directions in 76 out of 131 events (see Table 5.1 and Fig. 5.4). These two results yielded p-values of 1.7×10^{-9} and 0.04 in the one-tailed exact binomial test respectively. As such, under a confidence interval of 5%, the random walk null hypothesis was rejected for both data sets.

In order to understand this result, micromagnetic simulations were performed according to Section 5.2.3. Perfect selectivity was observed in the transverse domain

$(\Delta x, \Delta y)$	**1 μm**	**2 μm**
$(2, +2)$ u-u	68	56
$(2, 0)$ u-d	24	28
$(2, 0)$ d-u	23	27
$(2, -2)$ d-d	56	20
$(2, \pm 2)$ u-u, d-d	124	76
$(2, 0)$ u-d, d-u	47	55
Total	171	131
$p - value$	1.69×10^{-9}	0.040

Table 5.1: Summary of the two bar correlator results (see Section 5.3.1) in the transverse domain wall regime for bar lengths 1 μm and 2 μm. The p-values shown are for one-tailed exact binomial tests.

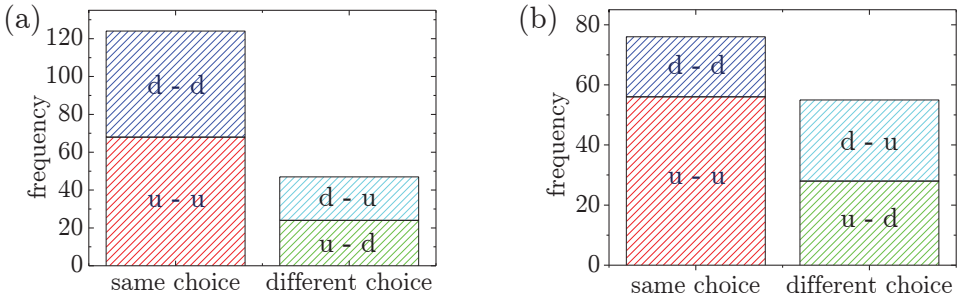

Figure 5.4: Graphical representation of two bar correlator data (see Section 5.3.1) in the transverse domain wall regime summarised in Table 5.1. Data is displayed in bar graphs (a) for 1 μm and (b) for 2 μm long nanobars. u-u, u-d, d-u and d-d correspond to $(\Delta x, \Delta y)$ of $(2, +2)$, $(2, 0)$, $(2, 0)$ and $(2, -2)$ respectively.

wall regime. A domain wall which propagated through the horizontal bar was seen to result in the switching of the $+60°$ (upper) or $-60°$ (lower) diagonal bar depending on whether it was of up (Fig. 5.5 (a)) or down (Fig. 5.5 (b)) chirality. During their transit through these diagonal bars the domain walls were subsequently distorted and the Zeeman force aligned the moment of the walls with the external field (Fig. 5.5 (c) & (d) i)), effectively resetting the chirality of the transverse domain wall between each horizontal bar. However Fig. 5.5 (c) ii) & (d) ii) show that the chirality depinning from the vertex next in line depended on whether the domain wall arrived from the lower branch or the upper branch. A domain wall arriving from the lower branch

depins as an up transverse domain wall (Fig. 5.5 (c)) and a domain wall arriving from the upper branch depins as a down transverse domain (Fig. 5.5 (d). In this way the chirality of the domain wall entering the second bar parallel to the field was determined by the chirality of the wall that exited the first parallel bar. Thus, chiral information can pass through the array as the domain wall continues to propagate, even though the chirality of the wall is reset in the intervening bar at $\pm 60°$ to the field. This leads to domain wall propagation paths that deviate from the random walk model. More specifically, this could explain why an unexpectedly high occurrence of long unidirectional chains were observed during 180° reversals.

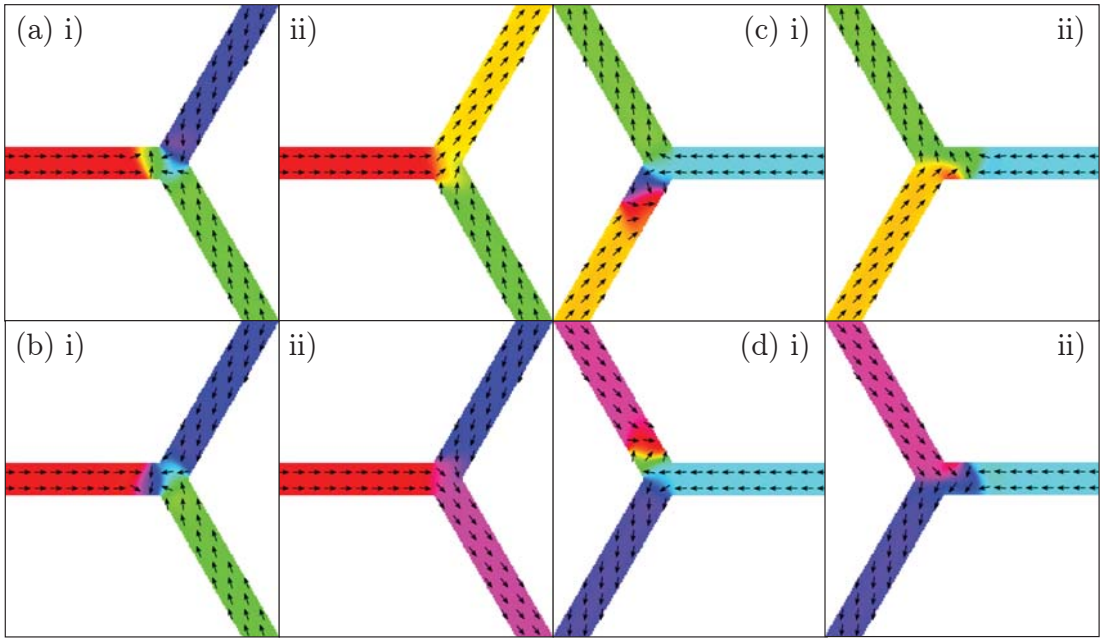

Figure 5.5: Micromagnetic simulations [18] of domain wall movement through an ASI vertex with thickness 18 nm and width 100 nm. The switching is driven by an applied field in the $+x$ direction after saturation in the $-x$ direction. The initial and final states show the magnetic structure before and after the domain wall has crossed the vertex. Switching via a transverse domain wall with (a) up chirality (i) converged state at 350 Oe, ii) converged state at 360 Oe) and (b) down chirality is shown (i) converged state at 290 Oe, ii) converged state at 300 Oe). Switching from the lower and upper diagonal bars and the subsequent formation of an up or down chirality transverse domain wall are shown in (c) & (d) respectively (non-converged states at 350 Oe).

5.4.1 Discussion

The data showed that in total, more domain walls took an upward branch than a downward branch. However, the data comes from the same series of runs on arrays grown on the same membrane without changing the sample and magnet mounting (aligned by eye with an error of less than 5°). This overall asymmetry could be related to field misalignment, or even something systematic in the sample fabrication that favours asymmetric domain wall nucleation (no such asymmetry is apparent in the images). However in the data (Table 5.1) a much greater intensity than expected from a random walk model in both the $+y$ and $-y$ extremities is seen for a single sample alignment. A typical illustration of this can be found in Fig. 5.2 (a). This cannot be explained by field misalignment. The magnetisation versus external field is plotted in Fig. 5.6 (a) and shows a sharp reversal without any plateaux. This also indicates that the field misalignment is not the source of selectivity and systematic fabrication imperfections do not dominate the reversal. Note that in the (zero temperature) simulations it is not possible to introduce a partial bias with field misalignment; no effect is seen at small angles, and perfect selectivity is seen at greater misalignments, with the crossover at about 7°. The combination of field misalignment with temperature or quenched disorder may be able to produce a biased random walk distribution, and is a possible explanation for the overall asymmetry between up and down in the statistics. However it is stressed that both the $+y$ and $-y$ extremities are strongly favoured over the random-walk model in data sets collected from a single sample mounting, and a bias to both extremes cannot be simply a matter of alignment.

The micromagnetic simulations suggest that the domain wall chirality breaks the symmetry of the Y-shaped junction and causes directional selectivity. A closer look at the magnetic configuration near the vertex shows which chirality favours which path. As the domain wall approaches the vertex it affects the local magnetisation in and around the vertex. In both transverse cases a *C*-like state (an intermediate state of low exchange energy cost seen in nanodiscs of certain dimensions [87]) is stabilised near the vertex, but the location of the C-like state depends on the chirality. In the up chirality situation, the C-like state is stabilised over the upper and horizontal

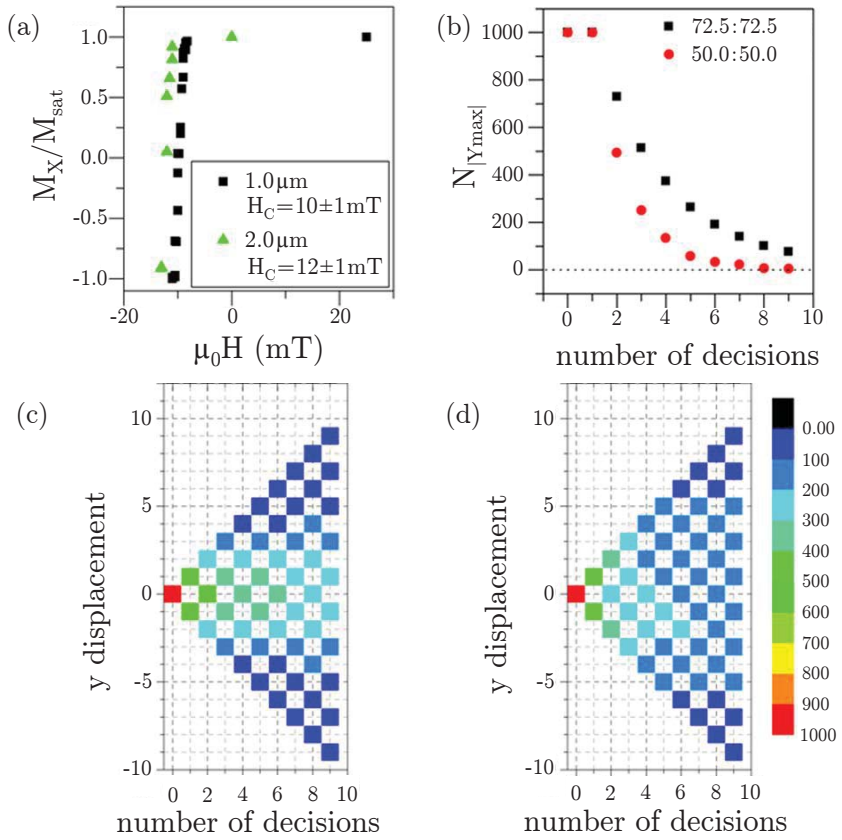

Figure 5.6: (a) room temperature magnetisation reversal after initial saturation in the positive x direction of ASI arrays. The normalised magnetisation is calculated by summing the number of bars with a particular STXM magnetic contrast (Fig. 5.2) and dividing by the total number of bars. Sharp magnetic reversal without any plateaux indicates that there is no field misalignment and that any fabrication defects have an insignificant influence on the switching. (b) expected number of observations at the outermost possible path ($N_{|Y_{max}|}$) after 1000 random walks and biased random walks. The colour-coded full path distribution is shown in (c) for random and (d) for biased random walks. The biased random walk model assumes that there is no overall preference for $\Delta y = \pm 1$ but that a subsequent decision is correlated with the immediately preceding decision. The apparent bias factor from the 1 μm experimental two decision correlation data of 72.5:27.5 (i.e. 124:47 from Table 5.1) was used.

bars, which is an equivalent situation to the nucleation of a domain wall in the upper branch (Fig. 5.5 (a)). Conversely, in the down chirality situation, the C-like state is stabilised over the lower and horizontal branches, equivalent to the nucleation of

a domain wall in the lower branch (Fig. 5.5 (b)). As the field is increased it is these domain walls that propagate through the array causing directional selectivity (illustrated in Fig. 5.7).

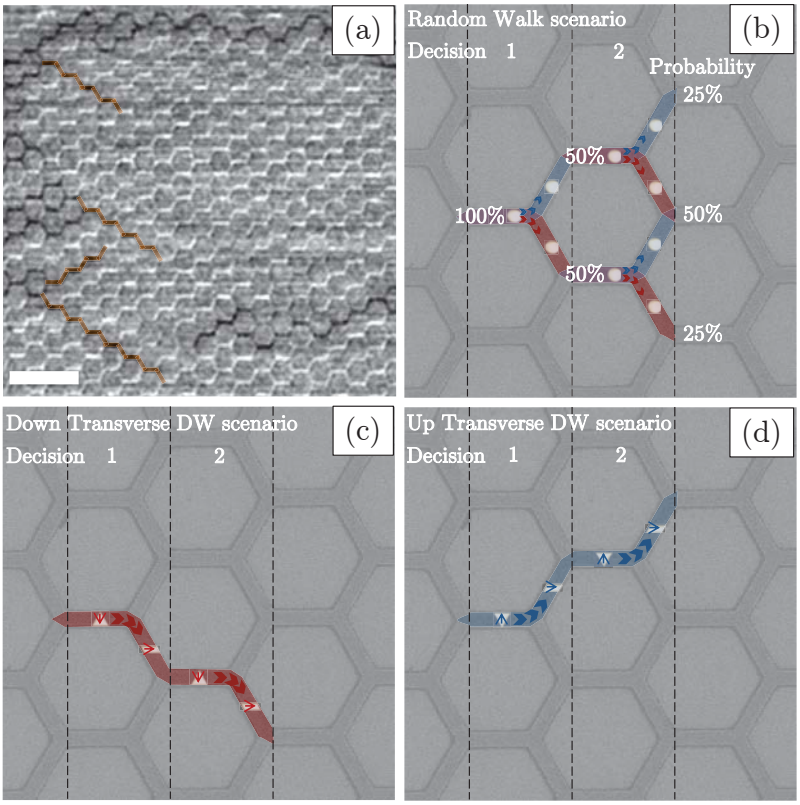

Figure 5.7: Domain wall movement through permalloy ASI (a) XMCD image (white contrast indicates magnetisation in the positive x direction, black contrast indicates magnetisation in the negative x direction) with long unidirectional chains of switched (black) bars highlighted in orange. The scale bar represents 5 µm. (b) schematic showing the random walk scenario which is expected if domain walls are portrayed as point-like magnetic charges moving through the structure. At each junction there is a 50 : 50 chance of taking the ±60° bar. However when the true shape of the domain walls is considered, in this case transverse domain walls, then the non uniform magnetic moment distribution affects the propagation path. (c) & (d) schematics illustrating the down and up chiral transverse domain wall cases respectively.

Despite these transverse domain wall dependent switching rules, the reversal is still a potentially stochastic process as a domain wall travelling through a nanobar

can undergo Walker Breakdown. Walker Breakdown refers to the change of domain wall chirality via intermediate states when the domain wall is forced to propagate down a nanobar due to an externally applied magnetic field [20, 88]. There are three identifiable regimes as a function of field in the Walker Breakdown mechanism. Below the Walker field, H_W, ($H < H_W$) the transverse domain wall propagates down the nanobar without deformation. Just above H_W ($1 < \frac{H}{H_W} < 5.5$) the chirality periodically changes from up to down transverse domain walls via the formation of an antivortex domain wall. And at high fields ($\frac{H}{H_W} > 5.5$) the transverse domain wall chirality changes via multivortex and multiantivortex states [89, 90]. Theoretical calculations predict the Walker Breakdown field to be $H_W \approx 6.5\,\mathrm{Oe}$ at zero temperature for perfectly smooth nanobars, 100 nm wide and 18 nm thick [91], which would place these structures well into region 3. The fidelity length, the length up to which the chirality is preserved, is predicted to be 0.5 µm [90] for simulations carried out at 0 K. Room temperature experiments on permalloy nanobars (90 nm wide, 12 nm thick) measured a fidelity length of $\approx 0.4\,\mu\mathrm{m}$ in a 100 Oe field [92]. However edge roughness can increase H_W, suppressing the onset of Walker Breakdown [93] and the observations suggest that this might be the case. With a bar length of 1 µm some Walker Breakdown is expected, manifested in the washing out of the selectivity produced by the chirality rule. However as 72.5% selectivity remains in the data, the edge roughness might be sufficiently suitable for Walker Breakdown to be suppressed in a majority of the nanobars. Selectivity decreases severely for the ASI with bar length of 2 µm emphasising the influence of Walker Breakdown.

Statistically insignificant numbers of long chains of switched bars were seen in the arrays (see Fig. 5.3). Long chains can only be tracked at early stages in the reversal since later on, there are many domain walls in the array and it is hard to infer which domain wall switched which bar. In order to improve the statistical viability of the study by witnessing more long chain events, it would be advantageous to have larger arrays or to restrict the number of domain walls in the arrays, perhaps by suppressing domain wall nucleation at some edge vertices.

A simulation was performed to demonstrate the differences in the distributions of switched bars expected from both a pseudorandom walk and a pseudorandom

biased walk. In the latter case, the first pseudorandom decision was unbiased (50 : 50) and each subsequent decision was pseudorandom with a bias of 72.5 : 27.5, the apparent bias factor from the 1 μm experimental two decision correlation data (i.e. 124 : 47 from Table 5.1). For example, if the first decision resulted in the switching of the upper bar then there was a 72.5% likelihood that the next decision resulted in the switching of the next upper bar. Simulations of 1000 random walks undergoing nine consecutive decisions were performed and the results of this study are shown in Fig. 5.6. As expected, it was observed that the addition of a bias resulted in a greater population of switched bars at the extremities and a reduced population of switched bars around a y displacement of zero compared to the random walk scenario; witnessing a unidirectional chain of 8 decisions was nearly 20 times more likely in the biased situation than it was in the random walk. This is consistent with the hypothesis that the domain walls perform a biased random walk in the transverse domain wall regime in ASI.

In this section the observation of a non-random walk of domain walls in the transverse domain wall regime has been presented and discussed in detail. In the following section a similar investigation into the propagation paths of domain walls in the vortex domain regime is presented.

5.5 Vortex domain wall regime: the random walk

In the previous section it was shown that that the domain walls in the transverse regime propagating through ASI nanobars of dimensions 100 nm × 1 μm × 18 nm did not follow a random walk and instead showed a strong element of selectivity. It was proposed that it was the chirality of the domain wall, up or down, which provided this symmetry breaking element. In addition, it was asserted that Walker Breakdown, the mechanism by which a domain wall's structure may be altered during propagation, was the source of the randomness in the data. These results were published in Scientific Reports early in 2013 [84].

More recently Pushp & Phung et al. [85] explored the influence of domain wall chirality in the vortex regime with nanobars 200 nm wide and 20 nm thick. They too

found that the domain wall chirality affected the domain wall's propagation direction at a Y-shaped junction and explained their result in terms of the topology of the domain wall and the vertex. In their argument, however, they asserted that the chirality of the vortex domain wall is robust under Walker Breakdown whilst the vortex domain wall polarity is not, citing Tretiakov et al.'s work [94]. As such, they predicted that the vortex domain wall propagates through ASI in an entirely selective fashion, either in an arm-chair or zigzag fashion, dependent on whether a transverse or vortex domain wall is nucleated in the non-horizontal bar. In this section their assertion is considered in light of experimental data showing seemingly random walks of domain walls in the vortex regime of nanobar dimensions of both 173 nm × 1.5 µm × 36 nm and 181 nm × 2 µm × 36 nm. In light of micromagnetic simulations, it is suggested that these results arise because the path selected by a domain wall not only depends on its topology but also on its precise micromagnetic structure, and that its micromagnetic structure changes considerably during propagation.

Potential correlations between two sequential decisions made by a domain wall at a Y-shaped junction were investigated as detailed in Section 5.3. The number of incidences in which the domain wall chose the upper branch followed by the upper branch ($\Delta y = +2$), the upper branch followed by the lower branch ($\Delta y = 0$), the lower branch followed by the upper branch ($\Delta y = 0$) and the lower branch followed by the lower branch ($\Delta y = -2$) were counted. For 1.5 µm long nanobars, from 204 events, domain walls made the same decision twice 104 times ($\Delta y = +2$ or $\Delta y = -2$) and two different decisions 100 times ($\Delta y = 0$). This result is illustrated in Fig. 5.8 (a) and in Table 5.2. An exact binomial test performed on this data yielded a one-tailed p-value of 0.417. This result therefore suggests that, for nanobar dimensions 173 nm × 1.5 µm × 36 nm, domain walls do indeed exhibit a random walk. This result differs starkly from the p-value of 1.69×10^{-9} achieved in nanobars of dimension 100 nm × 1 µm × 18 nm and described in Section 5.4 which suggested a distinctly non-random walk situation.

For 2 µm long nanobars, from 85 events, domain walls made the same decision twice 50 times ($\Delta y = +2$ or $\Delta y = -2$) and two different decisions 35 times ($\Delta y = 0$). This result is illustrated in Fig. 5.8 (b) and in Table 5.2. An exact binomial test

$(\Delta x, \Delta y)$	**1.5 µm**	**2 µm**
$(2, +2)$ u-u	56	27
$(2, 0)$ u-d	49	17
$(2, 0)$ d-u	51	18
$(2, -2)$ d-d	48	23
$(2, \pm 2)$ u-u, d-d	104	50
$(2, 0)$ u-d, d-u	100	35
Total	204	85
$p - value$	*0.417*	*0.064*

Table 5.2: Summary of the two bar correlator results (see Section 5.3.1) in the vortex domain wall regime for bar lengths 1.5 µm and 2 µm. The p-values shown are for one-tailed exact binomial tests.

performed on this data yielded a one-tailed p-value of 0.064. Although this p-value is considerably lower than the value achieved for 1.5 µm bars, the null-hypothesis of a random walk was still accepted at a 5% significance level.

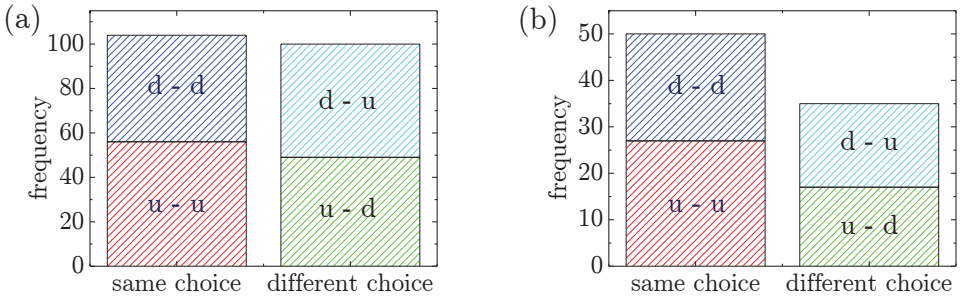

Figure 5.8: Graphical representation of two bar correlator data (see Section 5.3.1) in the vortex domain wall regime summarised in Table 5.2. Data is displayed in bar graphs (a) for 1.5 µm and (b) for 2 µm long nanobars. u-u, u-d, d-u and d-d correspond to $(\Delta x, \Delta y)$ of $(2, +2)$, $(2, 0)$, $(2, 0)$ and $(2, -2)$ respectively.

5.5.1 Discussion

In order to investigate the mechanism responsible for this random walk result, micromagnetic simulations of the propagation of vortex domain walls through a single ASI vertex with nanobars 150 nm wide and 36 nm thick were performed as described

in Section 5.2.3. An initial vortex domain wall structure was introduced to the left of the vertex and allowed to evolve in an external magnetic field. All four chirality polarity permutations were studied, the results of which are shown in Fig. 5.9. To improve clarity, the ends of the nanobars have been removed from view. Initial anticlockwise chirality domain walls of both up and down polarities resulted in the lower branch's reversal (Fig. 5.9 (a) & (b)) and initial clockwise chirality domain walls of both up and down polarities resulted in the upper branch's reversal (Fig. 5.9 (c) & (d)). These findings are consistent with a purely topological model of domain wall trajectory [85]. However, it was observed that the way in which the domain walls propagated through the vertex were different to those seen by Pushp & Phung et al. for all four chirality-polarity permutations.

The differences between the simulations shown here in Fig. 5.9 and those in Pushp & Phung et al.'s paper could arise for a number of reasons. Firstly, the geometry of their nanobars, both their dimensions and angle of opening of the Y-junction, are different to those studied here (theirs: 20 nm × 200 nm opening 30°, here: 36 nm × 150 nm opening 60°). Secondly, their driving magnetic field, 50 Oe, is appreciably lower than that used here, 250 Oe. The coercivities of the non-horizontal nanobars described here are approximately 4 times higher than those studied by Pushp & Phung et al. which is partly due to the difference in nanobar dimensions (the difference in thickness, t, and width, w, between the nanobars accounts for a factor of 2.4 since $coercivity \propto t/w$ [36]) and partly due to the difference in the angle of opening between the non-horizontal nanobars (which accounts for a factor $\cos(30°)/\cos(60°) \approx 1.7$)). And thirdly, their initial vortex domain wall micromagnetic structures are different from those here with their cores dramatically offset from the centres of the horizontal nanobars. However, despite all this, their simulations and those described here are topologically equivalent. As such, it is clear that the way in which a domain wall traverses a vertex does not exclusively depend on topology.

Micromagnetic simulations of the propagation of topologically equivalent clockwise chirality up polarity domain walls through a single ASI vertex were studied. Two different starting configurations were used which are termed *micromagnetic structure 1* (which is identical to the starting configuration used in Fig. 5.9 (d)) and *micromag-*

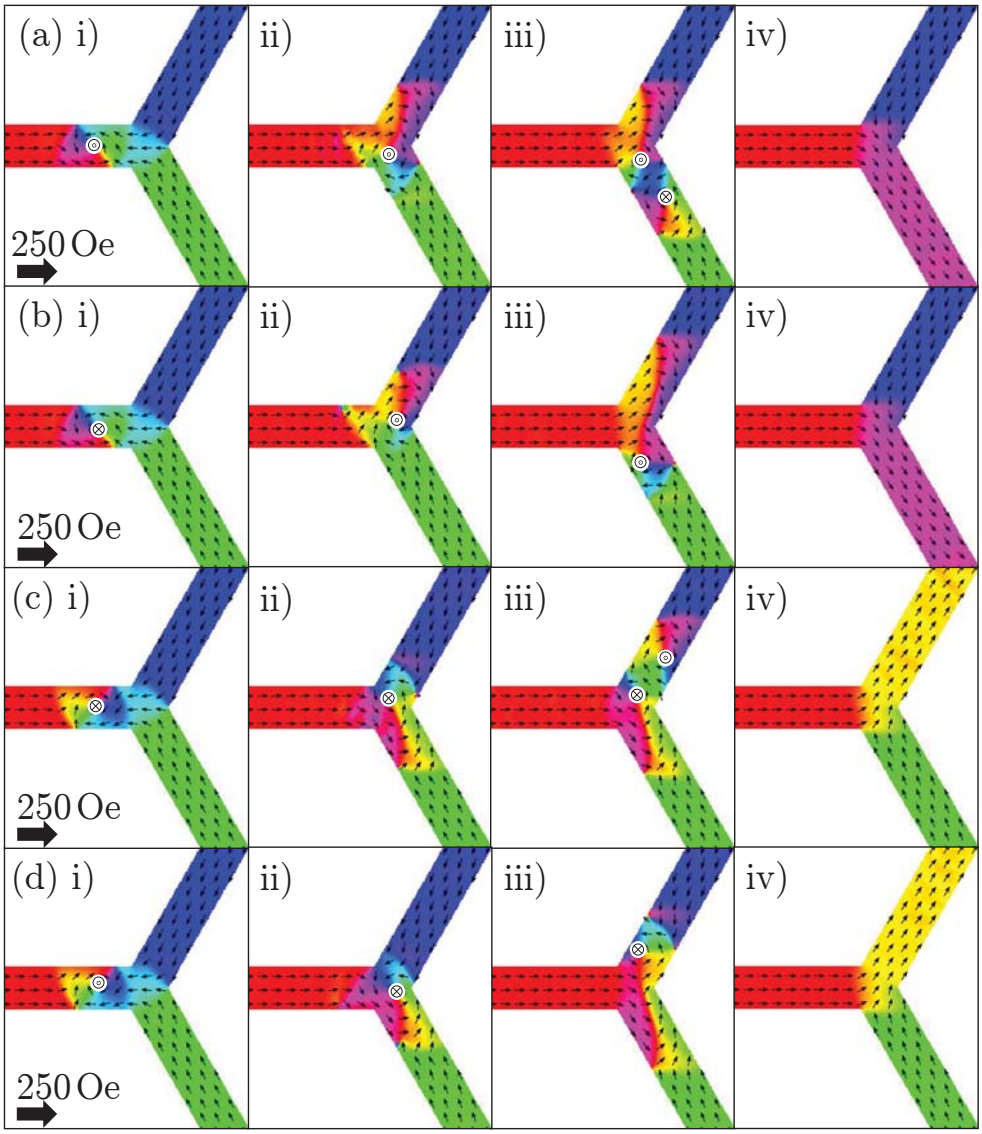

Figure 5.9: Micromagnetic simulations showing an initial vortex domain wall under the influence of a 250 Oe external field faced with two nominally equivalent paths. The four chirality-polarity combinations (a) anticlockwise-up, (b) anticlockwise-down, (c) clockwise- down and (d) clockwise-up are shown. i) shows the initial domain wall structure, ii) and iii) show the domain wall's interaction with the vertex and iv) shows the magnetic configuration after either the upper or lower bar has been reversed. Vortex polarities are identified by the black markers. To improve clarity, the ends of the nanobars have been removed from view.

netic structure 2 (whose vortex core is displaced 25 nm with respect to micromagnetic structure 1's). Fig. 5.10 (a) shows the propagation of micromagnetic structure 1 under

250 Oe (identical to Fig. 5.9 (d)) resulting in the reversal of the upper branch and Fig. 5.10 (b) shows the propagation of micromagnetic structure 2 under 250 Oe resulting in the reversal of the lower branch. From these simulations it is clear that two domain walls of identical chirality and polarity (and hence topology) but slightly different micromagnetic structure driven at the same external field can result in the switching of different branches. In addition it was seen that two identical domain walls, both micromagnetically and topologically, driven at different fields can also result in the switching of different branches. The propagation of micromagnetic structure 2 at 250 Oe, resulting in the reversal of the lower branch, is shown in Fig. 5.10 (b), and at 300 Oe, resulting in the reversal of the upper branch, is shown in Fig. 5.10 (c). These two findings clearly demonstrate that the domain wall trajectory not only depends on the domain wall's topology but also on its exact micromagnetic structure and the field at which it is driven.

In order to examine the vortex domain walls' structural changes during propagation in applied fields of different magnitudes, further micromagnetic simulations were performed. Here, the micromagnetic structure of an initial anticlockwise chirality up polarity domain wall was studied as it propagated through a 150 nm wide, 36 nm thick nanobar under the influence of external axial magnetic fields of magnitudes 100 Oe, 200 Oe, 300 Oe, 400 Oe and 500 Oe. At these fields the behaviour is governed by spin precessional frequency limitations and examples of complex micromagnetic structures that can be formed from the initial vortex domain wall structure are seen.

There are two important observations from this study. The first observation is that for all external field magnitudes studied, the exact micromagnetic structure of the domain wall was transformed as it propagated. In some cases this transformation was significant and the domain wall's topology was altered. An example of this is shown in Fig. 5.11 (a). The second observation is that the overall chirality of a vortex domain wall may change from anticlockwise to clockwise, an eventuality already observed by Lee et al. [90]. This type of behaviour was seen at an external magnetic field of 500 Oe and is shown in Fig. 5.11 (b). Here a complex micromagnetic state containing an anticlockwise domain wall transforms into a complex micromagnetic state containing a clockwise domain wall.

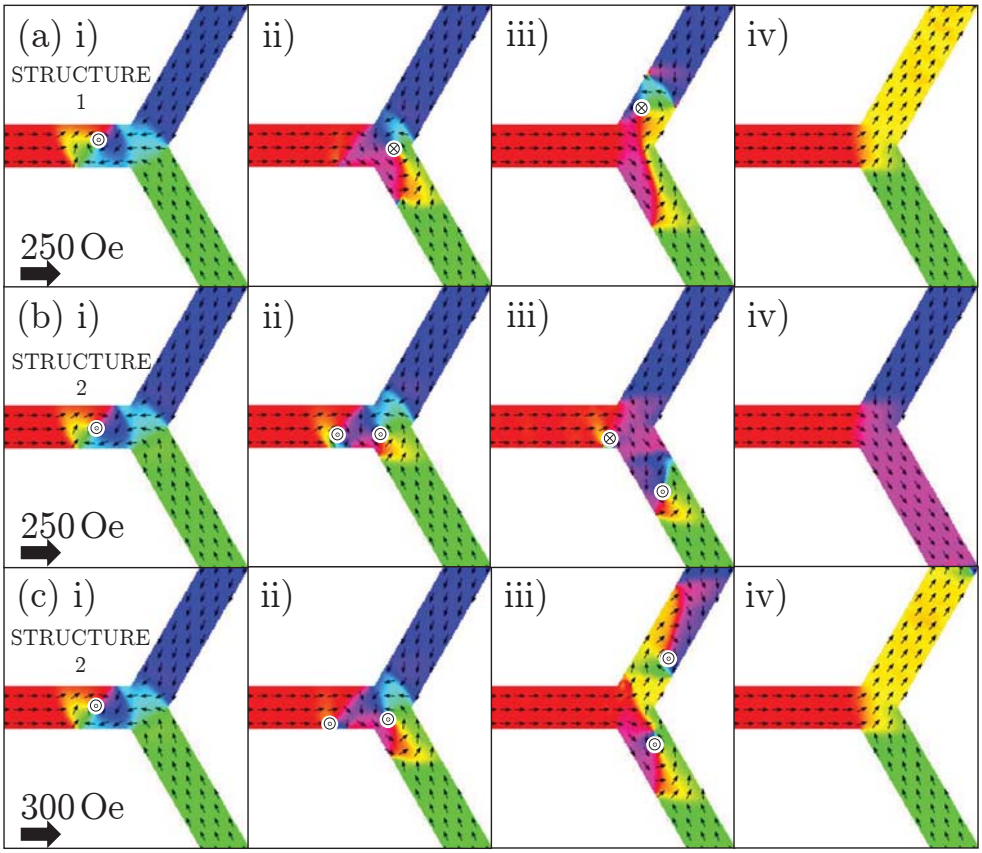

Figure 5.10: Micromagnetic simulations showing the motion of clockwise chirality up polarity vortex domain walls through an ASI vertex under a field in the positive x direction. (a) micromagnetic structure 1 driven at 250 Oe, (b) micromagnetic structure 2 driven at 250 Oe and (c) micromagnetic structure 2 driven at 300 Oe. Vortex polarities are identified by the black markers. Despite topologically equivalent starting configurations three different switching mechanisms are seen resulting in the reversal of the (a) upper, (b) lower and (c) upper branches respectively.

In order to assess the likelihood of the above events, it is necessary to consider the external fields at which domain walls propagate in ASI. The experimental data shows room temperature reversal occurring at external fields ≈ 100 Oe in magnitude. Since the Walker Breakdown critical fields decrease with increasing temperature [95] it is possible that, at 300 K, the data is recorded in an even more complex regime than that shown in Fig. 5.11 (a), in which domain wall micromagnetic structure and topology too are altered significantly.

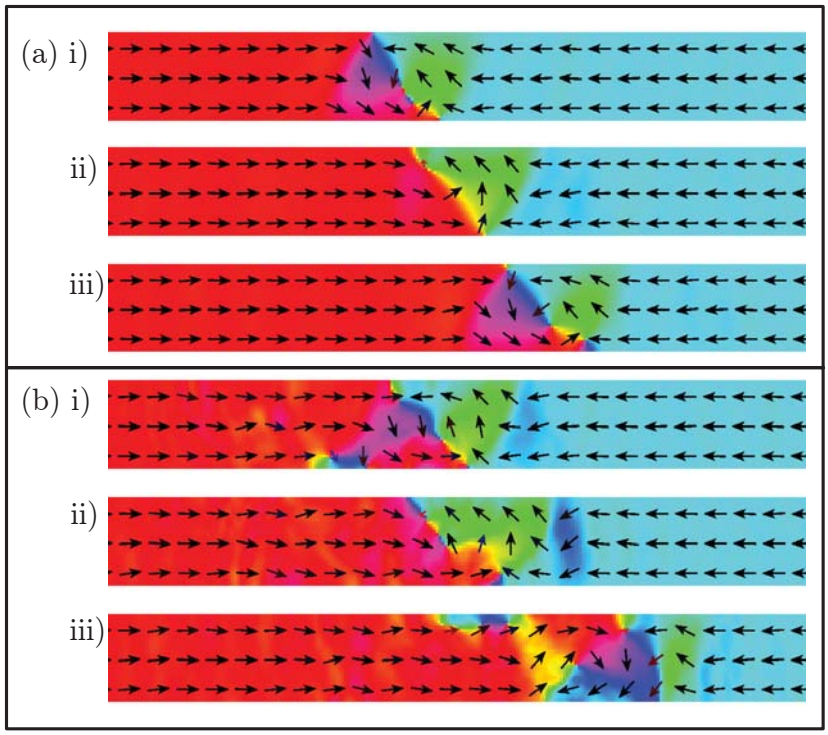

Figure 5.11: Micromagnetic simulations showing domain walls in a nanobar 150 nm wide and 36 nm thick undergoing propagation in external magnetic fields of (a) 100 Oe and (b) 500 Oe. In (a) complex micromagnetic states are seen which are sometimes more similar in appearance to transverse than vortex domain walls (e.g. state ii)). In (b) a complex micromagnetic structure involving an anticlockwise chirality domain wall in i) transforming into another complex micromagnetic structure involving a clockwise chirality domain wall in iii) is seen.

In light of these micromagnetic simulation observations presented above, the following explanation as to why selective behaviour is not seen in the data is offered. A domain wall of a certain micromagnetic structure and topology is presented to the first decision point. The diagonal branch reversed depends on the initial domain wall's exact structure and topology. The domain wall which propagates along the selected diagonal branch also has a complex micromagnetic structure which mutates over time. When a domain wall subsequently arrives at the second decision point it is in all likelihood structurally and perhaps topologically different to the domain wall

at the first decision point. Therefore either the same or a different diagonal branch is selected and no correlation between the two decisions is seen.

5.6 Summary

An investigation into the field-driven trajectories of transverse and vortex domain walls in ASI was performed. Scanning Transmission X-ray Microscopy data was presented suggesting that the domain walls followed non-random walks in the transverse domain wall regime and random walks in the vortex domain wall regime. The former result was attributed to some conservation of chiral information between decision points. The latter result was not fully explained by Pushp & Phung et al.'s model which is based purely on the topology of the domain walls and vertices. Further factors such as complex variations in domain wall micromagnetic structure during domain wall propagation were found to have an important influence on the path selection in these geometries. Understanding and controlling the full reversal of ASI is crucial in order to realise its full functionality and these results are an important step forward in this process.

CHAPTER 6 : CONTROLLING DOMAIN WALL CHIRALITY IN ARTIFICIAL SPIN ICE

As described in Chapter 5, domain wall chirality can play an important role in the field-driven domain wall mediated magnetic reversal of Artificial Spin Ice (ASI). In this chapter methods to control this domain wall chirality are explored.

Domain walls which mediate ASI's reversal may either be depinned from its edges in an order determined by the local quenched disorder or be controllably injected via large area *injection pads*. In the first section of this chapter, the possibility of using triangular injection pads in order to controllably inject transverse domain walls of known chirality is explored. The dependence of the injected domain wall's chirality on the dimensions of the triangular injection pad nanobar system is also investigated. In addition, a study into the external fields required for nucleation and injection of domain walls from pads of different sizes is presented. Both micromagnetic simulations and experimental results contribute to this discussion.

In the second section of this chapter a study into the control of vortex domain walls is presented. Ellipsoidal holes in nanobars are shown to pin vortex domain walls, and, depending on their size, position and orientation, are shown to switch, set, randomise or filter the domain wall's chirality. Although this study is at this stage based purely on micromagnetic simulation at absolute zero, ideas for experimental verification of these theories are included.

6.1 Triangular injection pads to inject transverse domain walls of known chirality

An *injection pad* is a structure of relatively large area fabricated onto the end of a nanobar [96, 97]. The injection pad has a lower coercivity than its neighbouring nanobar and hence undergoes magnetic reversal at lower external magnetic fields. The reversal of the injection pad introduces a domain wall at the junction between the injection pad and the nanobar. This domain wall is subsequently depinned at higher external magnetic fields and propagates along the nanobar, mediating its reversal. As such, the pad acts as a nucleation source of domain walls and reduces the switching field of the adjacent nanobar. Injection pads can be fabricated onto the edge of ASI arrays in order to control the positions at which magnetic reversal and hence cascades start, and to reduce the external magnetic field required to start reversal. Fig. 6.1 shows a charge configuration schematic for the left-hand edge of an ASI array after saturation in the left-hand direction for two different situations (a) without and (b) with an injection pad. According to the simple charge model described in Section 2.10.3.1, nanobar reversal starts at a field $H_c = 2 \times H_{quenched}$ without an injection pad but only $H_c = H_{quenched}$ with an injection pad ($H_{quenched}$ varies from nanobar to nanobar and describes the inherent quenched disorder in the array).

As demonstrated in Chapter 5, chirality plays an important role in the propagation paths of domain walls in ASI. As such, control of domain wall chirality is a necessary step towards the complete understanding of ASI's rich reversal behaviour and the subsequent realisation of its full functionality. McGrouther et al. [98] have already demonstrated the injection of vortex domain walls of known chirality via off-centre elliptical injection pads. Although the controllable injection of transverse domain walls of known chirality has already been achieved using hooks and complex orthogonal fields [92], the controllable injection of transverse domain walls using only a simple uniaxial field has yet to be demonstrated. In this section the possibility of using triangular injection pads of certain sizes and shapes in order to control the chirality of the injected transverse domain wall is explored. Although some images of injection from triangular pads have been acquired via STXM and PEEM, most of this work is

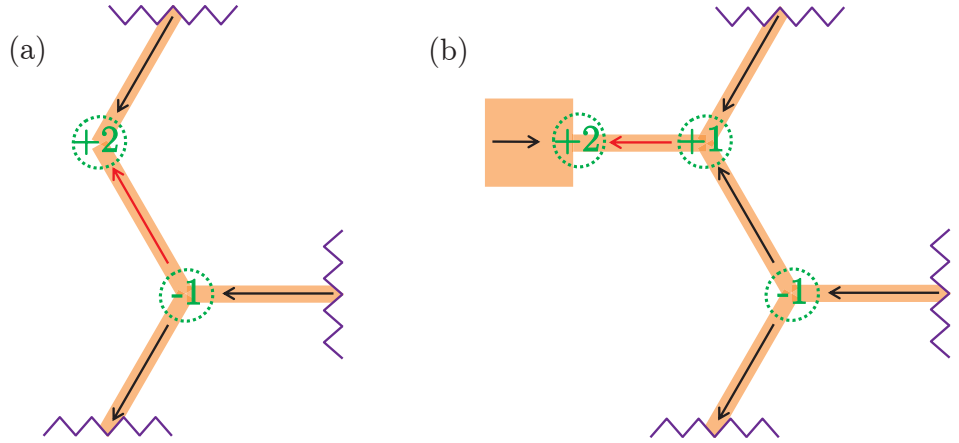

Figure 6.1: Injection pad schematic showing the charge configuration after saturation in the left-hand direction (a) without and (b) with an injection pad at the left-hand edge of an ASI array. According to the simple charge model for nanobar coercivities, nanobar reversal of the nanobars shown with red arrows starts at a field $H_c = 2 \times H_{quenched}$ in (a) but only $H_c = H_{quenched}$ in (b).

based on micromagnetic simulation performed with the OOMMF software [18].

The simplest geometry for injection involves an injection pad for example of square or circular shape centred symmetrically on the nanobar's long axis. In the square injection pad's case, a C-state, S-state or vortex state is supported at remanence depending on the exact dimensions of the system [99]. If the square injection pad-nanobar system is perfectly smooth, there are two possible degenerate magnetisation configurations after saturation along the nanobar's long axis. Fig. 6.2 shows the simulated magnetisation behaviour for an 18 nm thick system with square injection pad of lateral dimensions 1 µm × 1 µm and nanobar of width 100 nm. Here one of two different degenerate S-states is supported at remanence with the switching and hence chirality of the domain wall injected dependent on which of these S-states is supported initially. This means that there is a 50% probability of injecting an up or a down chirality domain wall. In contrast, however, a perfectly smooth triangular injection pad supports a unique remanent groundstate after saturation along the nanobar's long axis and as such switches in an entirely predictable fashion. Therefore

the orientation of this triangular injection pad alone, upright or upside-down, should determine the chirality of the injected domain wall.

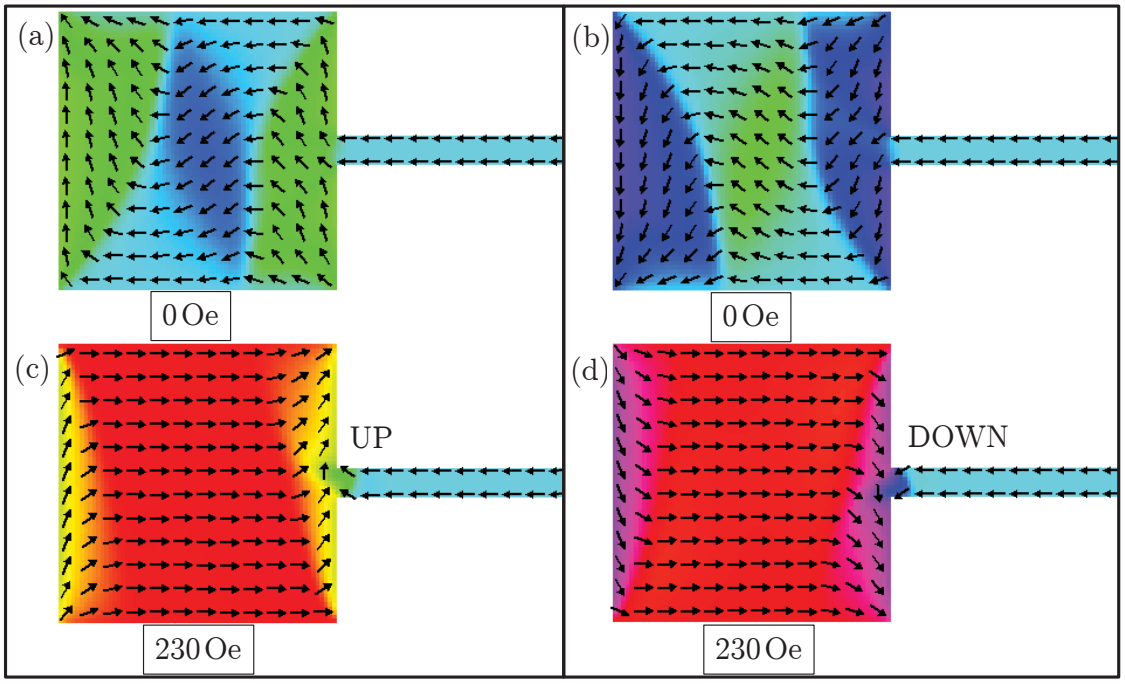

Figure 6.2: Micromagnetic simulation of the injection of a domain wall by a 1 µm × 1 µm × 18 nm square injection pad into a 100 nm wide nanobar. (a) & (b) show the two different degenerate remanent S-states following saturation in the negative x direction. (c) & (d) show the magnetisation when states shown in (a) & (b) respectively are subjected to an externally applied magnetic field of 230 Oe in the positive x direction. (c) & (d) show up and down chirality transverse domain walls respectively pinned at the pad just before injection.

The groundstates of isolated triangles of different dimensions have been explored by Kolstov et al. [100]. Triangles of very small dimensions support a Y state in which neighbouring magnetic moments are all approximately aligned with respect to each other. Conversely in larger triangles a buckle state is supported in which neighbouring magnetic moments are rotated slightly with respect to each other such that the net magnetisation is bent about one of the triangle's axes. In still larger triangles, a vortex state is stabilised, in which the magnetisation swirls around a vortex core. The chirality of the domain wall injected from a triangular injection pad should depend on its initial remanent magnetic state after saturation and hence on its

dimensions. In order to investigate this hypothesis, micromagnetic simulations were performed for triangular injection pads of different dimensions, the details of which are given below.

6.1.1 Method

Micromagnetic simulations were performed on permalloy triangular injection pad-nanobar systems with the OOMMF software [18]. The simulations were performed at absolute zero temperature. The magnetocrystalline anisotropy of $Ni_{81}Fe_{19}$ was assumed to be zero, the exchange constant was taken to be $1.3 \times 10^{-11}\,\mathrm{Jm}^{-1}$, and the saturation magnetisation was taken to be $800\,\mathrm{kAm}^{-1}$. The triangular injection pads were all equilateral and supported a nanobar at $0.45 \times$ (perpendicular height) from their base (see Fig. 6.3). The injection pads and nanobars always shared the same thickness. Mesh sizes specified in Table 6.1 were used. A convergence criterion of $d\phi/dt < 0.1$ was used. Since the behaviour of magnetisation versus external field was of interest, a Gilbert damping parameter of $\alpha = 0.5$ was used. A colour map was used to achieve an entirely saturated state in the negative x direction. An external magnetic field was then applied stepwise in 10 Oe increments in the positive x direction until a domain wall was injected into the nanobar. The chirality of the domain wall injected into the nanobar was visually identified as it was depinned from the triangular injection pad's mouth.

	Section 6.1.2.1	**Section 6.1.2.2 & 6.1.2.4**	**Section 6.1.2.3**
x	1.0 nm	5.0 nm	2.5 nm
y	1.0 nm	5.0 nm	2.5 nm
z	5.0 nm	18.0 nm	5.0 nm

Table 6.1: The mesh sizes used for micromagnetic simulations in different sections of this chapter.

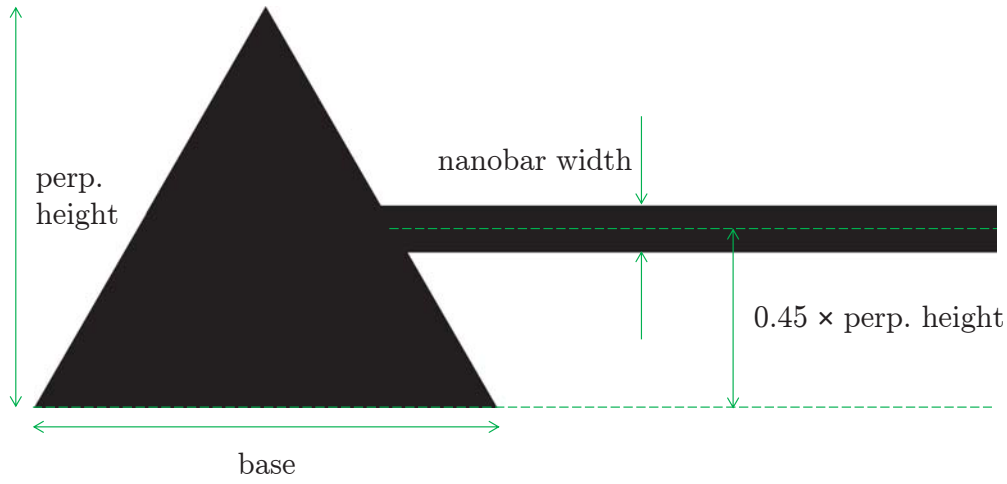

Figure 6.3: Geometry of triangular injection pad system.

6.1.2 Micromagnetic simulation results

6.1.2.1 Y state

A system of triangular injection pad base size 100 nm, nanobar width 10 nm and thickness 5 nm was studied. A Y state was supported at remanence after saturation in a direction along the nanobar's long axis and the chirality of the domain wall subsequently injected depended on the orientation of the triangular injection pad; the upright triangular injection pad injected a down chirality domain wall and the upside-down triangular injection pad injected an up chirality domain wall (see Fig. 6.4).

6.1.2.2 Buckle state

A system of triangular injection pad base size 600 nm, nanobar width 80 nm and thickness 18 nm was studied. For these dimensions a buckle state was favoured at remanence after saturation in a direction along the nanobar's long axis. Again, the chirality of the domain wall subsequently injected depended on the orientation of the injection pad; an upright triangular injection pad injected a down chirality domain wall (see Fig. 6.5 (c)) whereas an upside-down triangular injection pad injected an

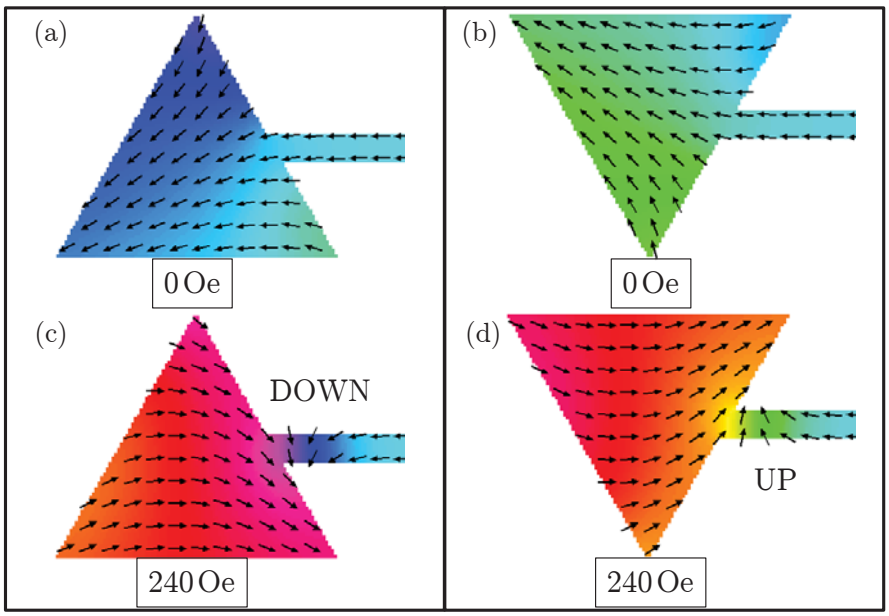

Figure 6.4: Micromagnetic simulations showing the injection of domain walls in the Y state regime, here 100 nm triangular injection pad base, 10 nm wide nanobar, 5 nm thick system. (a) & (b) show the remanent states after saturation in the negative x direction along the nanobar's long axis for upright and upside-down triangular injection pads respectively. (c) & (d) show the subsequent injection of down and up chiralities respectively on application of a 240 Oe field in the positive x direction.

up chirality domain wall.

6.1.2.3 Y-buckle state

A system of triangular injection pad base size 250 nm, nanobar width 50 nm and thickness 5 nm was studied. An interesting remanent state was seen after saturation along the nanobar's long axis. This state had both Y state and buckle state characteristics and as such was termed a *Y-buckle* state. This state showed both buckling of magnetisation near the base of the triangle as well as a large stray field due to the absence of buckling at the peak (see Fig. 6.5 (b)). Interestingly, this Y-buckle state switched neither like the pure Y nor like the pure buckle state and as such injected domain walls with opposite chiralities to those seen for both the pure buckle and the pure Y states i.e. an upright triangular injection pad injected an up chirality domain

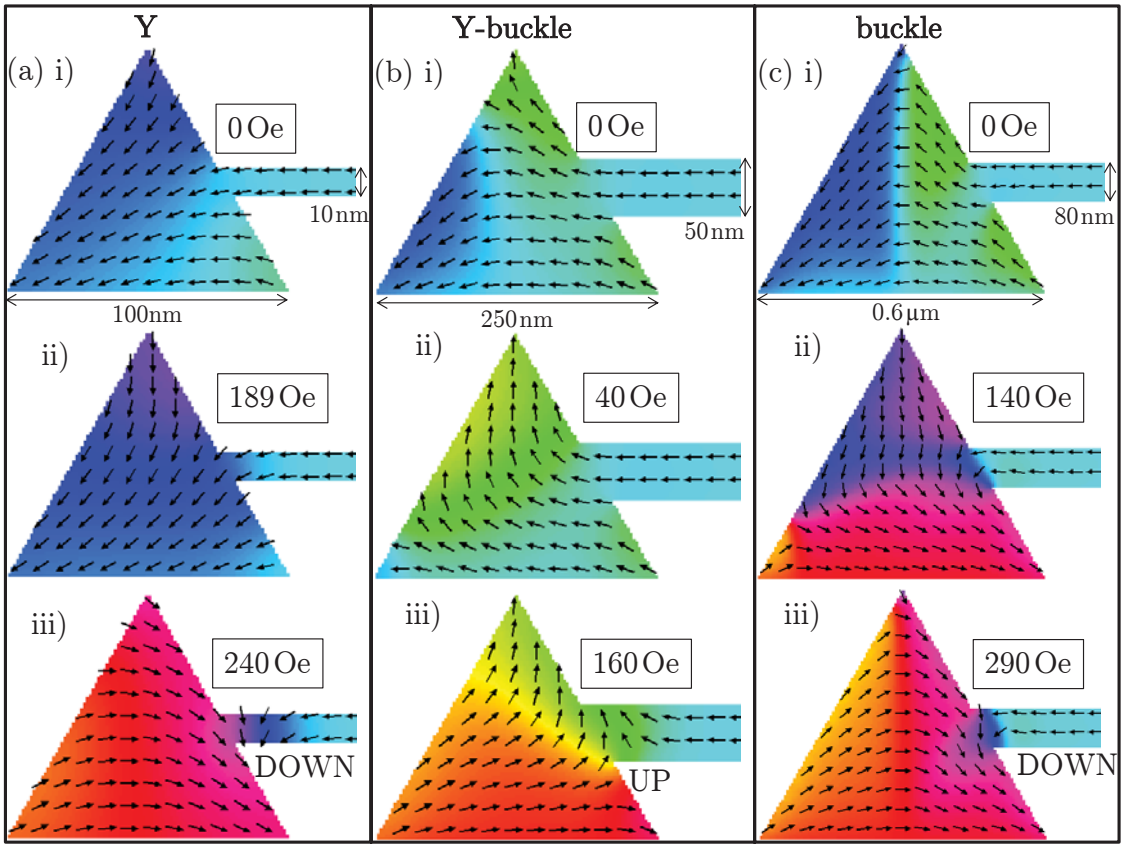

Figure 6.5: Comparison of domain wall injection from upright triangular injection pads in the Y, Y-buckle and buckle regimes after saturation in the negative x direction and a (labelled) smaller field in the positive x direction. (a) when a Y state is stabilised at remanence, a down chirality domain wall is injected (here, 100 nm triangular base, 10 nm wide nanobar, 5 nm thick system) (b) when a Y-buckle state is formed at remanence, an up chirality domain wall is injected (here, 250 nm triangular base, 50 nm wide nanobar, 5 nm thick system) and (c) when a buckle state is formed at remanence, a down chirality domain wall is injected (here, 600 nm triangular base, 80 nm wide nanobar, 18 nm thick system). The first row, (i), shows the remanent state after saturation in the left hand direction, the second row, (ii), the switching path and the third row, (iii), the domain wall pinned at the pad just before injection of chirality (a) down, (b) up, (c) down.

wall and an upside-down triangular injection pad injected a down chirality domain wall.

6.1.2.4 Depinning fields in buckle regime

Since the type and degree of Walker Breakdown that a domain wall experiences depends on the field at which it propagates at and hence the field at which it is injected, the external fields at which triangular injection pads reversed and subsequently injected domain walls into nanobars were investigated. Injection pad and nanobar systems in the buckle regime with nanobar dimensions close to those used in experiments in Section 5.4 were investigated, the results of which are shown in Fig. 6.6.

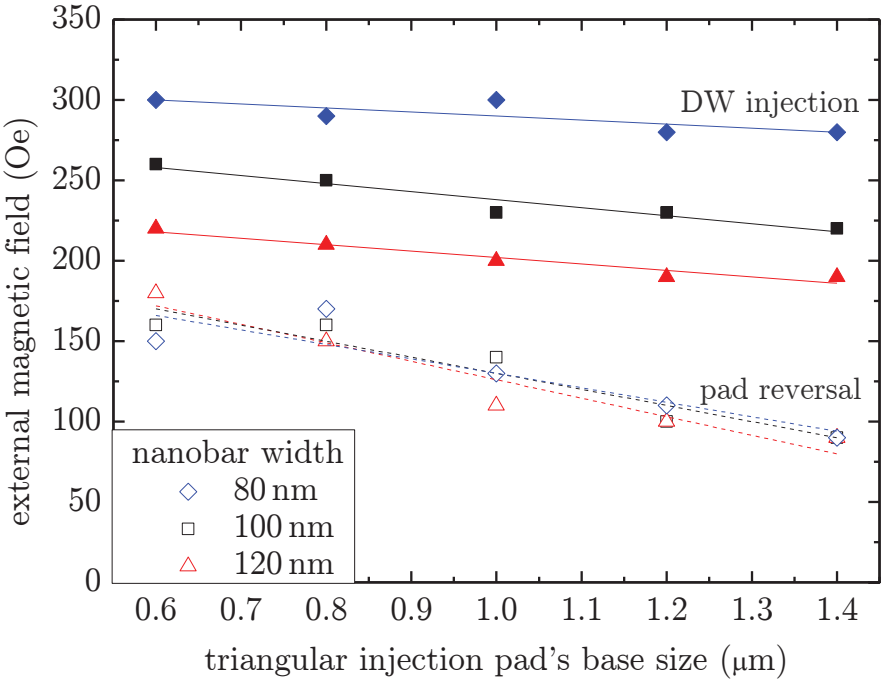

Figure 6.6: The dimension dependence of the triangular injection pad's coercivity (open symbols) and domain wall depinning/injection field (closed symbols) in the buckle regime. The diamond, square and triangle symbols represent nanobar widths of 80 nm, 100 nm and 120 nm respectively. All the structures investigated were 18 nm thick and supported buckle states at remanence. The lines are guides to the eye.

There were four main observations from this study: 1. the field at which the injection pad reverses tends to decrease with increasing injection pad size, 2. the field at which the injection pad reverses depends weakly on the width of the nanobar

(consistent with the findings of Bogart et al. [26]), 3. the field at which the domain wall is injected decreases with increasing nanobar width (also consistent with Bogart et al. [26]) and 4. the field at which the domain wall is injected has weak dependence on the size of the injection pad.

From these results it can be concluded that, if minimising the field of domain wall injection is important in the buckle state regime, a wide nanobar and a large triangular injection pad base should be used. However, if minimising device size in the buckle state regime is important, a smaller injection pad may be used which will have only an incrementally higher injection field.

6.1.3 Experimental results

Preliminary experiments to verify this theory of controlled chiral transverse domain wall injection were made via both Scanning Transmission X-ray Microscopy and Photo Electron Emission Spectroscopy. The results of these studies are presented below.

6.1.3.1 STXM

Fig. 6.7 shows Scanning Transmission X-ray Microscopy images of the successful injection of a domain wall from an upside-down triangular injection pad of base size 1 μm, thickness 19.3 nm into a 100 nm wide and 0.5 μm long nanobar joined to an ASI vertex. The images were taken at Beamline 11.0.2 Advanced Light Source, Berkeley. As discussed in Section 5.4, an ASI vertex in the transverse domain wall regime should act as a chirality filter and, so long as the domain wall has not undergone Walker Breakdown before the vertex, should reveal the chirality of the injected domain wall; an up chirality domain wall should result in the reversal of the upper branch and a down chirality domain wall should result in the reversal of the lower branch.

The STXM images in Fig. 6.7 show the evolution of the magnetic state supported by an upside-down triangular injection pad in increasing external field preceding domain wall injection. It was expected that a buckle state would be supported for these dimensions. Fig. 6.8 shows the simulated STXM images during reversal of an upside-down injection pad system that supports a buckle state at remanence. The

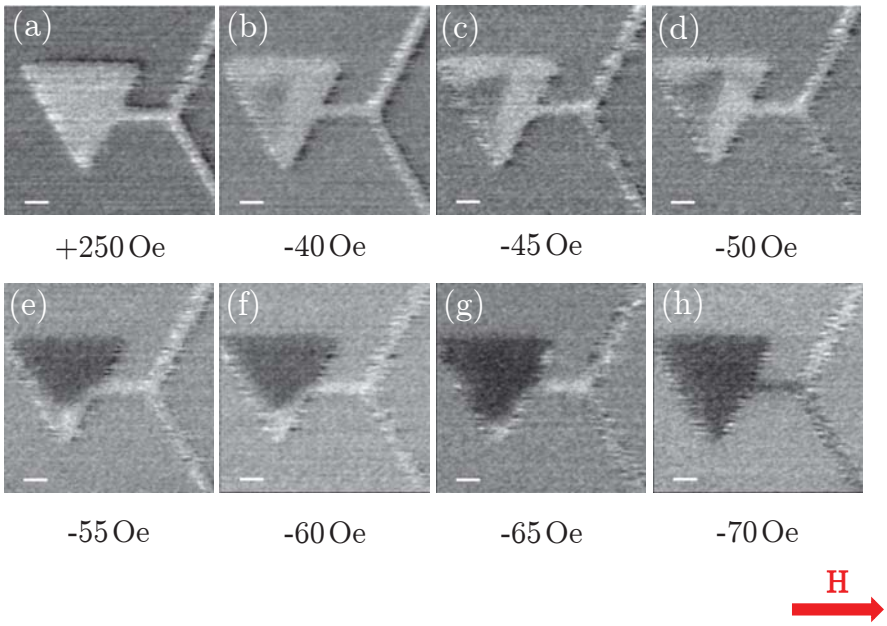

Figure 6.7: Scanning Transmission X-ray Microscopy images showing the injection of a domain wall from an upside-down triangular injection pad of base size 1 µm, thickness 19.3 nm into a 100 nm wide and 0.5 µm long nanobar joined to an ASI vertex. White and black contrast indicate magnetisation in the positive and negative x directions respectively. The white scale bar corresponds to 200 nm. (a) shows the system saturated in the positive x direction, (b) - (f) show the step-wise reversal of the injection pad, (g) shows the system with the domain wall pinned at the mouth of the injection pad and (h) the subsequent injection of a domain wall into the nanobar at an external magnetic field of −70 Oe followed by the reversal of the lower branch.

great similarity between the experimental and simulated STXM images, especially Fig. 6.7 (d) and Fig. 6.8 (b), suggests that the experimental system was indeed in the buckle regime. As such, it was expected that an up chirality domain wall would be injected from the triangular injection pad, resulting in the reversal of the upper branch. However, it is clear from Fig. 6.7 (h) that, in this instance, the lower branch is reversed instead.

In order to better understand this result, multiple sequential injections from the same triangular injection pad under the same field sequences were studied. Both the orientation of the triangle and the subsequent non-horizontal bar reversed were noted. It was observed that the domain walls injected from a specific injection pad

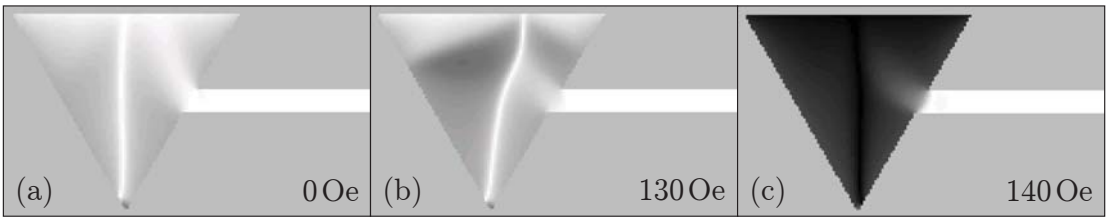

Figure 6.8: Micromagnetic simulations showing expected STXM contrast during the magnetic reversal of an upside-down triangular injection pad base 1 µm, 100 nm wide nanobar and 18 nm thick system at external fields (a) 0 Oe, (b) 130 Oe and (c) 140 Oe in the positive x direction.

did not always take the same branch at the ASI vertex. In addition, when results were combined from twelve nominally identical triangular injection pads and summarised in Table 6.2, it appeared that there was no correlation between the orientation of the triangular injection pad and the path the domain wall took; a one-tailed exact binomial test (described in Section 5.3.1) yielded a p-value of 0.450.

Orientation and direction	**Frequency**
upright triangle - up	14
upright triangle - down	9
upside-down triangle - up	21
upside-down triangle - down	18
same orientation and direction	32
different orientation and direction	30
Total	62
$p - value$	*0.450*

Table 6.2: Summary of experimental STXM triangular injection pad results: the paths taken by domain walls from twelve nominally identical triangular injection pads of both upright and upside-down orientations. The corresponding one-tailed exact binomial test p-value is also shown.

Possible explanations for and sources of this apparently non-selective behaviour are summarised in Table 6.3. Regarding the behaviour of the triangular injection pads it seems unlikely that a variation in groundstate or switching mechanism could occur given that the dimensions of the injection pad system fall well within the buckle

regime (see Fig. 6.6) and the high magnification STXM images show buckle behaviour (see Fig. 6.7 and Fig. 6.8). It seems more likely that fabrication imperfections at the mouth of the pad and/or thermal effects affected the depinning and hence chirality of the domain wall.

Possible explanation	**Possible source**
Triangular injection pads not 100% selective.	Variation in injection pad groundstates, switching mechanisms or depinning due to thermal effects or fabrication imperfections.
DW sometimes changes chirality between injection pad and vertex.	Walker Breakdown affects some DWs and not others during propagation through 0.5 µm long nanobar.
ASI vertex not 100% accurate as chirality filter.	Stray field of triangle, fabrication imperfections or thermal effects affect vertex magnetisation.

Table 6.3: Possible explanations for the apparently non-selective behaviour seen in the triangular injection pad data summarised in Table 6.2.

It is also possible that some of the domain walls suffered Walker Breakdown during propagation along the 0.5 µm nanobar between the injection pad and the ASI vertex (see e.g. [92]). However data presented in Section 5.4 for 1 µm long nanobars of the same width and thickness in which a greater loss of chiral fidelity would be expected showed 72.5% selectivity. As such, it seems unlikely that Walker Breakdown is exclusively responsible for this non-selective 52 : 48 result seen here.

Regarding the reliability of ASI vertices as chirality filters, it is possible that in some cases, due to fabrication imperfections and thermal effects, the filter did not work properly. However in light of the data shown in Section 5.4 it seems unlikely that poor-filtering of domain wall chirality at an ASI vertex could be fully responsible for the non-selectivity seen here. The influence of the triangular injection pad's stray field on the filtering properties of the ASI vertex is, at this stage, unclear. However it is thought that if all the injection pads support the same states as each other their stray field should boast selectivity and not destroy it.

The fact that two different domain walls from the same injection pad took different trajectories indicates that something with an element of randomness e.g. thermal

effects or Walker Breakdown does indeed affect the propagation path. In light of this and the discussion above it seems likely that there is more than one reason why the data shown in Table 6.8 shows non-selectivity. Further investigations with a PEEM imaging technique are described below and ideas for future work on the behaviour of triangular injections pads are provided in Section 6.3.1.

6.1.3.2 PEEM

Photo Electron Emission Microscopy (PEEM) images taken at Beamline I06, Diamond Light Source, Oxfordshire yielded similarly inconclusive results. Fig. 6.9 shows PEEM images of the early stages of ASI's magnetic reversal. The images were taken at remanence after currents of (a) −4 A, (b) 2.2 A, (c) 2.3 A and (d) 2.4 A were applied to an electromagnet situated below the sample providing in-plane fields of approximately +130 Oe, −71.5 Oe, −75.0 Oe and −78.0 Oe at the sample space respectively (estimated by comparison with the STXM data and by assuming that the field scaled linearly with current). Three upside-down triangles of base size 1 µm and thickness 18 nm were fabricated onto the left hand side of the array. The top and bottom triangular injection pads were both 950 nm away from the vertex whereas the middle injection pad was fabricated further away at a distance 1.4 µm. In these images it is clear that the two nominally identical injection pads at the top and the bottom have injected domain walls which have resulted in different propagation paths. It remains unclear as to whether this is due to (a) the two nominally identical triangular injection pads injecting domain walls of different chiralities, (b) different degrees of Walker Breakdown in the two nominally identical systems or (c) the ASI vertex not working as a perfect chirality filter. The reader is referred to Table 6.3 and the discussion surrounding it for a detailed analysis of possible sources of non-selectivity.

In order to identify the exact source of the non-selective transverse domain wall injection behaviour in both this PEEM data and the STXM data, further experiments must be performed such as those described in the future work Section 6.3.1. Meanwhile in the next section, the possibility of using ellipsoidal holes to control and readout vortex domain wall chirality is explored.

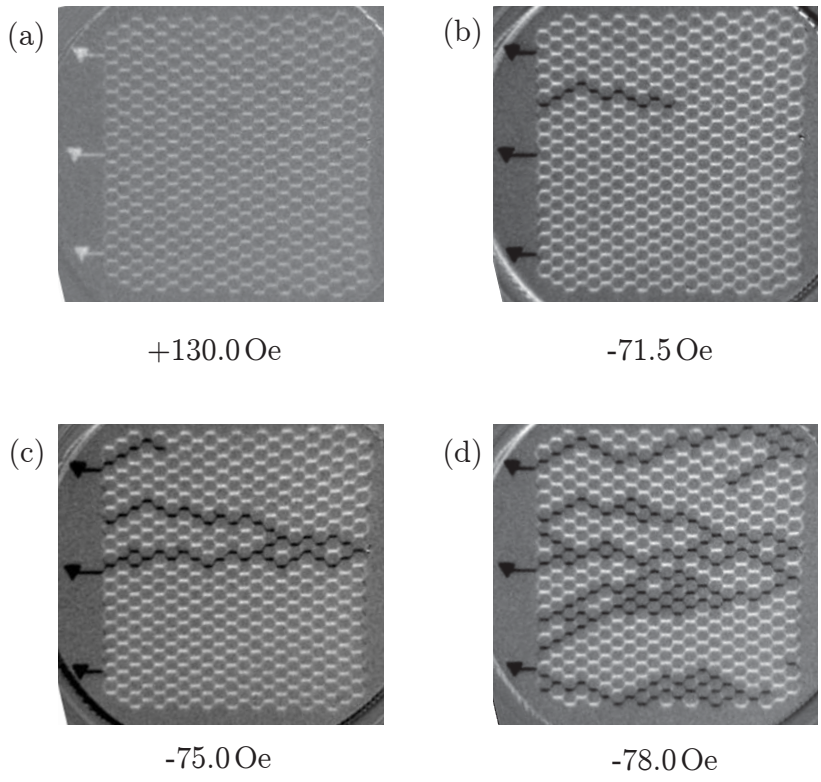

Figure 6.9: PEEM images showing the early stages of magnetic reversal of a 18 nm thick ASI array consisting of 0.5 µm long, 150 nm wide bars after saturation in the positive x direction. White and black contrast indicate magnetisation in the positive and negative x directions respectively. The images were taken at remanence after a current of (a) −4 A, (b) 2.2 A, (c) 2.3 A and (d) 2.4 A was applied to an electromagnet situated below the sample providing in-plane fields of approximately +13.00 mT, −7.15 mT, −7.50 mT and −7.80mT at the sample space respectively. The three injection pads fabricated on the left hand side of the array have all reversed by (b) and subsequently inject domain walls into the lattice at low external magnetic fields shown in (c) & (d).

6.2 Ellipsoidal holes to control and readout vortex domain wall chirality

As detailed in Section 5.5, domain wall chirality plays some role in the magnetic reversal of ASI in the vortex domain wall regime. In order to gain better understanding of and control over the magnetic reversal of ASI, a method for both control and readout of vortex domain wall chirality was developed. In this section, micromagnetic simulations are presented that show that field-driven vortex domain walls propagating in permalloy nanobars can be pinned in front of and subsequently pinned over (as a core-less *quasi-vortex domain wall* or two transverse domain walls) ellipsoidal holes. It is demonstrated that a small ellipsoidal hole, if centred about the nanobar's long axis, can act to change the chirality of the vortex domain wall, and if placed off-centre, can either act as a chirality filter or act as a means to set the chirality of the domain wall. In addition it is demonstrated that a large ellipsoidal hole, if centred about the nanobar's long axis, can act to randomise the chirality of the vortex domain wall. Furthermore it is shown that ellipsoidal holes rotated about their centre point act as chirality filters because quasi-vortex domain walls of opposite chiralities are depinned from them at different external fields.

Asymmetric notch pinning potentials may also be used to trap vortex domain walls for readout or chirality filtering [24]. Ellipsoidal holes, however, have greater functionality since they can not only be used for readout of vortex domain wall chirality and chirality filtering, but also can be used to change, set or randomise the chirality of the vortex domain wall subsequently depinned. As such, ellipsoidal holes promise to provide the necessary tools required to gain a better understanding of the role of domain wall chirality in the propagation paths of vortex domain walls in ASI. The exact details of the micromagnetic investigation into the ellipsoidal holes' functionality are given below.

6.2.1 Method

Micromagnetic simulations were performed on permalloy nanobars 100 nm wide, 1.12 µm long and 36 nm thick. A mesh size of [2.5 nm, 2.5 nm, 18 nm] was used. The simulations were performed at absolute zero temperature. The magnetocrystalline anisotropy of $Ni_{81}Fe_{19}$ was assumed to be zero and the exchange constant and saturation magnetisation were set to 1.3×10^{-11} Jm^{-1} and 800 kAm^{-1} respectively. A convergence criterion of $d\phi/dt < 0.1$ was used. Since the behaviour of magnetisation versus external field was of interest, a Gilbert damping parameter of $\alpha = 0.5$ was used. An ellipsoidal hole of constant 36 nm thickness was made in the nanobar. This had lateral dimensions X and Y. When X and Y were equal the hole was cylindrical. The ellipsoidal hole was made in the centre of the bar unless otherwise specified. If the ellipsoidal hole was rotated such that its semi-major and semi-minor axes were no longer parallel or perpendicular to the bar, the rotation was specified. A left-handed vortex head-to-head domain wall (i.e. clockwise chirality up polarity or anticlockwise chirality down polarity) was introduced via a colour map to the left of the ellipsoidal hole and the magnetic field was increased stepwise for 10 Oe field steps in the right hand direction.

6.2.2 Micromagnetic simulation results

6.2.2.1 Centred cylindrical holes

Micromagnetic simulations of vortex domain walls incident on centred cylindrical holes of diameters 10 nm to 90 nm were performed. The results of this study are summarised in Table 6.4 from which it is clear that there were four different types of behaviour seen.

For a cylindrical hole of diameter 10 nm, the domain wall was not pinned before the hole. Instead it was pinned over the hole as a quasi-vortex domain wall without changing chirality.

For a cylindrical hole of diameter 20 nm, the domain wall was pinned before the hole at low field. At higher field it subsequently depinned and propagated past the

Hole diameter (nm)	Behaviour
10	pinned as quasi-vortex of same chirality
20	not pinned over hole
30	pinned as quasi-vortex of opposite chirality
40	pinned as quasi-vortex of opposite chirality
50	pinned as quasi-vortex of opposite chirality
60	pinned as quasi-vortex of opposite chirality
70	pinned as two transverse DWs
80	pinned as two transverse DWs
90	pinned as two transverse DWs

Table 6.4: Summary of domain wall pinned behaviour over centred cylindrical holes of different diameters in nanobars 100 nm wide and 36 nm thick.

obstruction without being pinned over the cylindrical hole.

For slightly larger cylindrical holes (diameters 30 nm to 60 nm) the vortex domain wall was pinned just in front of the hole at low external magnetic fields with its core slightly offset from the centre of the nanobar in a direction dependent on its chirality (see Fig. 6.10 (a) & (f)). As the external magnetic field was increased, the vortex domain wall's core moved further downwards (Fig. 6.10 (b)) or upwards (Fig. 6.10 (g)), minimising Zeeman energy. At still larger external magnetic fields, the core of the domain wall moved very close to the edge of the nanobar. The vortex core was subsequently expelled from the nanobar enabling part of the domain wall to propagate past one side of the hole. The side of the hole which was affected was the side in which the vortex core had migrated towards. The domain wall was then pinned over the hole as a quasi-vortex domain wall. Since the part of the vortex domain wall that propagated past the obstruction first was initially the trailing part, this quasi-vortex domain wall pinned over the hole had a different chirality to the initial domain wall chirality (see Fig. 6.10 (c) & (h)). The quasi-vortex domain wall was subsequently depinned from the cylindrical hole at still higher external magnetic field. Despite the absence of a converged-state showing the chirality of the depinned domain wall, by looking at non-converged states (see Fig. 6.11) it was thought that the chirality of the domain wall depinned from the hole was the same as the chirality of the quasi-vortex domain wall pinned over the hole. Thus it appears that cylindrical holes of diameter

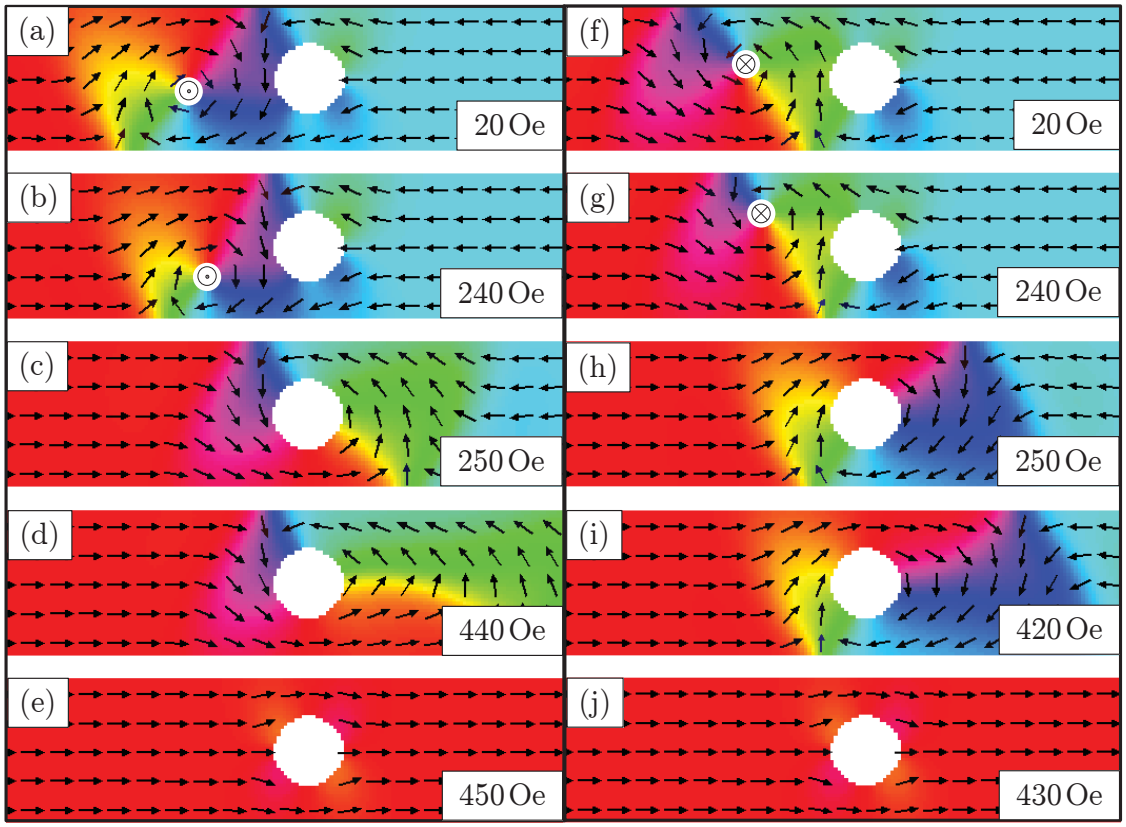

Figure 6.10: Cylindrical hole as a domain wall pinning site and chirality changer. A 50 nm diameter cylindrical hole in a 100 nm wide, 36nm thick nanobar with (a) - (e) a clockwise chirality up polarity and (f) - (j) an anticlockwise chirality down polarity vortex domain wall incident under the influence of an external magnetic field in the positive x direction. At low fields, (a) & (f), the domain wall is pinned before the hole. With increasing field, the vortex core moves downwards, (b), or upwards, (g), until the core is expelled and the trailing edge of the domain wall gets pushed through the narrow side of the hole, forming an anticlockwise, (c), and clockwise, (h), quasi-vortex domain wall respectively. At even higher fields the region aligned with the magnetic field grows, (d) & (i), until eventually the domain wall depins mediating magnetic reversal of the rest of the bar, shown in (e) & (j).

30 nm to 60 nm act to change the chirality of the incoming vortex domain wall.

For yet larger cylindrical holes (diameters 70 nm to 90 nm), the vortex domain wall was again pinned in front of the hole at low external fields (see Fig. 6.12 (a) & (e)). However, at larger external fields a quasi-vortex domain wall state was not seen. Instead, transverse domain walls of up and down chirality were pinned on the upper

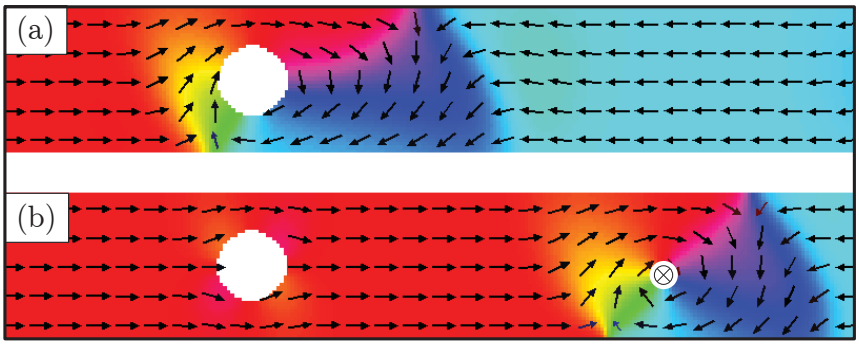

Figure 6.11: Depinning of a vortex domain wall from a cylindrical hole of diameter 50 nm in a 100 nm wide, 36 nm thick nanobar. (a) converged state showing pinned quasi-vortex of clockwise chirality and (b) non-converged state showing clockwise chirality down polarity vortex domain wall depinned.

and lower sides of the hole respectively. This micromagnetic state was seen for both initial vortex domain wall chiralities (see Fig. 6.12 (b) & (f)). Since this two transverse domain wall system was symmetric about the nanobar's long axis, when the domain walls subsequently depinned from the hole at higher external magnetic fields (see Fig. 6.12 (c) - (d) & (g) - (h)), the propagating vortex domain wall could employ a clockwise or anticlockwise chirality. In a perfect wire, a clockwise and an anticlockwise chirality are seen with equal probability, irrespective of the initial chirality, and as such a large cylindrical hole can be viewed as a chirality randomiser.

In order to understand the reason for the crossover from a quasi-vortex domain wall pinned over the hole (seen at diameter 60 nm) to two transverse domain walls pinned over the hole (seen at diameter 70 nm), the remanent energies of the two possible configurations were compared for different cylindrical hole diameters. As can be seen in Fig. 6.13, a quasi-vortex domain wall state is more energetically favourable than two transverse domain walls for cylindrical diameters $\leq$ 70 nm whereas the converse is true for diameters $\geq$ 80 nm. These results explain the presence of a crossover between the two regimes near 75 nm. The observation of two transverse domain walls at diameter 70 nm (shown in Fig. 6.12) despite the quasi-vortex domain wall's lower energy at remanence could be due to the non-zero field or the two states having very similar energies and a complex energy landscape between them.

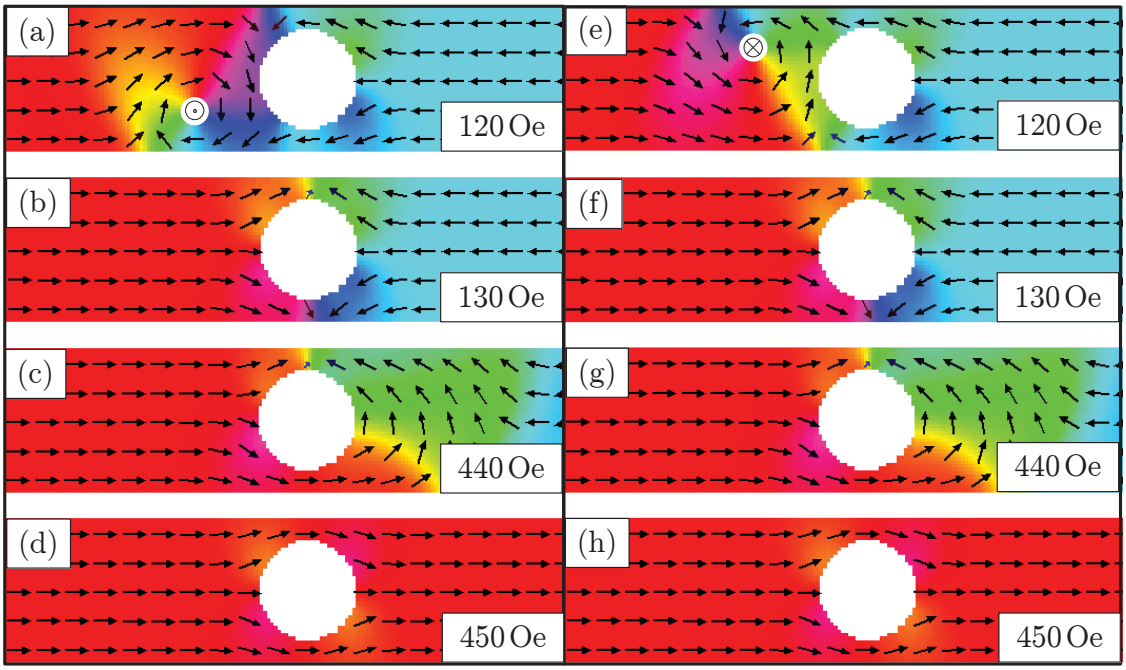

Figure 6.12: Chirality randomising of vortex domain walls incident on a cylindrical hole diameter 70 nm in a 100 nm wide, 36nm thick nanobar, showing (a) - (d) when a clockwise chirality up polarity domain wall is incident and (e) - (h) when an anticlockwise chirality down polarity domain wall is incident. Here the vortex may be pinned before the hole, shown in (a) & (e), however a quasi-vortex state is never seen. Instead an exchange favouring state is established, shown in (b) & (f), which is identical for both initial domain wall chiralities. This domain wall depins at higher external magnetic fields, the magnitude of which depends on the size of the constriction. (c) & (g) show the depinning process. (d) & (h) show the magnetic state after the domain wall has depinned from the hole.

6.2.2.2 Displaced cylindrical holes

The effect of displacing a 40 nm diameter cylindrical hole off-centre by a distance y was investigated. When the hole was displaced by a small amount, $y = -5$ nm, similar behaviour to that seen in Fig. 6.10 was observed for both chiralities, with a quasi-vortex domain wall pinned over the hole with chirality opposite to the initial chirality. However, when the cylindrical hole's displacement off-centre was $y = -10$ nm, different behaviour was seen. For an incident clockwise chirality up polarity domain wall, an anticlockwise quasi-vortex state was pinned over the hole as in the centered cylindrical hole situation shown in Fig. 6.10. This eventuality is shown in Fig. 6.14

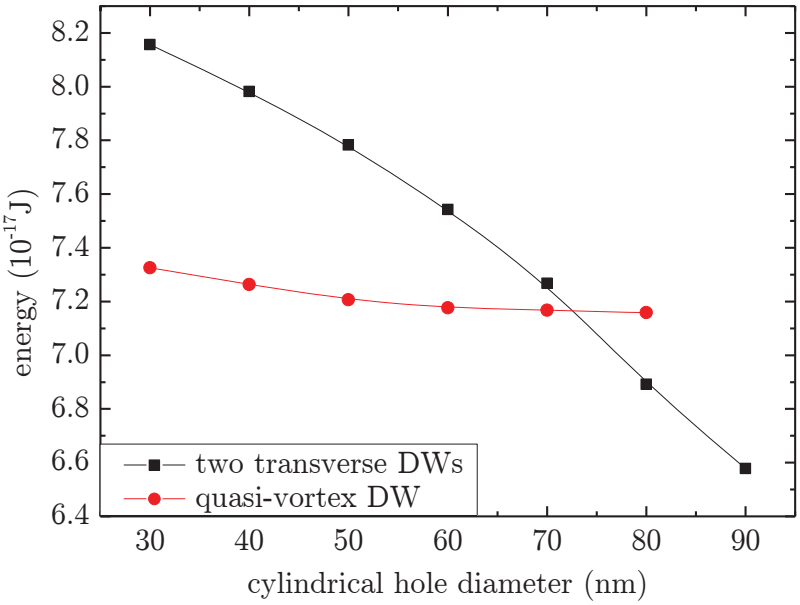

Figure 6.13: Comparison of energies at remanence of two transverse domain walls (see e.g. Fig. 6.12 (b) & (f)) and a quasi-vortex domain wall (see e.g. Fig. 6.10 (c) & (h)) pinned over centred cylindrical holes of different diameters. The lines are guides to the eye.

(a) - (c). However, for an incident anticlockwise chirality down polarity domain wall, the vortex core moved in a direction away from the displaced hole enabling the domain wall to propagate past the obstruction as a transverse domain wall at low field (210 Oe) without being pinned. Therefore, the field at which the area to the right of the hole reversed depended on the chirality of the incident domain wall (210 Oe for anticlockwise chirality down polarity and 490 Oe for clockwise chirality up polarity). As such, this displaced cylindrical hole acted as a vortex domain wall chirality filter.

Another type of behaviour was seen at a yet larger cylindrical hole displacement of $y = -20$ nm. Here the chirality of the quasi-vortex domain wall pinned over the hole no longer depended on the initial chirality. When the vortex core moved in increasing external magnetic fields in the same direction as the hole was displaced, the switching occurred as in Fig. 6.10 except at slightly different fields. This is illustrated in Fig. 6.15 (a) - (c). When, however, the vortex core moved in increasing external magnetic fields in the opposite direction to the hole, the leading edge of the domain wall was

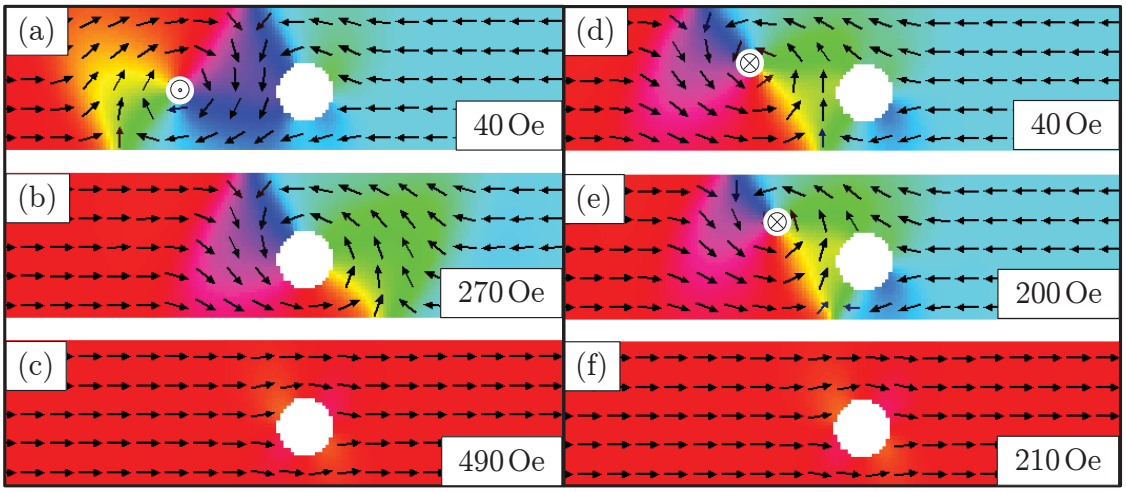

Figure 6.14: Chirality filtering: (a) - (c) clockwise chirality up polarity domain wall and (d) - (f) anticlockwise chirality down polarity domain wall incident on a 40 nm diameter cylindrical hole displaced off-centre by $y = -10$ nm in a 100 nm wide, 36nm thick nanobar. (a) shows the vortex pinned in front of the displaced hole, (b) shows the quasi-vortex domain wall pinned over the hole with the opposite chirality, and (c) shows the micromagnetic state after the domain wall has depinned from the hole. The sequence of events with this chirality is the same as for the centered hole situation. (d) shows the vortex pinned in front of the hole, (e) shows the vortex core migrating to the upper edge in increasing field and (f) shows the micromagnetic state after the domain wall has depinned from the hole. Note that for this chirality-polarity-displacement combination a quasi-vortex state is not pinned over the hole.

able to propagate past the obstruction first before the trailing edge (see Fig. 6.15 (d)). As such, the switching was different to the centred hole case, and the domain wall's chirality was conserved as it was pinned over the hole as a quasi-vortex ((see Fig. 6.15 (e))). Therefore domain walls of different chirality encountering the same displaced hole resulted in the same final chirality quasi-vortex domain wall pinned over the hole i.e. if the hole was displaced upwards, both initial clockwise chirality up polarity and anticlockwise chirality down polarity domain walls were pinned over the hole with clockwise quasi-vortex chirality, and if the hole was displaced downwards as in Fig. 6.15, both initial clockwise chirality up polarity and anticlockwise chirality down polarity domain walls were pinned over the hole with anticlockwise quasi-vortex chirality. Since the chirality of the domain wall subsequently depinned from the hole was that of the quasi-vortex (e.g. see Fig. 6.11), the depinned domain wall chirality

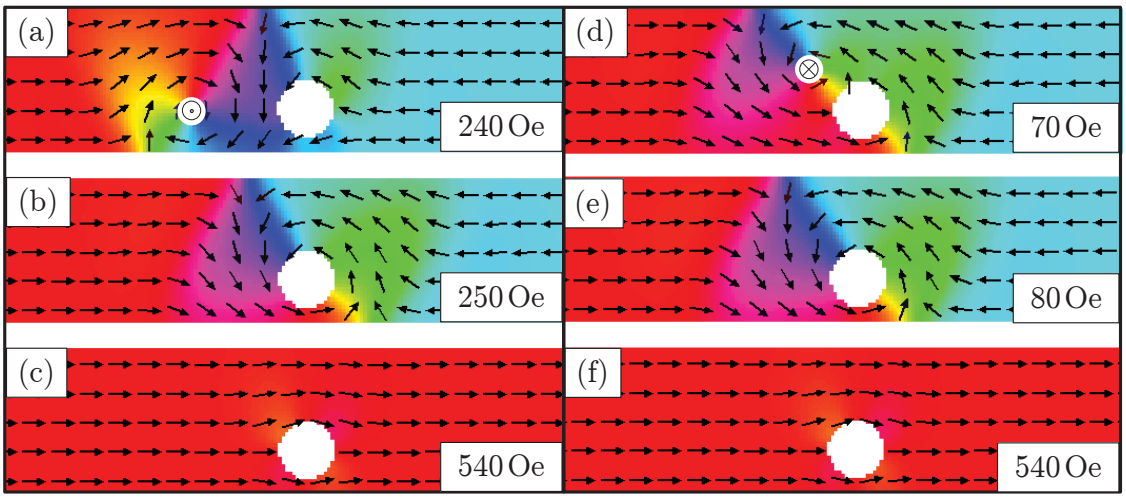

Figure 6.15: Chirality setting: (a) - (c) clockwise chirality up polarity domain wall and (d) - (f) anticlockwise chirality down polarity domain wall incident on a 40 nm diameter cylindrical hole displaced off-centre by $y = -20$ nm in a 100 nm wide, 36nm thick nanobar. (a) shows the vortex pinned in front of the displaced hole, (b) shows the quasi-vortex domain wall pinned over the hole with the opposite chirality, and (c) shows the micromagnetic state after the domain wall has depinned from the hole. The sequence of events with this chirality is the same as for the centered hole situation. (d) shows the vortex core pinned in front of the hole and the vortex's leading edge beyond the hole, (e) shows a quasi-vortex domain wall pinned over the hole with the same chirality and (f) shows the micromagnetic state after the domain wall has depinned from the hole. Note that in both cases an anticlockwise quasi-vortex domain wall is pinned over the hole.

was therefore independent of the initial domain wall chirality. As such, this displaced cylindrical hole acted as a vortex domain wall chirality setter.

In summary, the way in which a vortex domain wall interacts with a displaced cylindrical hole depends on its chirality and the hole's exact displacement. Displaced cylindrical holes may be used for both vortex domain wall chirality filtering and vortex domain wall chirality setting.

6.2.2.3 Elliptical small centred holes

A study into the effect that changing the ellipticity of centred holes has on the pinning and depinning fields of quasi-vortex domain walls was made. For all dimensions sim-

ulated, for incident clockwise chirality up polarity vortex domain walls, an identical mechanism to that shown in Fig. 6.10 was seen i.e. the vortex was pinned before the hole at low field, pinned over the hole as a quasi-vortex domain wall of anticlockwise chirality at higher field and subsequently depinned from the hole at still higher field. A typical x-component magnetisation vs. external field plot for a nanobar with a cylindrical hole of diameter 40 nm is shown in Fig. 6.16. The fields at which the

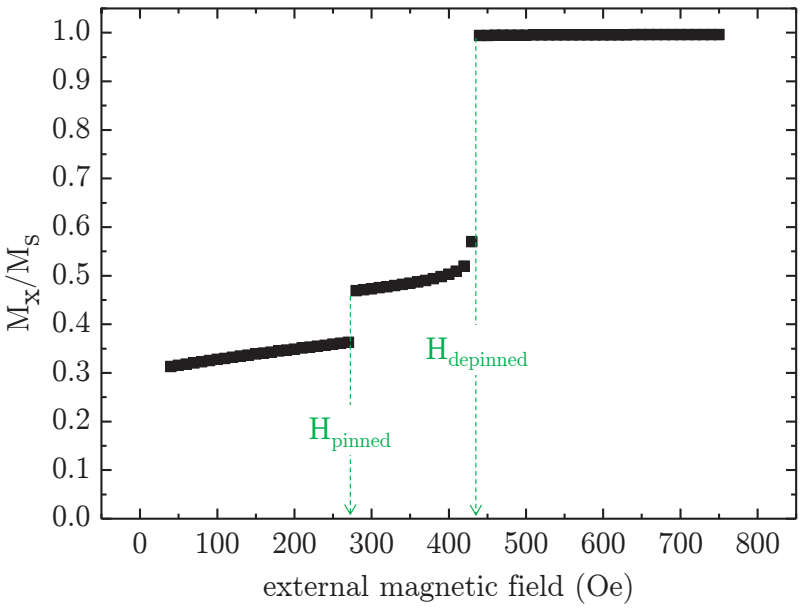

Figure 6.16: Normalised x-component of magnetisation vs. external field for a 100 nm wide, 36nm thick nanobar with cylindrical hole of diameter 40 nm after saturation in the negative x direction and the introduction of a clockwise chirality up polarity domain wall. The fields at which the domain wall is pinned over and subsequently depinned from the cylindrical hole are indicated in green.

domain wall is pinned over the hole as a quasi-vortex and depinned from the hole are clearly indicated. On analysis of data from many different geometries, these pinning and depinning fields of the domain wall over the hole were seen to depend on the hole's ellipticity (see Fig. 6.17). The field at which a quasi-vortex domain wall was pinned over the hole was found to decrease with increasing X and Y. In addition, the field at which the quasi-vortex domain wall depinned from the hole was found to increase with increasing X and surprisingly decrease with increasing Y. These results

mean that the ellipsoidal hole's exact geometry can be tailored in order to meet the external field requirements of a specific experiment. For example, if an ellipsoidal hole is required for vortex domain wall chirality and polarity readout, a large quasi-vortex pinning field may be desirable to maximise the window of vortex core stability. If this is indeed the case, an ellipsoidal hole with small Y should be used.

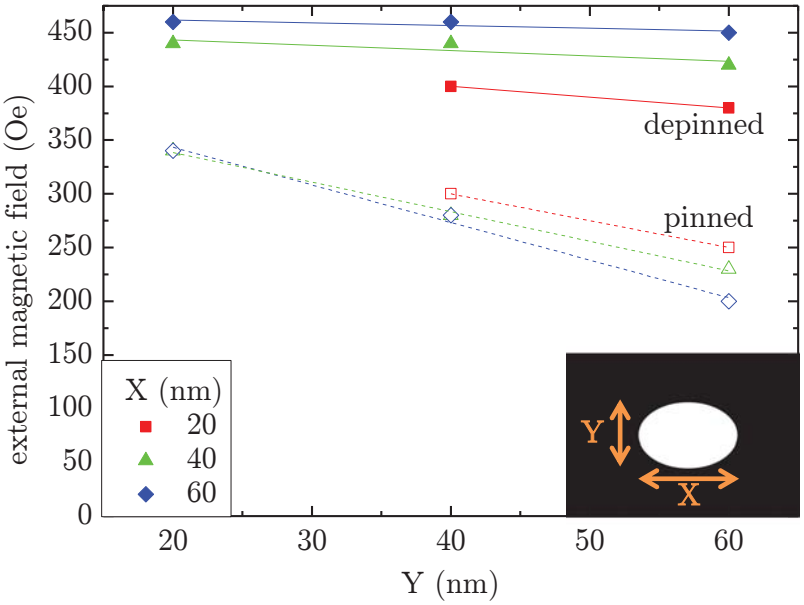

Figure 6.17: Stability of quasi-vortex domain wall as a function of dimensions and ellipticity of hole in a 100 nm wide, 36nm thick nanobar for an incident clockwise chirality up polarity domain wall. The open symbols represent the field at which a quasi-vortex domain wall is pinned over the hole (e.g. see Fig. 6.10 (c)) and the closed symbols represent the field at which the quasi-vortex domain wall subsequently depins from the hole (e.g. see Fig. 6.10 (e)). The lines are guides to the eye.

6.2.2.4 Rotated elliptical holes as chirality filters

The effect of rotating an ellipsoidal hole of lateral dimensions $Y = 40\,\text{nm}$ and $X = 60\,\text{nm}$ clockwise about its centre point was studied. For all rotations simulated a quasi-vortex domain wall was pinned over the hole with opposite chirality to that with which it was incident, with similar mechanisms to those shown in Fig. 6.10. Fig. 6.18 shows the fields at which the domain wall was pinned over and subse-

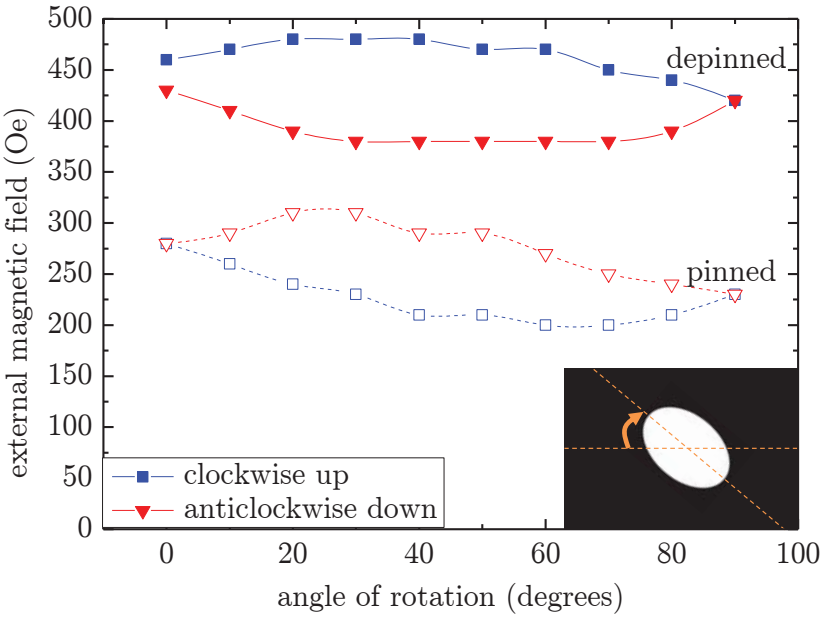

Figure 6.18: The effect of rotating the ellipsoidal hole of $Y = 40\,\text{nm}$ and $X = 60\,\text{nm}$ clockwise about its centre point in a 100 nm wide, 36nm thick nanobar, as indicated in the inset, on the pinning and depinning fields of the quasi-vortex domain wall. Open symbols indicate the fields at which the vortex domain wall is pinned over the hole as a quasi-vortex, closed symbols indicate the fields at which the quasi-vortex domain wall is depinned from the hole. Blue and red indicate incident clockwise chirality up polarity and anticlockwise chirality down polarity domain walls pinned as anticlockwise and clockwise quasi-vortex domain walls over the ellipsoidal hole respectively. The lines are guides to the eye.

quently depinned from the hole for clockwise chirality up polarity and anticlockwise chirality down polarity domain walls incident on rotated ellipsoidal holes. The angle of rotation of the hole is defined as per the inset, with 0° and 90° corresponding to symmetrical situations about the nanobar's long axis. Unsurprisingly, rotations of 0° and 90° yielded near identical characteristic fields for both chirality situations, with the small difference in depinning field at 0° occurring due to edge effects. However, for rotations resulting in holes not symmetrical about the nanobar's long axis, different characteristic fields for clockwise chirality up polarity and anticlockwise chirality down polarity domain walls were seen. The most significant difference occurred when the asymmetry was most pronounced i.e. near 45°.

The difference in the depinning fields from the ellipsoidal hole for domain walls of opposite chiralities can be understood by looking at the quasi-vortex domain wall stability. Fig. 6.19 (a) & (b) show the situations in which an anticlockwise chirality down polarity and clockwise chirality up polarity vortex domain wall are incident on the hole and are pinned over the hole as clockwise and anticlockwise chirality quasi-vortex domain walls respectively. The state shown in Fig. 6.19 (b) is more energetically favourable than Fig. 6.19 (a) in terms of both magnetostatic and exchange energies (values were obtained with the micromagnetic software [18]) and as such remains stable to higher external magnetic fields. The difference in pinning fields over the ellipsoidal hole for domain walls of opposite chirality can also be understood by studying energy considerations.

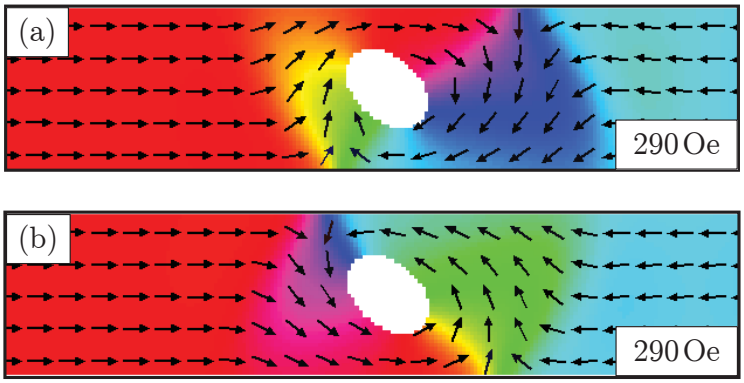

Figure 6.19: An ellipsoidal hole of lateral dimensions $Y = 40\,\text{nm}$ and $X = 60\,\text{nm}$ rotated at an angle of 40° in a 100 nm wide, 36nm thick nanobar. This geometry may be used as a chirality filter since the different vortex chiralities respond differently to the hole. (a) shows a clockwise quasi-vortex domain wall, the result of an incident anticlockwise chirality down polarity domain wall. This situation is not as favourable energetically as in (b) in which an anticlockwise quasi-vortex domain wall is shown, the result of an incident clockwise chirality up polarity vortex domain. This difference in stability is reflected in the depinning field of the quasi-vortex domain wall, which is 380 Oe for the situation shown in (a) as opposed to 480 Oe for that shown in (b).

Since the switching of the area to the right of the hole relies on the depinning of the quasi-vortex domain wall from the hole, a rotated ellipsoidal hole may be employed as a vortex domain wall chirality filter. A rotation of 40° yields the largest differential between depinning fields of different chiralities and as such should be employed for

optimal performance.

In order to verify the theories described here and throughout this section, these nanobars with ellipsoidal holes must be fabricated and tested experimentally. The exact details of future work continuing the investigation into ellipsoidal holes' functionality is provided in the following section.

6.3 Future work

In Section 6.1 and Section 6.2 of this chapter the potential functionality of triangular injection pads and ellipsoidal holes respectively was investigated. The next stages of these studies are outlined in detail below.

6.3.1 Triangular injection pads: notch filter method

As detailed in Section 6.1, the investigation into the controllable injection of a transverse domain wall with specific chirality via a triangular injection pad using an ASI vertex 1 μm away was inconclusive. To elucidate the injected domain wall's chirality in future work, a *notch filter method* will be employed. A notch is a small indentation of a semi-elliptical nature made on either the upper or lower side of the nanobar. The notch acts as a pinning site for the domain wall as it propagates down the nanobar (see Section 2.7.2.1). Due to the triangular shape of the transverse domain wall, up and down transverse chiralities are affected differently by the shape of the notch [22, 25–27] resulting in a chirality dependent depinning field. The notch filter method has already proved reliable in determining domain wall chirality [22, 26, 27].

Many nominally identical triangular injection pad systems will be made with notches fabricated at slightly different distances from the pad's mouth allowing the degree of Walker Breakdown to be judged. In addition, many injections from the same injection pads will be studied in order to gauge the influence of fabrication imperfections on the injected domain wall. The structures will be imaged again via STXM, PEEM or LTEM or their switching fields will be studied via Magneto Optic Kerr Effect Lensing. In this way more conclusive results should be achieved.

6.3.2 Ellipsoidal holes: investigating right-handed chirality-polarity permutations

In the ellipsoidal hole work described in Section 6.2, only incident clockwise chirality up polarity and anticlockwise chirality down polarity domain walls were studied. At first glance one would expect that changing the polarity of a domain wall of specific chirality should not influence its interaction with the ellipsoidal hole. However initial simulations of the remaining domain wall chirality-polarity combinations suggest that, although the behaviour is broadly similar, there are some subtle differences. As such, future work in this area includes running all the simulations in this section with the remaining chirality-polarity domain wall permutations and exploring possible reasons for any differences in behaviour observed for domain walls of the same chirality but opposite polarity.

6.3.3 Ellipsoidal holes: experimental verification

According to the micromagnetic simulations described in Section 6.2, ellipsoidal holes promise to be useful candidates for vortex domain wall chirality control. As such, details of both how nanobars with ellipsoidal holes could be fabricated and how their functionality could be studied experimentally are presented below.

6.3.3.1 Fabrication

Nanobars with ellipsoidal holes may be fabricated via an electron-beam lithography, thermal evaporation and lift-off technique as described in Section 3.1. However, problems with the lift-off of small features have been encountered in the past and as such, the successful lift-off of the material inside the hole may not be achieved. If this is indeed the case here, an alternative *top down* approach may be used in which unwanted material from a pre-grown thin permalloy film is removed via a negative resist (which after exposure to an electron-beam becomes insoluble to the developer), electron-beam lithography and ion-beam milling method.

Although the behaviours of ellipsoidal holes of diameters 10 nm to 90 nm have

been discussed in this chapter, it is unlikely that this range could be realised experimentally. Due to proximity effects [101] and the 20 kV accelerating voltage limit the current electron beam lithography system has (see Section 3.1.4), only diameters of approximately 40 nm to 60 nm appear feasible at this stage.

6.3.3.2 Experimentation

In order to test the theories described in Section 6.2, the chirality of the vortex domain wall approaching the hole must be known and the chirality of the vortex domain wall depinned from the hole must be measured. An off-centre ellipsoidal injection pad may be used to inject a vortex domain wall of known chirality, as demonstrated by McGrouther et al. [98]. A notch filter method, as described in Section 6.3.1 and by Bogart et al. [24], may be used to measure the chirality of the vortex domain wall beyond the ellipsoidal hole. This notch filter method relies on measuring the coercivity of the nanobar beyond the notch. The coercivity of the nanobar can be measured via an imaging method such as STXM, PEEM or LTEM. Alternatively it can be measured directly with MOKE so long as the nanobar is extended considerably ($> 5\,\mu$m) in order to accommodate the large laser spot.

In order to look at the micromagnetic state and, if necessary, the chirality of the quasi-vortex domain wall pinned over the hole, an imaging method could be used. Fig. 6.20 shows the simulated Lorentz Transmission Electron Microscopy (LTEM) electron phase contrast for incident (a) clockwise and (b) anticlockwise vortex domain walls achieved with the MALTS software [64] discussed in Chapter 4. The OOMMF images are identical to those shown in Fig. 6.10 (a), (c), (f) & (h). Since the electron phase contrast expected for the two different domain wall chiralities is significantly different and there is an LTEM facility at Imperial College London, LTEM seems the most suitable technique with which to start imaging these structures.

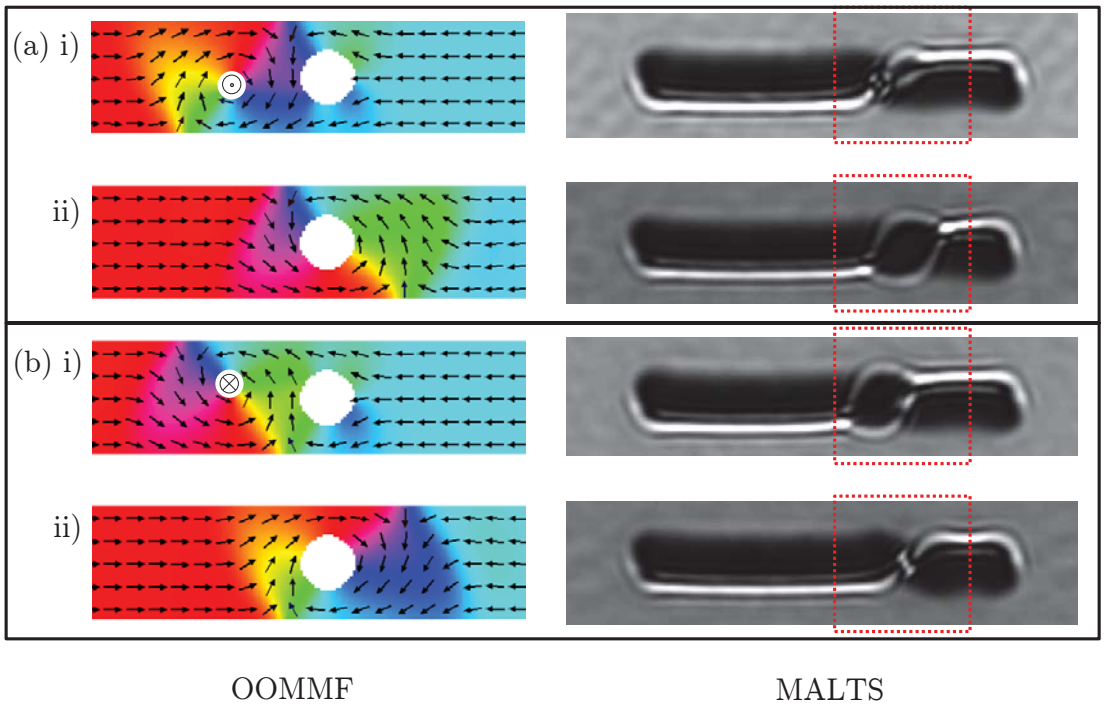

Figure 6.20: Expected LTEM electron phase contrast for pinned vortex and quasi-vortex domain walls at cylindrical holes. The nanobar shown here is 100 nm wide, 18 nm thick and supports a cylindrical hole of diameter 50 nm. Both micromagnetic OOMMF [18] and MALTS [64] simulations are shown for situations with (a) an incident clockwise chirality up polarity domain wall and (b) an incident anticlockwise chirality down polarity domain wall on a 50 nm diameter cylindrical hole. The OOMMF simulations directly correspond to those shown in Fig. 6.10 (a), (c), (f) & (h). The area of the micromagnetic simulation shown corresponds to the red boxed area in the MALTS simulation. For the MALTS simulations, a beam divergence of 0.01×10^{-3}, a defocus of 1600 µm, a spherical aberration coefficient of 0 and an accelerating voltage of 300 kV were used.

6.4 Summary

In this chapter, methods to control domain wall chirality in permalloy nanobars have been explored. Micromagnetic simulations and preliminary experimental data showing the injection of domain walls from triangular injection pads have been presented. Although the micromagnetic simulations strongly suggest that the chirality of the injected transverse domain wall can be set by the orientation of the triangular injection pad, the preliminary results are so far inconclusive. As such ideas for future work have been detailed.

Micromagnetic simulations showing the interaction of vortex domain walls with ellipsoidal holes have also been presented. Although these systems are yet to be realised experimentally, the simulations suggest that ellipsoidal holes may be used for vortex domain wall pinning, chirality and polarity readout as well as chirality changing, setting and randomising. If the future work fabricating and testing these systems discussed in this chapter is successful, ellipsoidal holes could prove to be invaluable for fully understanding and controlling the magnetic reversal of ASI in the vortex domain wall regime.

The treatment provided in this chapter ends the discussion of domain walls and ASI in this thesis. In the next chapter, the behaviour of Artificial Dipolar 2D-XY, a close relative of ASI, is analysed and discussed.

CHAPTER 7 : SINGLE DOMAIN NANODISCS FOR ARTIFICIAL DIPOLAR 2D-XY

As demonstrated in Chapter 5, Artificial Spin Ice (ASI), comprised of geometrically frustrated nanobars on a kagome lattice, has proved to be a very powerful model frustrated system whose direct imaging has revealed rich physics. ASI's ferromagnetic nanobars are single domain and these *Ising-macrospins* interact via the magnetic dipolar interaction giving rise to ice physics. Theoretically a complementary system is one in which individual spins are free to point in any direction within the plane. This situation is well described by the *Dipolar 2D-XY model*, the exact features of which are currently contested by theoreticians elsewhere. In this chapter the idea of realising an Artificial Dipolar 2D-XY structure in which the macrospins are single domain permalloy nanodiscs is presented. Preliminary results from single-spin-flip Metropolis Monte Carlo simulations on a kagome lattice are presented. In addition, data from preliminary investigations performed on nanodisc arrays via Lorentz Transmission Electron Microscopy, Scanning Transmission X-ray Microscopy and Superconducting Quantum Interference Device Magnetometry is shown and analysed.

7.1 Theory and literature from elsewhere

7.1.1 Phase transitions and universality

As discussed in Section 2.3.1, a material may behave ferromagnetically and show spontaneous ordering below a critical temperature, its Curie temperature, T_C. Above T_C, the material is disordered in the absence of an applied field and behaves paramagnetically [11]. This transition between ferromagnetic to paramagnetic behaviour is

an example of an order-to-disorder *continuous phase transition*, and the magnetisation, M, is said to be the *order parameter* of the ferromagnetic-paramagnetic phase transition; above T_C the order parameter is zero and below T_C it is non-zero. The behaviour of thermodynamic quantities near a system's critical temperature can be described in terms of *critical exponents*. For example, the order parameter, here the magnetisation, M, takes the form $M \propto (T_C - T)^\beta$ just below the critical temperature of the continuous phase transition. Here β is a *critical exponent*. Surprisingly, similar values for critical exponents have been seen for many different types of continuous phase transitions with the same dimensionality of the order parameter, D, the same dimensionality of the lattice, d, and the same range of forces. These include those with different lattice types and order parameters [102]. This is called *universality* and different subsets of critical behaviour correspond to different *universality classes*.

7.1.1.1 Correlation function

The *correlation function*, $C(r)$, is a measure used to gauge a system's order over distances r. In a spin system it is defined as

$$C(r) = \langle (\mathbf{S}(R+r) - \langle \mathbf{S} \rangle) \cdot (\mathbf{S}(R) - \langle \mathbf{S} \rangle) \rangle, \tag{7.1}$$

in which $\mathbf{S}(R+r)$ and $\mathbf{S}(R)$ are spin vectors separated by a distance r, and $\langle \mathbf{S} \rangle$ is the average spin direction of all the spins in the lattice. The total average is performed over many independent states at a given temperature.

At a phase transition, the degree of ordering of the system changes and this change is reflected in the correlation function. As such, calculation of a system's correlation function can provide an insight into a system's critical behaviour.

7.1.2 2D-XY model

The 2D-XY universality class with $D = 2$ and $d = 2$ describes nearest neighbour interactions of vectors in the xy-plane confined to point in the xy-plane. The Hamiltonian

of this universality class is

$$H = -J \sum_{<i,j>} \mathbf{S}_i \cdot \mathbf{S}_j, \tag{7.2}$$

in which $\mathbf{S}_i$ and $\mathbf{S}_j$ are vectors in the xy-plane, J is some coupling constant and $< i, j >$ indicates that the sum is over nearest neighbours alone. Exchange interacting spins whose orientations are confined to the xy-plane fall into this universality class.

Unusually, in an infinite 2D-XY system there is no order-disorder continuous phase transition. This is because there is an absence of spontaneous magnetisation for all non-zero temperatures. However, a *Kosterlitz-Thouless* transition [103,104] can occur which separates a low temperature phase of bound vortex-anti-vortex pairs characterised by a power law correlation function, and a high temperature phase in which free vortices and antivortices occur characterised by an exponential correlation function. Finite 2D-XY systems, however, behave somewhat differently, with an ordered low temperature phase of finite magnetisation and an order-to-disorder continuous phase transition characterised by a critical exponent $\beta = 0.23$ [7,105]. The temperature at which this phase transition occurs depends on the exact size, L, of the lattice and as such, 2D-XY systems are said to exhibit *finite size effects*.

7.1.3 Dipolar 2D-XY model

In the *Dipolar 2D-XY model*, dipolar interactions as well as nearest neighbour interactions are considered. This Dipolar 2D-XY model is characterised by the Hamiltonian

$$H = -J \sum_{<i,j>} \mathbf{S}_i \cdot \mathbf{S}_j + D_p \sum_{i \neq j} \frac{\mathbf{S}_i \cdot \mathbf{S}_j}{r_{ij}^3} - 3\frac{(\mathbf{S}_i \cdot \mathbf{r}_{ij})(\mathbf{S}_j \cdot \mathbf{r}_{ij})}{r_{ij}^5}, \tag{7.3}$$

in which the first term is identical to that in Eq. 7.2, $\mathbf{r}_{ij}$ is the vector separating two spins $\mathbf{S}_i$ and $\mathbf{S}_j$ at positions i and j, D_p is the dipolar constant, and the sum is over all i and j for $i \neq j$.

There is currently some disagreement as to how Dipolar 2D-XY systems behave. Bramwell and Holdsworth's work [7] suggests that they fall into the 2D-XY universality class whereas the work of others presents a different picture. Mol et al. found a set of critical exponents around an order-disorder phase transition which

did not fit into any known universality class [8] whilst Maeier and Schwabl noted a ferromagnetic phase transition which shared similarities with a Kosterlitz-Thouless transition [9]. Furthermore, Baek et al. suggested that the lattice geometry is important [10], with pure magnetic dipoles ($J = 0$) on square lattices undergoing an order-disorder phase transition belonging to the 2D Ising universality class and those on honeycombs exhibiting a Kosterlitz-Thouless transition. The study of Dipolar 2D-XY systems experimentally could provide key articulations for these theories and as such, the experimental realisation of Dipolar 2D-XY systems is discussed below.

7.2 Experimental realisation of 2D-XY and Dipolar 2D-XY systems

Although real spin systems are typically three dimensional and their behaviour is governed by exchange, dipolar and magnetocrystalline considerations simultaneously, some systems do exhibit quasi 2D-XY characteristics, namely layered magnets [7] and ultrathin films [106] with in-plane anisotropies. As such, these materials have been used to explore 2D-XY behaviour. Fortunately, advances in nanofabrication in recent years mean that artificial systems well described by the Dipolar 2D-XY model (with $J \approx 0$) may now be realised enabling the comparison of experimental results with previous theoretical work described in Section 7.1.3. In the following section the possibility of fabricating an Artificial Dipolar 2D-XY system comprised of single domain permalloy nanodiscs is explored.

7.2.1 From Artificial Spin Ice to Artificial Dipolar 2D-XY

Nanobars in ASI behave like Ising macrospins due to their large aspect ratio and hence large shape anisotropy. Nanodiscs with no in-plane shape anisotropy are therefore obvious candidates with which to construct complementary XY-systems comprised of macrospins free to point in any direction in the xy-plane. In the next section the dimensions with which permalloy nanodiscs support *single domain* macrospin-like states are explored with a view to realising Artificial Dipolar 2D-XY from arrays of

these single domain nanodiscs.

7.2.1.1 Nanodisc dimensions for single domain states

A nanodisc is a cylindrical element with nano-sized dimensions. The magnetisation configuration a ferromagnetic nanodisc supports depends on its dimensions [107] and its magnetocrystalline anisotropies. The following is true if the material has negligible magnetocrystalline anisotropy like permalloy. If the nanodisc is thin and small in radial extent it supports a single domain in-plane magnetised state comprising approximately collinear magnetic moments (see Fig. 7.1 (a)). However, if the nanodisc is

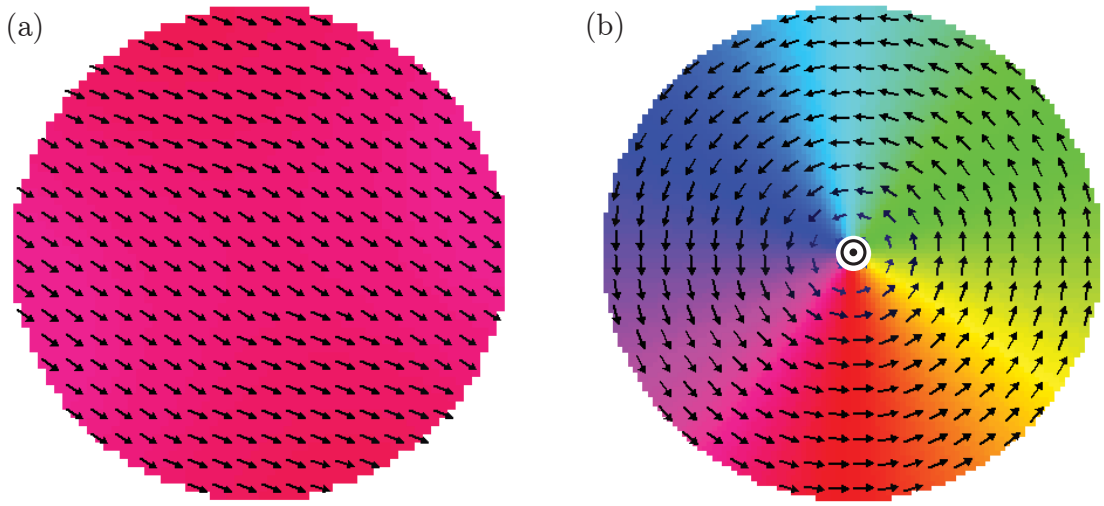

Figure 7.1: Micromagnetic simulations [18] of a permalloy nanodisc (a) 60 nm diameter 20 nm thick supporting a single domain state and (b) 100 nm diameter 30 nm thick supporting an anticlockwise chirality up polarity vortex state. Mesh sizes of [1 nm, 1 nm, 5 nm] were used.

thick or large in radial extent it supports a vortex state comprising magnetic moments curling around a central core (see Fig. 7.1 (b)). This vortex state arises here because the magnetostatic energy benefit associated with partial flux-closure outweighs the exchange energy penalty incurred through curling. Finally if the structure's thickness is comparable to or greater than its diameter, an out-of-plane magnetisation state is supported comprising magnetic moments aligned approximately collinearly along the cylindrical axis. These dimensions are quantified for permalloy nanodiscs in Fig.

7.2. In the next section a new frustrated architecture comprised of nanodiscs which are sufficiently small to support in-plane single domain states is introduced, and the degree to which it acts as a Dipolar 2D-XY system is discussed.

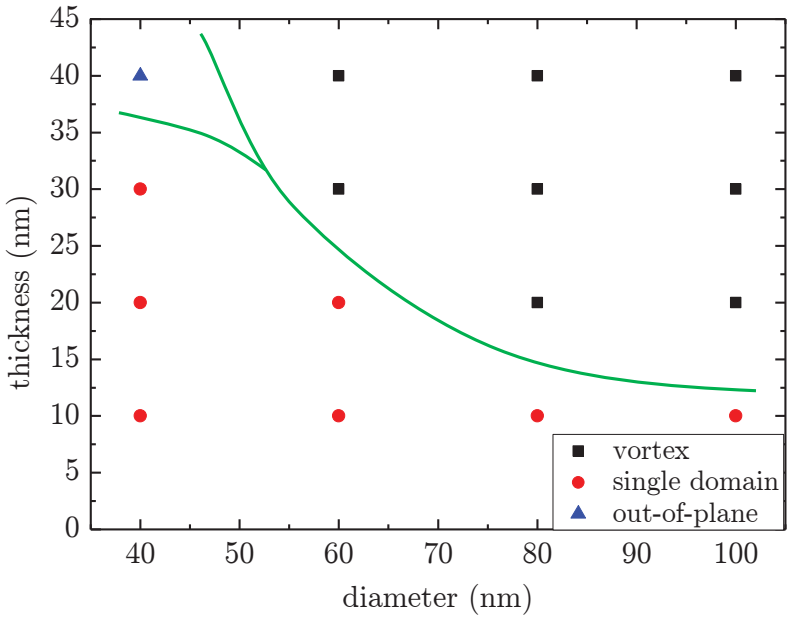

Figure 7.2: Phase diagram obtained via micromagnetic simulation [18] showing the remanent magnetic states in permalloy nanodiscs of different diameters and thicknesses. Mesh sizes of [1 nm, 1 nm, 5 nm] were used. The green lines are guides to the eye.

7.2.1.2 Arrays of single domain nanodiscs for Artificial Dipolar 2D-XY

If each nanobar in ASI is replaced by a single domain nanodisc, a new frustrated system termed *Kagome Artificial Dipolar 2D-XY* is created. The relationship between ASI and Kagome Artificial Dipolar 2D-XY is shown in Fig. 7.3. This system can only be modelled as a pure Dipolar 2D-XY system if the single domain nanodiscs behave as pure Dipolar XY macrospins. This can only arise if the following perturbations to the nanodiscs' dipolar behaviour can be made negligibly small:

1. exchange coupling between nanodiscs
2. in-plane magnetocrystalline anisotropy

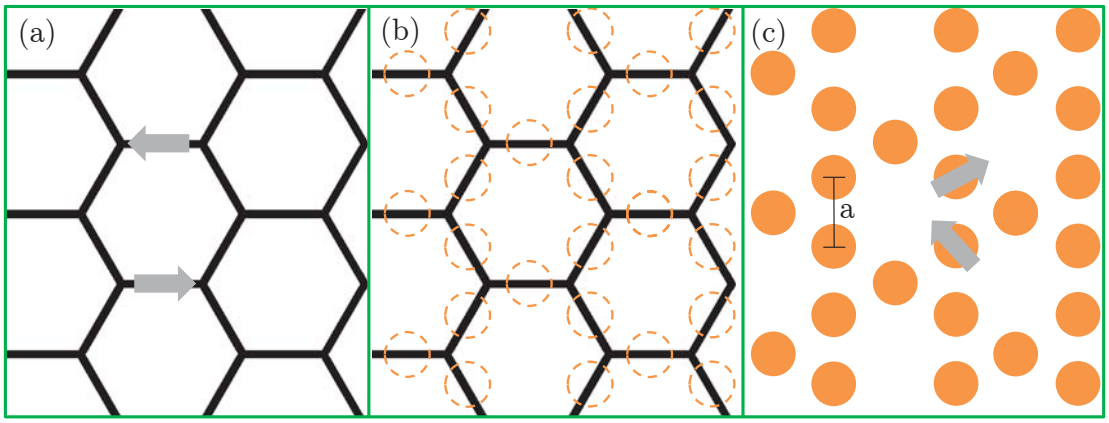

Figure 7.3: A schematic showing (a) ASI (black indicates ferromagnetic material, white indicates empty space) (b) the relation of the nanodisc geometry (dashed orange) to ASI (black) (c) Kagome Artificial Dipolar 2D-XY (orange indicates magnetic material, white indicates empty space). The grey arrows indicate possible local magnetisation directions, in (a) restricted to one of two directions and in (c) restricted to any direction within the xy-plane. The lattice separation, a, is defined in (c).

3. higher order multipolar terms.

The first perturbation is small so long as the edge-to-edge separation of the nanodiscs is much larger than the exchange length of the material (the exchange length of ferromagnetic permalloy is 5.7 nm [108]).

The second perturbation is small if the nanodiscs are fabricated out of permalloy which has near zero magnetocrystalline anisotropy (see Section 2.9).

The magnitude of the third perturbation can be estimated with reference to Mikuszeit et al.'s [109, 110] study of the multipole moments of a uniformly in-plane magnetised nanodisc. In this investigation, the next non-zero term in the multipole expansion after the dipolar term was found to be the octupolar term and the ratio between these two contributions was found to have the following dependence on the thickness, h, of the disc, the radius, r_0, of the disc and the distance, r, away from the disc:

$$\frac{\textit{octupolar contribution}}{\textit{dipolar contribution}} = \frac{\sqrt{2}(h^2 - 3r_0^2)}{4\sqrt{3}r^2}. \tag{7.4}$$

As can be seen from this equation, the nanodisc looks increasingly like a pure dipole the further away the observer moves. For nanodiscs of $h = 15\,\text{nm}$, $r_0 = 30\,\text{nm}$ and lattice separation $a = 100\,\text{nm}$,

$$\frac{octupolar\ contribution}{dipolar\ contribution} \approx -0.05. \tag{7.5}$$

As such, perturbations due to higher order multipolar terms may be neglected for single domain nanodiscs of approximately these dimensions and separations.

7.2.1.3 Advantages of Artificial Dipolar 2D-XY

There are many advantages associated with using Artificial Dipolar 2D-XY over quasi 2D-XY systems for the experimental verification of theory. These advantages are listed below:

1. Many different lattice geometries may be readily explored.
2. The strength of the interactions may be tuned by altering the lattice separation.
3. A true single-layered XY-system may be achieved.
4. Only negligibly small in-plane anisotropies exist if permalloy is used.
5. The nanodiscs' macrospins are sufficiently large for direct imaging.

In the next section, attempts to simulate the behaviour of Artificial Dipolar 2D-XY via a Metropolis Monte Carlo algorithm are detailed.

7.3 Metropolis Monte Carlo simulations of dipole-dipole interacting spins on a kagome lattice

The groundstate of perfect dipoles on a kagome lattice is known to be a macroscopic vortex for a finite lattice and a tessellating configuration with perfect sublattice ordering for an infinite lattice [111]. However, in order to understand the influence of

temperature, external magnetic field and lattice separation on the magnetisation configuration of dipoles in a kagome geometry, single-spin-flip Metropolis Monte Carlo simulations were performed. This Metropolis Monte Carlo algorithm produces an ensemble of Boltzmann distributed states at a given temperature, lattice separation and external magnetic field. As such, simulations demonstrating dipoles' behaviour under different conditions can be performed and the results can be used to aid the understanding of experimental Kagome Artificial Dipolar 2D-XY data.

In this section the exact details of the single-spin-flip Metropolis Monte Carlo simulations performed in this thesis are provided. In addition, preliminary results are analysed and discussed.

7.3.1 Method

The dipole-dipole interactions between single domain nanodiscs in a kagome lattice were investigated. The energy of two interacting dipoles is given by

$$E_{dipole-dipole} = \frac{\mu_0}{4\pi r_{ij}^3}\Big(\frac{\mathbf{m}_i \cdot \mathbf{m}_j}{r_{ij}^3} - 3\frac{(\mathbf{m}_i \cdot \mathbf{r}_{ij})(\mathbf{m}_j \cdot \mathbf{r}_{ij})}{r_{ij}^5}\Big), \tag{7.6}$$

in which $\mathbf{m_i}$ and $\mathbf{m_j}$ are the magnetisation vectors of the two dipoles i and j, $\mathbf{r}_{ij}$ is the vector joining their two centres. Each nanodisc was considered to be a point dipole with magnetisation $4.52\times10^{-17}\,\mathrm{JT}^{-1}$ corresponding to the magnetisation from a nanodisc of radius 30 nm and thickness 20 nm. The simulation comprised 972 nanodiscs (and hence dipoles) in total which is equivalent to 162 unit cells. The unit cells were configured in a rhombus shaped super cell illustrated in Fig. 7.4 (a). Periodic boundary conditions and the minimum image convention were employed; each nanodisc interacted with the closest image of all the other nanodiscs.

Initially each nanodisc was assigned a random in-plane magnetisation direction between 0 and 2π and the energy of this system was calculated. Then a single-spin-flip Metropolis Monte Carlo Method [112] was used to explore the Boltzmann distribution of states of the system. As such, one of the 972 nanodiscs was selected randomly. The magnetisation direction of this chosen disc was then randomised and

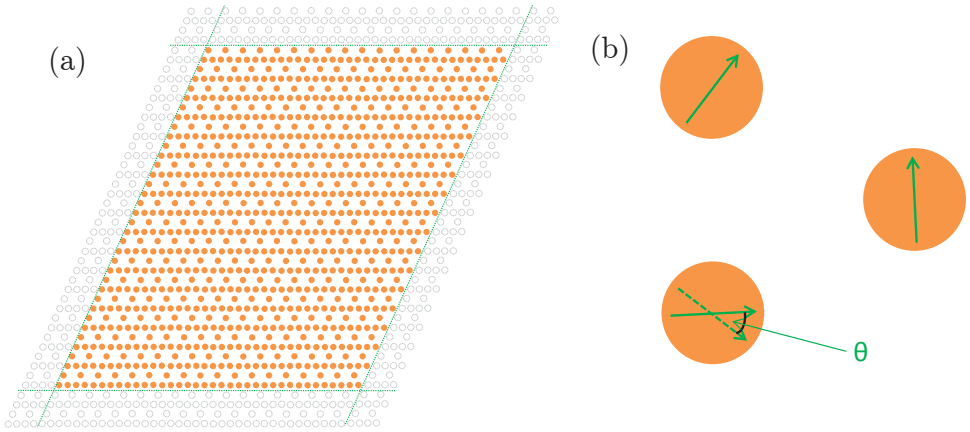

Figure 7.4: (a) the 972 nanodisc kagome lattice super cell used in the single-spin-flip Metropolis Monte Carlos simulations. (b) schematic of the single-spin-flip Metropolis Monte Carlo method showing the initial state of energy $E_{initial}$ (solid arrows) and the trial energy state of energy E_{trial} (solid and dashed arrow). The probabilities of acceptance of the new trial state are detailed in Table 7.1.

the new trial energy of the system was calculated (see Fig. 7.4 (b)). The trial energy was then compared with the initial energy and if the trial energy was lower than the initial energy, the trial magnetisation state was accepted and became the new initial configuration for the next iteration. However if the trial energy was higher than the initial energy, the trial magnetisation state was accepted with a probability $\exp(-((E_{trial} - E_{initial})/k_BT))$, in which k_B is the Boltzmann constant. A summary of the acceptance probabilities described here is provided in Table 7.1.

	probability of acceptance
$E_{trial} < E_{initial}$	1
$E_{trial} > E_{initial}$	$\exp(-((E_{trial} - E_{initial})/k_BT))$

Table 7.1: The probabilities of the acceptance of a new spin configuration of energy E_{trial} in the single-spin-flip Metropolis Monte Carlo algorithm.

Single-spin-flip Metropolis Monte Carlo simulations as described above were performed on the Imperial College High Performance Computing facility. This facility has a maximum run time of 72 hours enabling the computation of approximately $4 \times 10^5 \times 972$ single flips. For the energy versus temperature simulations, the first

$1 \times 10^4 \times 972$ iterations were discarded in the *burnout period* to ensure that the final result did not depend on the initial spin configuration. The minimum energy reached during the $4 \times 10^5 \times 972$ iterations was recorded and the average energy of the simulation was calculated for the last $4 \times 10^5 \times 972 - 1 \times 10^4 \times 972 = 3.9 \times 10^5 \times 972$ iterations. For the magnetisation versus external field simulations, the system started in a random spin configuration and was run for 500×972 iterations at 0.1 Oe intervals between -10 Oe and 10 Oe and subsequently between 10 Oe and -10 Oe.

There are a number of problems associated with a single-spin-flip Metropolis Monte Carlo method such as the one described above. The main problems are identified in Table 7.2 and ways in which they can be avoided and checked for are also provided. For the simulations in this thesis, the burnout period, number of iterations and periodic lattice size were all chosen to be as large as reasonably possible.

potential problem	**prevention and check**
burnout period too small	maximise burnout period and check that autocorrelation between states over burnout timescales is negligible
system stuck in local minimum due to small acceptance probabilities at low temperature	maximise number of iterations in simulation and check for convergence in identical simulations with different initial states
periodic boundary conditions introducing artificial periodicity	maximise periodic boundary size and repeat simulation for slightly different periodic boundaries

Table 7.2: Summary of the potential problems associated with the single-spin-flip Metropolis Monte Carlo simulation method [113, 114]. Ways in which one can avoid and check for these problems are also detailed.

7.3.2 Preliminary results

Simulations calculating the mean energy, E, for a given temperature, T, and lattice separation, a, in the absence of a magnetic field were performed. The results of this investigation are shown in Fig. 7.5. A general trend for the energy of the system to increase with increasing temperature was seen for all lattice separations studied,

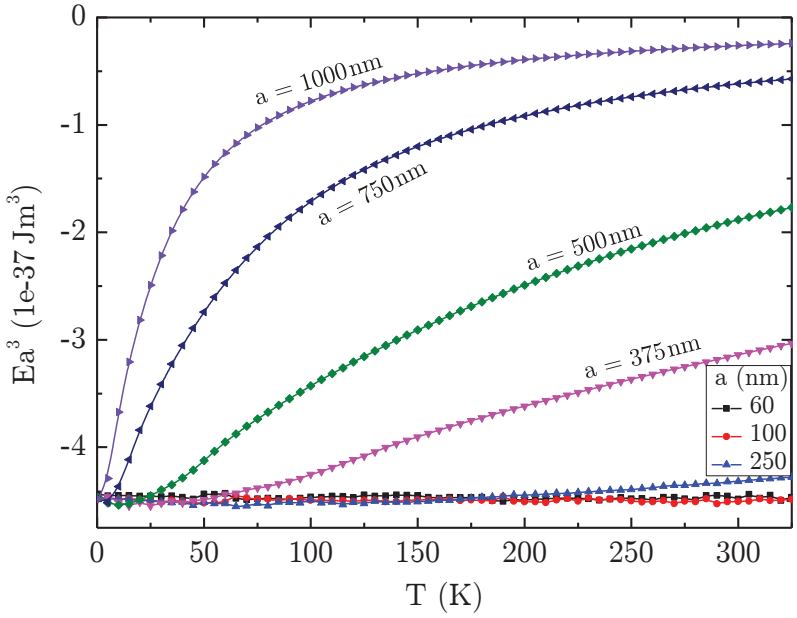

Figure 7.5: Simulated mean energy, E, as a function of temperature, T, for Kagome Dipolar 2D-XY lattices of different lattice separations, a. The results are plotted as Ea^3 vs. T to aid comparison. The lines are guides to the eye.

as expected. However, different shaped curves were seen for different lattice separations. Most interestingly, for the smallest lattice separations studied, an increase in temperature barely affected the energy of the system. And for the largest lattice separation studied, $a = 1000\,\text{nm}$, there appeared to be two different regimes, a low temperature regime in which dipolar interactions were obviously important, and a high temperature more disordered regime at $T \gtrsim 200\,\text{K}$ in which an increase in temperature barely affected the energy of the system. (Note that a perfectly disordered state has zero mean energy). As expected, both the simulated minimum and mean energies (shown in Fig. 7.5) fell onto a universal curve of Ea^3 vs. Ta^3, as shown in Fig. 7.6. The universal curve illustrates the fact that two systems of the same Ta^3 should behave identically since the probability of acceptance of a less favourable energy state is identical for both systems (see Table 7.1).

The field response of a kagome lattice, $a = 250\,\text{nm}$, was also simulated for comparison with experimental data shown later in Fig. 7.8. The results at temperatures at the extremities of the experimental range, $T = 5\,\text{K}$ and $T = 300\,\text{K}$, are shown in

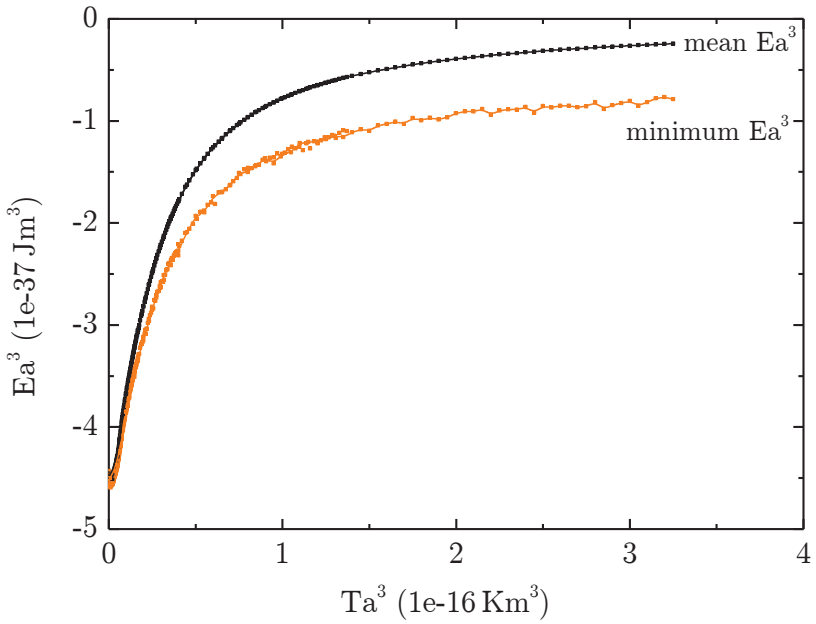

Figure 7.6: Universal curve (Ea^3 vs. Ta^3) onto which data in Fig. 7.5 falls. The lines are guides to the eye.

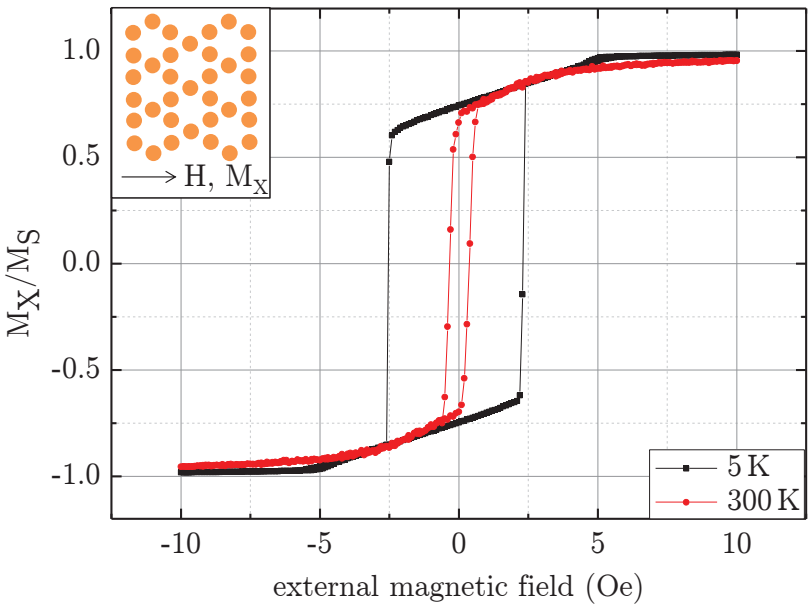

Figure 7.7: Simulated magnetisation as a function of applied field for a kagome nanodisc lattice, separation $a = 250\,\mathrm{nm}$, at $T = 5\,\mathrm{K}$ and $T = 300\,\mathrm{K}$.

Fig. 7.7. As expected, the coercivity of the array was seen to be significantly reduced when the thermal energy was increased (from 2.4 Oe at 5 K to 0.4 Oe at 300 K).

The preliminary Metropolis Monte Carlo simulations of Kagome Artificial Dipolar 2D-XY lattices shown in this section clearly indicate interesting behaviour for lattice separations $a = 60\,\text{nm}$ to $a = 1000\,\text{nm}$ in the temperature range 0.5 K to 350 K. As such Artificial Dipolar 2D-XY lattices with lattice separations in this range were fabricated and tested experimentally, the precise details of which are included in the next section.

7.4 Preliminary experimental measurements on Artificial Dipolar 2D-XY

Permalloy nanodisc arrays, termed Artificial Dipolar 2D-XY, were grown via an electron beam lithography, thermal evaporation and lift-off technique (see Section 3.1). Magnetisation vs. external field and magnetisation vs. temperature measurements were performed with a SQUID magnetometer (by Megha Chadha) in order to probe the systems' interaction strengths. In addition, attempts to elucidate the magnetisations of individual nanodiscs with Magnetic Force Microscopy (by Megha Chadha), Lorentz Transmission Microscopy (by myself and Solveig Felton) and Scanning Transmission X-Ray Microscopy (by our synchrotron team) were made. Details of these investigations are presented below.

7.4.1 Superconducting Quantum Interference Device magnetometry

Arrays comprising 6×10^7 nanodiscs of diameter 60 nm and thickness 14 nm were fabricated for bulk magnetometry experiments. The samples were firstly studied with Vibrating Sample Magnetometry. However, limitations on the size of the array (maximum area $\approx 4\,\text{mm} \times 4\,\text{mm}$) due to the small sample space meant that the array's magnetisation ($\approx 2 \times 10^{-6}$ emu for the 6×10^7 nanodiscs at saturation) was too small to be resolved (Quantum Design PPMS VSM's sensitivity 10^{-6} emu). Therefore a more sensitive SQUID magnetometer Quantum Design MPMS-7 (sensitivity 10^{-8} emu) at the London Centre for Nanotechnology was used in order to continue the investigation. So that the magnetic response of the nanodisc arrays alone could be analysed, a field-dependent magnetisation term due to the diamagnetic contribution of the sample substrate and holder was subtracted from all SQUID data sets. When magnetisation field dependence was explored, data was taken between -5000 Oe and 5000 Oe. However to improve clarity, data corresponding to saturated states beyond ± 1500 Oe has been omitted from the figures shown in this section.

Magnetisation versus external field measurements were taken for a kagome lattice of separation $a = 250\,\text{nm}$ at $T = 5\,\text{K}$ and $T = 293\,\text{K}$. These results are shown in

Fig. 7.8. The coercivity of the lattice was found to be 250 Oe at 5 K and only 3 Oe at

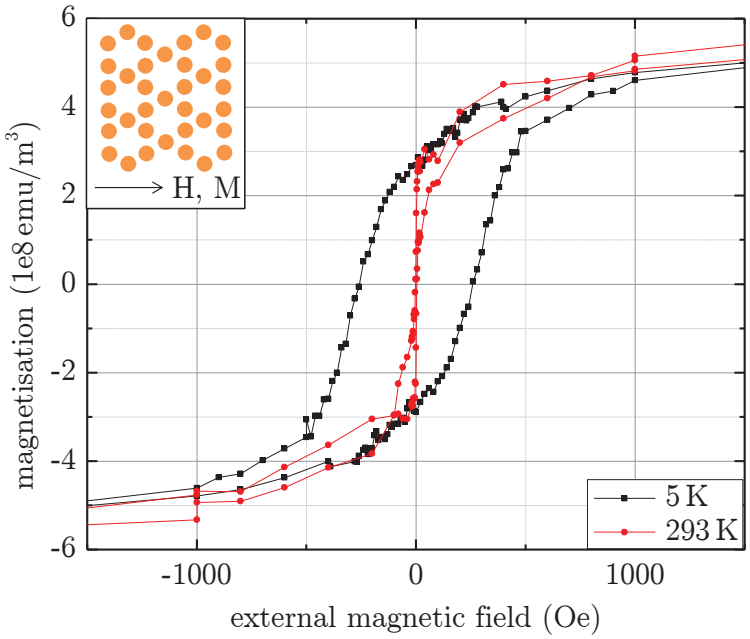

Figure 7.8: Hysteresis loops for nanodiscs in a kagome lattice $a = 250\,\text{nm}$ at $T = 5\,\text{K}$ (coercivity 250 Oe) and $T = 293\,\text{K}$ (coercivity 3 Oe). The inset indicates both the external field and magnetisation measurement directions.

293 K. Although this trend is in agreement with that seen in the simulation shown in Fig. 7.7 which suggests that the nanodiscs do indeed interact, there is a considerable discrepancy between the magnitudes of the coercivities. This arises because in the simulation the nanodiscs are approximated as point dipoles (with zero coercivity if isolated) whereas in reality the nanodiscs are extended macrospins with non-zero coercivities and pinning sites.

Further magnetisation versus external field measurements were taken for a kagome lattice at $T = 5\,\text{K}$ for different lattice separations $a = 160\,\text{nm}$, $a = 250\,\text{nm}$ and $a = 450\,\text{nm}$. The results of this study are shown in Fig. 7.9 (a). From this figure it is clear that, although the hysteresis loops for different lattice separations are broadly similar, there is a variation in their coercivities. Since all three nanodisc samples were fabricated using the same recipe and were in the same thermal evaporation, this result, which is summarised in Fig. 7.9 (b), indicates that a change in lattice

parameter alters magnetic reversal behaviour and as such, that the nanodiscs are interacting. The fact that the coercivity peaks at $a = 250\,\text{nm}$ is surprising as it was expected to simply decrease with increasing lattice separation. The cause of this interesting result is so far unclear and reproducibility checks (see Section 7.5) must be performed before any firm conclusions are drawn.

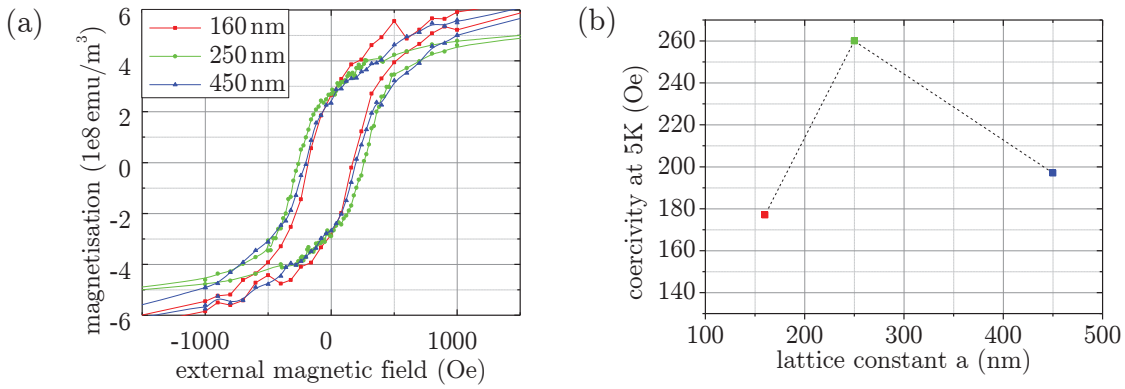

Figure 7.9: (a) hysteresis loops for nanodiscs in a kagome lattice at $T = 5\,\text{K}$ for $a = 160\,\text{nm}$, $a = 250\,\text{nm}$ and $a = 450\,\text{nm}$. The external field and magnetisation measurement directions are identical to that shown in the inset of Fig. 7.8. (b) coercivity at 5 K as a function of kagome lattice separation. The lines are guides to the eye.

Still further magnetisation versus external field measurements were taken for kagome and square geometries of identical lattice separation, $a = 250\,\text{nm}$, at $T = 5\,\text{K}$ and $T = 293\,\text{K}$. These hysteresis loops are shown in Fig. 7.10. Although the kagome and square lattices had similar coercivities at 5 K ($\approx 262\,\text{Oe}$), the dissimilarity in hysteresis loop shape suggests that the magnetisation field response was different for the two geometries. At 293 K this difference in behaviour was more pronounced and the kagome lattice's coercivity (3 Oe) was found to be considerably smaller than the square's (64 Oe). Since both kagome and square nanodisc samples were fabricated using the same recipe and were in the same thermal evaporation, it appears that it is the location and number of neighbouring nanodiscs that affects the reversal behaviour of the nanodiscs and that, as such, the nanodiscs are indeed interacting. The origin of the similar behaviour at low temperature but markedly different behaviour at high temperature, however, is not yet known.

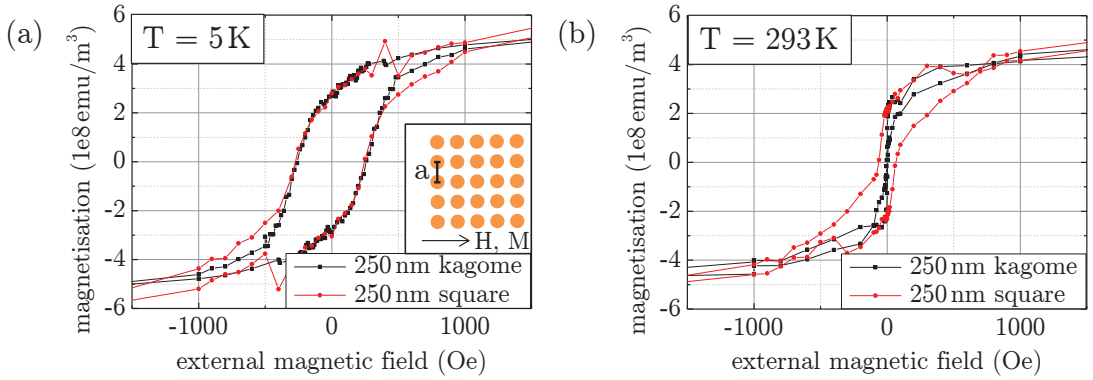

Figure 7.10: Hysteresis loops for nanodiscs in kagome and square lattices of $a = 250\,\text{nm}$ at (a) $T = 5\,\text{K}$ and (b) $T = 293\,\text{K}$. The inset here in (a) and the inset in Fig. 7.8 illustrate both the external field and magnetisation measurement directions for the square and kagome lattices respectively.

Zero field cooled (ZFC) and field cooled (FC) magnetisation versus temperature measurements were performed on kagome lattices with separations $a = 160\,\text{nm}$, $a = 250\,\text{nm}$ and $a = 450\,\text{nm}$. Here, the sample was demagnetised and subsequently cooled from 360 K to 5 K in the absence of an external magnetic field. Its magnetisation was then measured (ZFC measurement) as it was warmed from 5 K to 360 K, at approximately $2\,\text{Kmin}^{-1}$, in an in-plane external field of 10 Oe in the direction shown in the Fig. 7.8 inset. As such the sample started with near-zero magnetisation which it retained on cooling but not on subsequent (measured) heating. Next the sample was cooled back down from 360 K to 5 K in the same in-plane external field of 10 Oe. Its magnetisation was then measured (FC measurement) as it was warmed up from 5 K to 360 K, at approximately $2\,\text{Kmin}^{-1}$, in the same external magnetic field. As such, in this instance the sample started with non-zero magnetisation which it retained on cooling and subsequent (measured) heating.

The results of the ZFC-FC study are shown in Fig. 7.11. From this figure it is clear that the ZFC and FC curves do not overlap below a certain temperature. This indicates that at low temperatures the history of the system is important. This was expected since the coercivities of the lattices at 5 K were considerably larger than 10 Oe (see Fig. 7.9) whereas at 293 K they were thought to be lower (see e.g. Fig.

7.8). It was also expected that the temperature at which the ZFC and FC curves joined (T_{join}) would depend on the lattice separation. This was indeed the case. The largest T_{join} was seen for $a = 250\,\text{nm}$ ($\approx 325\,\text{K}$) which is consistent with the surprising observation that this lattice separation has the largest coercivity at 5 K (see Fig. 7.9 (b)). The presence of a joining temperature and its dependence on lattice separation lends further credence to the claim that these nanodiscs are indeed interacting.

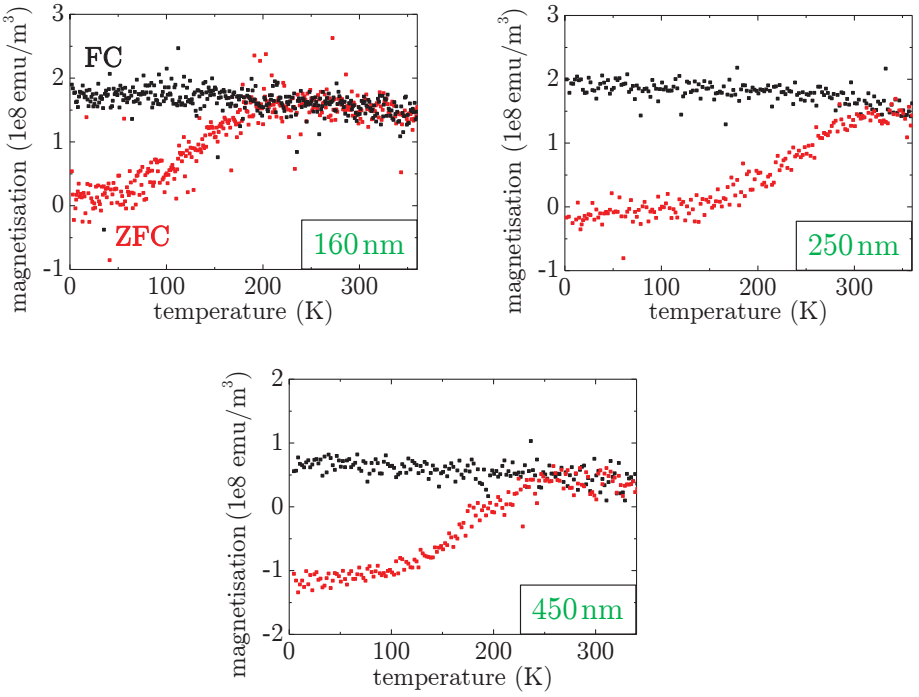

Figure 7.11: Zero field cooled (red) and field cooled (black) measurements for nanodiscs in kagome lattices of $a = 160\,\text{nm}$, $a = 250\,\text{nm}$ and $a = 450\,\text{nm}$ at 10 Oe.

The preliminary magnetometry results shown in this section are promising. The fact that both the lattice separation and geometry changes the M vs. H curves and the fact that the lattice spacing changes the joining temperature in ZFC-FC measurements strongly indicate that dipolar interactions are important in this system. In addition the peak in 5 K coercivity and joining temperature at a lattice separation $a = 250\,\text{nm}$ hints at some interesting physics needing further investigation.

7.4.2 Magnetic Force Microscopy

Magnetic Force Microscopy (MFM) (see Section 3.2.7) was performed in order to probe the magnetisation directions of individual nanodiscs (diameter 80 nm, thickness 16 nm) in Artificial Dipolar 2D-XY. Fig. 7.12 shows the MFM phase shift contrast of nine nanodiscs in the kagome geometry, lattice separation $a = 328$ nm. Here blocks of red and yellow contrast were seen at each disc indicating that the nanodiscs were indeed in single domain states (a vortex state would yield considerable red or yellow contrast at the centre due to its core and minimal contrast elsewhere). However the

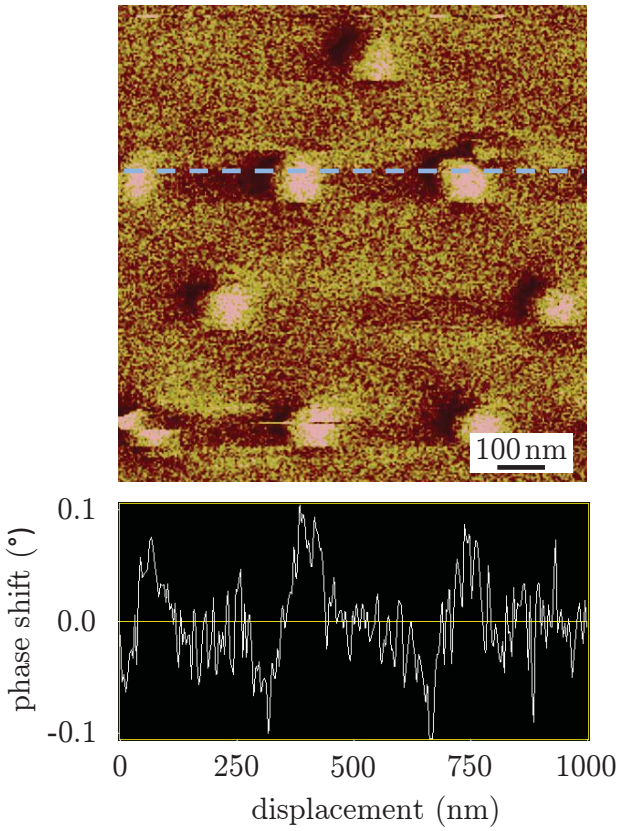

Figure 7.12: Top: Magnetic Force Microscopy phase shift image of nanodiscs (diameter 80 nm, thickness 16 nm) in a kagome geometry, $a = 328$ nm. Red and yellow contrast indicate negative and positive phase shifts respectively. Bottom: phase shift cross section at blue dashed line.

single domain nanodiscs were all aligned along the left-right scan axis. Furthermore when the scan direction was changed, the direction of alignment changed. These

results indicate that, due to the array's low room temperature coercivity (Fig. 7.8 suggests ≈ 3 Oe), the nanodiscs' magnetisation directions were switched as the MFM tip rastered over the sample. In this way, any interesting magnetic states occurring due to dipolar interactions between the nanodiscs were wiped from the sample during scanning. As such, MFM was not a suitable way to image these nanodiscs and a new non-invasive imaging technique was sought.

7.4.3 Lorentz Transmission Electron Microscopy

Kagome Artificial Dipolar 2D-XY arrays comprising nanodiscs of diameter 60 nm and thickness 18 nm were studied via Lorentz Transmission Electron Microscopy (LTEM) (see Section 3.2.6). The expected LTEM contrast of the simulated [18] single domain nanodisc shown in Fig. 7.13 (a) was computed with the MALTS software [64] and is shown in Fig. 7.13 (b). This MALTS simulation indicated that the magnetisation of a single domain nanodisc could be inferred with LTEM by studying the position of a bright white dot.

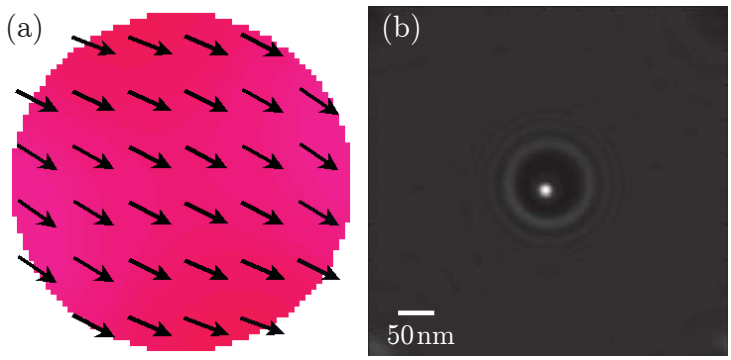

Figure 7.13: (a) micromagnetic simulation [18] of a 60 nm diameter, 20 nm thick permalloy nanodisc supporting a single-domain state, identical to Fig. 7.1 (a). (b) MALTS [64] simulation of the LTEM contrast from the micromagnetic structure shown in (a) performed at an accelerating voltage of 300 kV and defocus of 500 µm.

Experimental LTEM images were taken at $+30°$ and $-30°$ tilts corresponding to in-plane magnetic fields of 46 mT in the $-y$ and $+y$ directions respectively. For both these tilts, defocus series from -1500 µm to $+1500$ µm were taken. During the defocus series the images of the nanodiscs were seen to change in both position

and size. In order to enable direct comparison between different defocus images, the images were aligned with respect to each other using the scaled rotation function in the ImageJ [115] StackReg [116] add on.

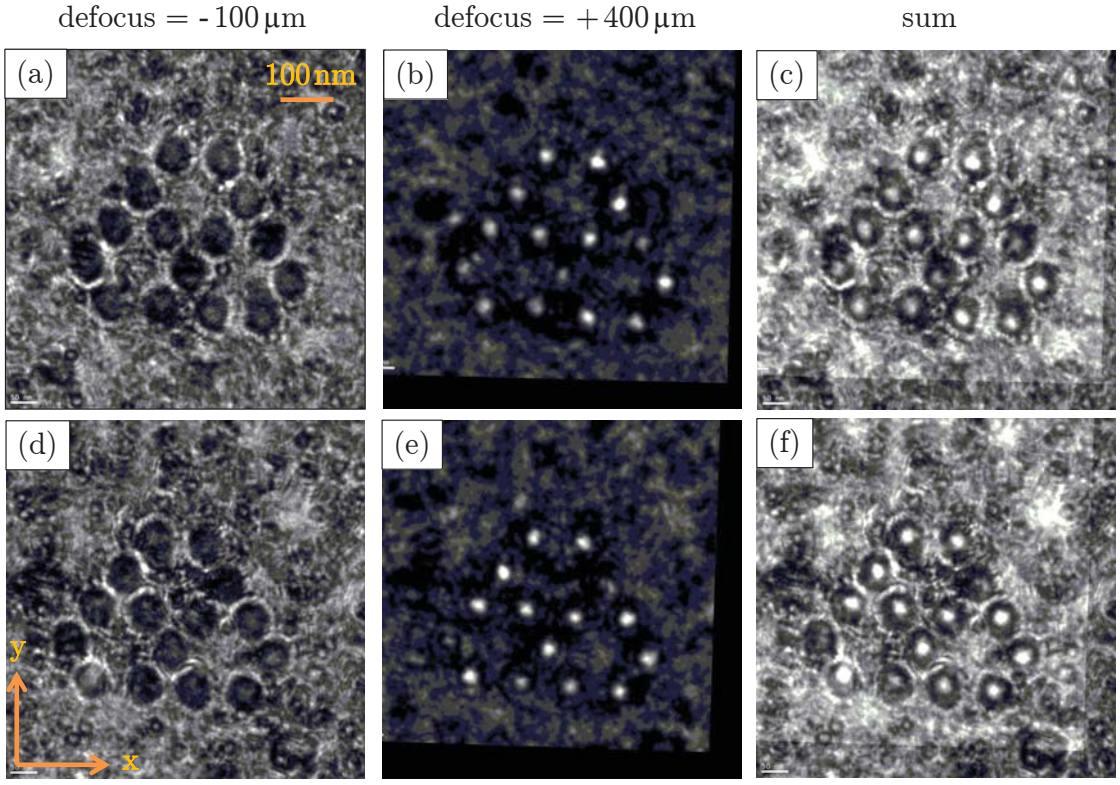

Figure 7.14: Experimental LTEM images of a three hexagon building block of Kagome Artificial Dipolar 2D-XY taken with an accelerating voltage of 300 kV. (a) & (b) were taken at a tilt of +30° and (d) & (e) at a tilt of −30° corresponding to an in-plane magnetic field of 46 mT in the $-y$ and $+y$ directions respectively. (a) & (d) were taken at a defocus of −100 µm and (b) & (c) at a defocus of +400 µm. (c), the sum of (a) & (b) and (f), the sum of (d) & (e) were used to determine the positions of the white dots with respect to the centres of the discs.

Although the experimental LTEM contrast of a three hexagon building block of Kagome Artificial Dipolar 2D-XY matched the simulated single-domain contrast well, it was not possible to discern the positions of the white dots with respect to the centres of the nanodiscs from a single defocus image (e.g. see Fig. 7.14 (b) or (e)). Therefore, for analysis purposes, an image taken at small negative defocus which clearly showed the positions of the discs was overlapped with an image taken at larger

positive defocus which clearly showed the white dots. This is illustrated in Fig. 7.14.

From the overlapped images shown in Fig. 7.14 (c) & (f), the approximate distances between the white dots and the centres of the discs were calculated. The mean distances for both tilt directions are shown in Table 7.3. According to the simulation shown in Fig. 7.13, a saturating field in the $-y$ direction ($+30°$ tilt) should yield a negative x displacement of the white dot from the disc centre and a saturating field in the $+y$ direction ($-30°$ tilt) should yield a positive x displacement of the white dot from the disc centre. The results shown in Table 7.3 display this kind of behaviour. However a larger y displacement was seen for both situations, perhaps due to inaccuracies in the alignment and overlapping method. In addition, the standard deviations for all data sets were large making it impossible to unambiguously determine nanodisc magnetisation directions with this method. As such a more conclusive way to image Artificial Dipolar 2D-XY was sought.

Field (Oe)	Δ**x** μ (σ) (nm)	Δ**y** μ (σ) (nm)
-46 mT	-3.8 (3.3)	-8.4 (5.1)
$+46$ mT	1.5 (4.1)	3.6 (3.1)

Table 7.3: Mean x and y distances between the white dots and their disc centres for the two situations shown in Fig. 7.14. The standard deviations for each case are provided in brackets.

7.4.4 Scanning Transmission X-Ray Microscopy

Scanning Transmission X-Ray Microscopy (see Section 3.2.4) was performed on Artificial Dipolar 2D-XY at Beamline PolLux - X07DA of the Swiss Light Source, Paul Scherrer Institute. Kagome arrays of nanodiscs of diameter 65 nm (measured via Scanning Electron Microscopy, see Fig. 7.15) and thickness 13 nm (measured by Atomic Force Microscopy) were made with four different lattice separations, $a = 224$ nm, $a = 328$ nm, $a = 612$ nm and $a = 1\,\mu$m. Different sized areas ($\approx 90 \times 90\,\mu m^2, \approx 30 \times 30\,\mu m^2, \approx 10 \times 10\,\mu m^2$) of arrays of each of these lattice separations were fabricated in order to investigate the finite size effect. In addition, alignment markers in the form of circles, squares and triangles were fabricated to ease

navigation around the sample.

Figure 7.15: Scanning Electron Microscopy image (taken by Megha Chadha) of nanodiscs in a kagome geometry, $a = 328\,\text{nm}$, on a silicon nitride membrane at a magnification of 28000.

7.4.4.1 Experimental results

The alignment markers (including discs of diameter 20 µm and 5 µm × 5 µm squares) were the largest features on the sample and as such were used for focusing purposes. These markers also produced magnetic contrast (see Fig. 7.16 (a) - (c)). The nanodiscs in Kagome Artificial Dipolar 2D-XY were then brought into focus and left hand and right hand circularly polarised light transmission images were taken. Unfortunately, however, no discernible magnetic contrast was seen. Attempts to enhance the differential absorption were made. Firstly the images were taken using longer dwell times (up to 60 ms) and more data points (up to 250 pts × 250 pts). However problems with drifting and excessive carbon deposition were encountered during these lengthy

scans. Secondly an external magnet was introduced in the sample space. The sample was magnetically saturated under 10 mT along both contrast directions sequentially but any differences in absorption were imperceptible (see Fig. 7.17). This was true at both the nickel (853.7 eV) and iron (708.0 eV) L_3 edges.

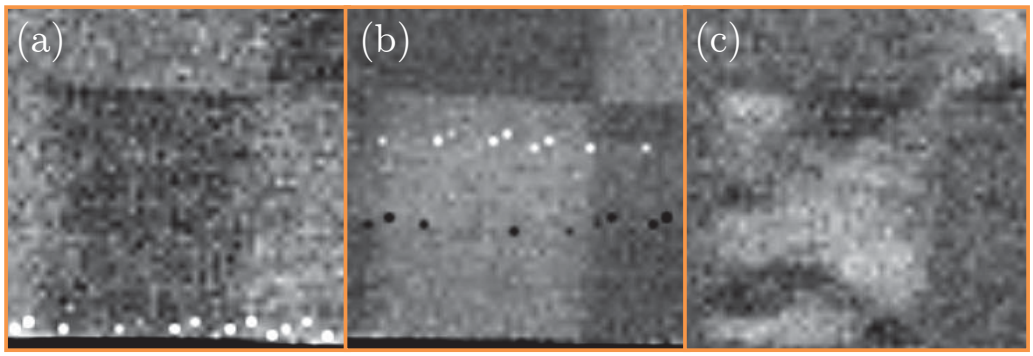

Figure 7.16: STXM differential absorption images at the iron edge for a square alignment marker of dimensions 5 μm × 5 μm after (a) saturation in the positive x direction (b) saturation in the negative x direction and (c) a demagnetisation routine. The scan size was 7 μm × 7 μm, there were 50 pts × 50 pts and the dwell time was 20 ms. The black and white dots are instrumental artefacts.

Analysis of the data suggested that the absorbance of the material was consistent with only 6 nm thick permalloy, not 13 nm. In addition, when the sample was studied under an optical microscope in transmission mode, a transparent brown colour rather than the silvery opaque colour expected for permalloy was seen (see Figure 7.18). From these observations it was understood that the quality of the permalloy was substandard and that perhaps other elements apart from iron and nickel were present. As such, *X-ray Absorption Spectroscopy* was performed at the SLS in order to identify these extra elements. For incident X-ray energies between 390 eV and 1000 eV, however, no unexpected signatures were observed. In addition, Solveig Felton performed detailed elemental analysis of the samples via *Energy Dispersive X-Ray Spectroscopy* at Queen's University Belfast. The chemical composition of the structures was analysed for incident X-ray energies of both 10 keV and 15 keV but again, no unexpected elements were observed.

Since no unexpected elements were found during elemental analysis, a study into the *porosity* or degree of empty space in the sample was made. The deposition rate

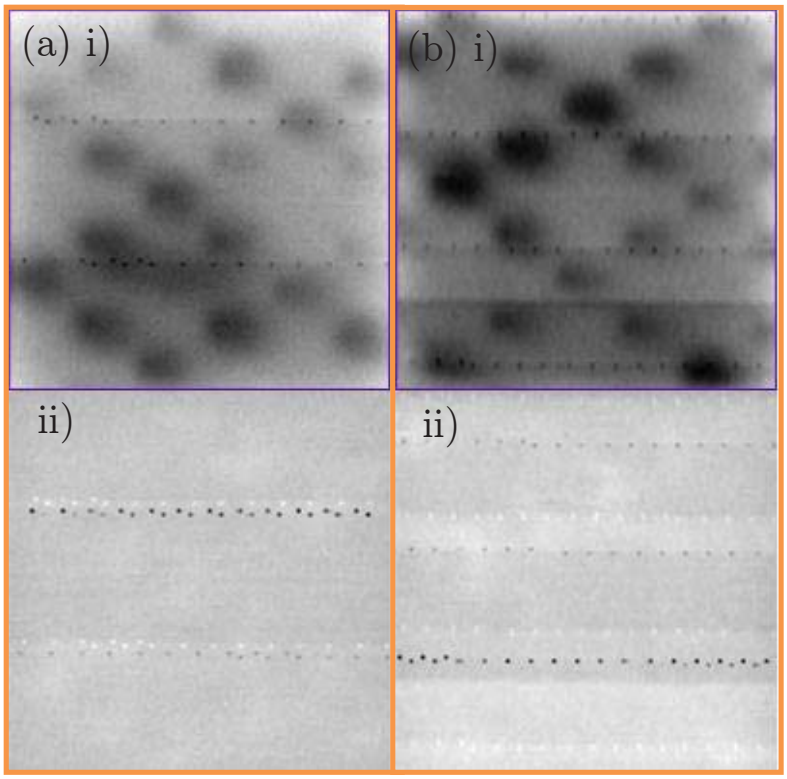

Figure 7.17: (a) i) and (b) i) in focus STXM images of different 1 µm×1 µm areas of the kagome nanodisc array of lattice separation $a = 224\,\text{nm}$. The corresponding differential absorptions ii) at the iron edge (a) after saturation in the negative x direction and (b) after saturation in the positive x direction are shown below. The images were taken with 100 pts × 100 pts and a dwell time of 50 ms. The black and white dots are instrumental artefacts.

used during thermal evaporation for the samples for the SLS STXM experiment was $0.01\,\text{nms}^{-1}$. This yielded a saturation magnetisation of $500\,\text{kAm}^{-1}$, 60% of that expected for permalloy. When, however, the evaporation was performed at a higher rate of $0.16\,\text{nms}^{-1}$, a saturation magnetisation of $652\,\text{kAm}^{-1}$ was achieved, 79% of that expected for permalloy. As such it was understood that the slow deposition rate had led to porous, low quality permalloy nanodiscs with negligibly small differential absorptions. Therefore all future experiments will be performed with a faster deposition rate in order to prevent problems of this nature in the future.

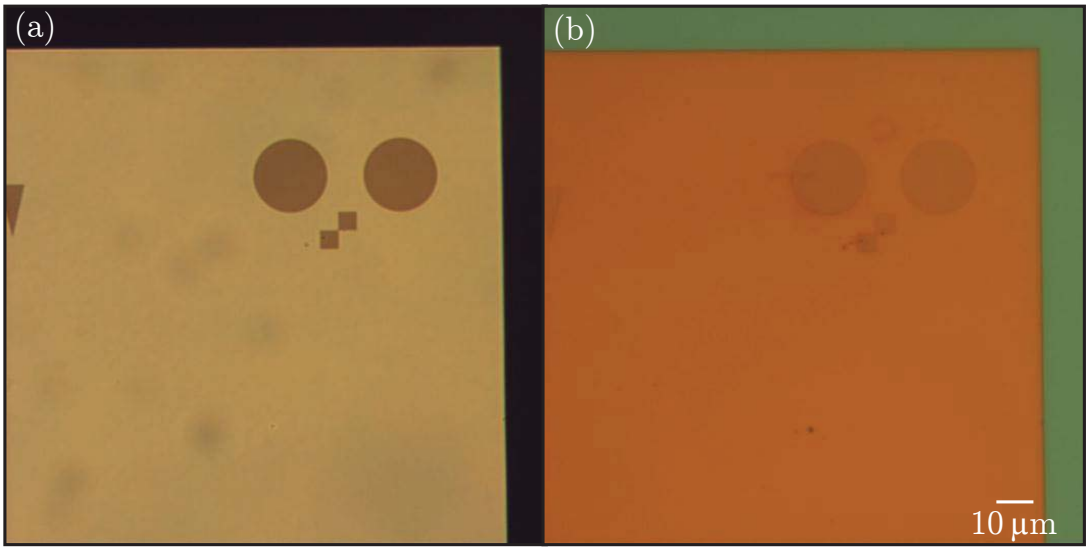

Figure 7.18: Optical Microscope images of alignment markers at the corner of the sample in (a) transmission and (b) reflectance mode. A silvery opaque colour in transmission is typical of permalloy of this thickness.

7.5 Future work

Nominally identical Artificial Dipolar 2D-XY samples will be fabricated and studied in order to check that the surprising magnetometry results described in Section 7.4.1, particularly the peak in 5 K coercivity and joining temperature for a lattice separation $a = 250\,\text{nm}$, are reproducible. In addition, in order to understand better the differences between the field responses of square and kagome lattices, single-spin-flip Metropolis Monte Carlo simulations will be performed on square lattices for comparison with the existing kagome simulations.

Further attempts to elucidate the magnetisations of individual nanodiscs with STXM will be made. A fast deposition rate will be used during thermal evaporation to ensure that the nanodiscs are made of the highest quality permalloy.

7.6 Summary

In this chapter the 2D-XY and Dipolar 2D-XY models have been introduced and concepts such as phase transitions and universality have been discussed. The viability of using an array of single domain nanodiscs, termed Artificial Dipolar 2D-XY, to test Dipolar 2D-XY theories has been explored. Results from preliminary single-spin-flip Metropolis Monte Carlo simulations have been shown. In addition, results from magnetometry and preliminary imaging experiments on Artificial Dipolar 2D-XY have been presented. The magnetometry data provided convincing evidence that the nanodiscs were indeed interacting. The origin of an interesting peak in 5 K coercivity and joining temperature seen for lattice separation $a = 250\,\text{nm}$, however, is not yet known and requires further investigation. Although a comparison of Artificial Dipolar 2D-XY and Artificial Spin Ice's reversal behaviour has not yet been possible since imaging attempts of Artificial Dipolar 2D-XY have so far been unsuccessful, this remains one of the main long term goals for this work.

CHAPTER 8 : CONCLUSION AND FUTURE WORK

In this thesis, the behaviour of the magnetically frustrated nanostructures Artificial Spin Ice and Artificial Dipolar 2D-XY has been investigated. A summary of the key outcomes from this investigation is given below and ideas for future work are detailed.

8.1 Key output

A new software called *Micromagnetic Analysis to Lorentz TEM Simulation* (MALTS) was developed which, when used in conjunction with a micromagnetic solver, simulates the Lorentz Transmission Electron Microscopy (LTEM) contrast of magnetic structures of any shape and size. In **Chapter 4**, MALTS's computational methodology, functionality and availability were discussed in detail. In addition, good agreement between MALTS's output with both experimental images and simulated LTEM contrast from other groups was demonstrated. MALTS was subsequently used in Chapters 6 & 7 for predicting and analysing LTEM contrast from nanobars with ellipsoidal holes and single domain nanodiscs respectively.

8.2 Key results and future work

During the study of field-driven domain wall trajectories in Artificial Spin Ice, two key results were obtained. These were presented and discussed in **Chapter 5**. The first key result was that domain walls in the transverse domain wall regime can execute non-random walks. In light of micromagnetic simulations, this result was explained in terms of the domain wall's chirality dictating its path but a potential loss of chiral information between decision points due to Walker Breakdown. The second key result was that domain walls in the vortex domain wall regime can execute random walks

despite predictions of complete selectivity. This result was though to arise due to Walker Breakdown and complex variations in domain wall micromagnetic structure at high driving fields. In the next stage of this investigation into domain wall propagation paths in Artificial Spin Ice an attempt to increase the selectivity in the transverse domain wall regime by decreasing the nanobar lengths will be made. In addition, an attempt to witness selective behaviour in the vortex domain wall regime will be made by studying reversal at lower external driving fields. This will be achieved by making nanobars thinner and wider yielding lower coercivities.

In an attempt to control the chirality of transverse domain walls injected into Artificial Spin Ice, the functionality of triangular injection pads was studied. Although preliminary experimental data of injection into an Artificial Spin Ice vertex was inconclusive, micromagnetic simulations strongly suggest that the chirality of a domain wall injected from a triangular injection pad is determined by the pad's dimensions and orientation. These simulations are presented and analysed in the first half of **Chapter 6**. In order to verify the functionality of triangular injection pads in the future, a notch filter method will be employed in which the injected domain wall is trapped and subsequently depinned at a field dependent on its chirality. An imaging technique or MOKE will be used in this investigation.

In an attempt to measure and control a vortex domain wall's chirality, the functionality of ellipsoidal holes in nanobars was studied. Micromagnetic simulations suggested that ellipsoidal holes are highly versatile and may be used for domain wall pinning, chirality and polarity readout, chirality changing, setting and randomising. These simulations are presented in the second half of **Chapter 6**. In order to verify the functionality of these ellipsoidal holes, these structures must be realised experimentally. As such, the next stage in this investigation is to develop an effective recipe to fabricate nanobars with ellipsoidal holes. Once this has been achieved, the nanobars' coercivities may be studied with a technique such as MOKE and the domain walls' chiralities may be imaged with a technique such as LTEM.

In order to verify Dipolar 2D-XY theories, the feasibility of realising Artificial Dipolar 2D-XY with single domain nanodiscs in a kagome array was explored. Single domain nanodiscs were thought to behave approximately as Dipolar-XY macrospins

so long as they were separated sufficiently and were made of a material with low magnetocrystalline anisotropy such as permalloy. Preliminary energy versus temperature and magnetisation versus field single-spin-flip Metropolis Monte Carlo simulations for dipoles on a kagome lattice were performed. In addition, bulk magnetometry data was collected which demonstrated that the nanodiscs do indeed interact and that there is an interesting and so far unexplained peak in 5 K coercivity and joining temperature at a lattice separation of $a = 250\,\text{nm}$. A full discussion of this work on Artificial Dipolar 2D-XY is provided in **Chapter 7**. The next stages in this investigation are to check the reproducibility of the data and to reattempt to resolve the magnetisations of individual nanodiscs with an imaging technique. A move to simulating the behaviour of single domain nanodiscs in a square lattice would also be instructive, given that most of the Dipolar 2D-XY theory addresses this geometry and intriguing differences between field responses of square and kagome lattices were observed.

REFERENCES

[1] M. N. Baibich, J. M. Broto, A. Fert, F. N. Vandau, F. Pertoff, P. Eitenne, G. Creuzet, A. Friederich, and J. Chazelas. Giant Magnetoresistance of (001)Fe/(001)Cr Magnetic Superlattices. *PHYSICAL REVIEW LETTERS*, 61(21):2472–2475, 1988.

[2] G. Binasch, P. Grunberg, F. Saurenbach, and W. Zinn. Enhanced magnetoresistance in layered magnetic structures with antiferromagnetic interlayer exchange. *PHYSICAL REVIEW B*, 39(7):4828–4830, 1989.

[3] C. Ross. Patterned magnetic recording media. *ANNUAL REVIEW OF MATERIALS RESEARCH*, 31:203–235, 2001.

[4] Y. Qi, T. Brintlinger, and J. Cumings. Direct observation of the ice rule in an artificial kagome spin ice. *PHYSICAL REVIEW B*, 77(9), 2008.

[5] S. Ladak, D. E. Read, G. K. Perkins, L. F. Cohen, and W. R. Branford. Direct observation of magnetic monopole defects in an artificial spin-ice system. *NATURE PHYSICS*, 6(5):359–363, 2010.

[6] W. R. Branford, S. Ladak, D. E. Read, K. Zeissler, and L. F. Cohen. Emerging Chirality in Artificial Spin Ice. *SCIENCE*, 335(6076):1597–1600, 2012.

[7] S. T. Bramwell and P. C. W. Holdsworth. Magnetization and universal subcritical behavior in 2-dimensional XY magnets. *JOURNAL OF PHYSICS-CONDENSED MATTER*, 5(4):L53–L59, 1993.

[8] L. A. S. Mol and B. V. Costa. Phase transition in the two-dimensional dipolar planar rotator model. *JOURNAL OF PHYSICS-CONDENSED MATTER*, 22(4), 2010.

[9] P. G. Maier and F. Schwabl. Ferromagnetic ordering in the two-dimensional dipolar XY model. *PHYSICAL REVIEW B*, 70(13), 2004.

[10] S. K. Baek, P. Minnhagen, and B. J. Kim. Kosterlitz-Thouless transition of magnetic dipoles on the two-dimensional plane. *PHYSICAL REVIEW B*, 83(18), 2011.

[11] Stephen Blundell. *Magnetism in Condensed Matter*. Oxford University Press, 2008.

[12] J. Michael. D. Coey. *Magnetism and Magnetic Materials*. Cambridge, 2010.

[13] David Jiles. *Introduction to Magnetism and Magnetic Materials*. Chapman and Hall, 1998.

[14] Roy Carey and Evan David Isaac. *Magnetic domains and techniques for their observation*. The English Universities Press Limited, 1966.

[15] Sóshin Chikazumi. *Physics of Ferromagnetism*. Oxford University Press, 2009.

[16] Y. Nakatani, A. Thiaville, and J. Miltat. Head-to-head domain walls in soft nano-strips: a refined phase diagram. *JOURNAL OF MAGNETISM AND MAGNETIC MATERIALS*, 290(Part 1, SI):750–753, 2005.

[17] R. D. McMichael and M. J. Donahue. Head to head domain wall structures in thin magnetic strips. *IEEE TRANSACTIONS ON MAGNETICS*, 33(5, Part 2):4167–4169, 1997.

[18] M. J. Donahue and D. G. Porter. *OOMMF User's Guide, Version 1.0*. Interagency Report NISTIR 6376, National Institute of Standards and Technology, Gaithersburg, MD (Sept 1999).

[19] A. Thiaville. Coherent rotation of magnetization in three dimensions: A geometrical approach. *PHYSICAL REVIEW B*, 61(18):12221–12232, 2000.

[20] N. L. Schryer and L. R. Walker. Motion of 180 degrees domain-walls in uniform DC magnetic-fields. *JOURNAL OF APPLIED PHYSICS*, 45(12):5406–5421, 1974.

[21] C. C. Faulkner, M. D. Cooke, D. A. Allwood, D. Petit, D. Atkinson, and R. P. Cowburn. Artificial domain wall nanotraps in Ni81Fe19 wires. *JOURNAL OF APPLIED PHYSICS*, 95(11, 2):6717–6719, 2004.

[22] D. Petit, A.-V. Jausovec, D. Read, and R. P. Cowburn. Domain wall pinning and potential landscapes created by constrictions and protrusions in ferromagnetic nanowires. *JOURNAL OF APPLIED PHYSICS*, 103(11), 2008.

[23] A. Himeno, T. Ono, S. Nasu, K. Shigeto, K. Mibu, and T. Shinjo. Dynamics of a magnetic domain wall in magnetic wires with an artificial neck. *JOURNAL OF APPLIED PHYSICS*, 93(10, 3):8430–8432, 2003.

[24] L. K. Bogart, D. Atkinson, K. O'Shea, D. McGrouther, and S. McVitie. Dependence of domain wall pinning potential landscapes on domain wall chirality and pinning site geometry in planar nanowires. *PHYSICAL REVIEW B*, 79(5), 2009.

[25] D. S. Eastwood, L. K. Bogart, and D. Atkinson. Scaling Behaviour of Chirality Dependent Domain Wall Pinning in Planar Nanowires. *ACTA PHYSICA POLONICA A*, 118(5):719–722, 2010.

[26] L. K. Bogart, D. S. Eastwood, and D. Atkinson. The effect of geometrical confinement and chirality on domain wall pinning behavior in planar nanowires. *JOURNAL OF APPLIED PHYSICS*, 104(3), 2008.

[27] D. S. Eastwood, J. A. King, L. K. Bogart, H. Cramman, and D. Atkinson. Chirality-dependent domain wall pinning in a multinotched planar nanowire and chirality preservation using transverse magnetic fields. *JOURNAL OF APPLIED PHYSICS*, 109(1), 2011.

[28] G. W. Elmen. Magnetic alloys of iron, nickel and cobalt. *BELL SYSTEM TECHNICAL JOURNAL*, 15 (1):113–135, 1936.

[29] H. D. Arnold and G. W. Elmen. Permalloy, a new magnetic material of very high permeability. *BELL SYSTEM TECHNICAL JOURNAL*, 2 (3):101–111, 1923.

[30] S. T. Bramwell and M. J. P. Gingras. Spin ice state in frustrated magnetic pyrochlore materials. *SCIENCE*, 294(5546):1495–1501, 2001.

[31] A. P. Ramirez, A. Hayashi, R. J. Cava, R. Siddharthan, and B. S. Shastry. Zero-point entropy in 'spin ice'. *NATURE*, 399(6734):333–335, 1999.

[32] C. Castelnovo, R. Moessner, and S. L. Sondhi. Magnetic monopoles in spin ice. *NATURE*, 451(7174):42–45, 2008.

[33] S. T. Bramwell, S. R. Giblin, S. Calder, R. Aldus, D. Prabhakaran, and T. Fennell. Measurement of the charge and current of magnetic monopoles in spin ice. *NATURE*, 461(7266):956–U211, 2009.

[34] T. Fennell, P. P. Deen, A. R. Wildes, K. Schmalzl, D. Prabhakaran, A. T. Boothroyd, R. J. Aldus, D. F. McMorrow, and S. T. Bramwell. Magnetic Coulomb Phase in the Spin Ice Ho2Ti2O7. *SCIENCE*, 326(5951):415–417, 2009.

[35] D. J. P. Morris, D. A. Tennant, S. A. Grigera, B. Klemke, C. Castelnovo, R. Moessner, C. Czternasty, M. Meissner, K. C. Rule, J. U. Hoffmann, K. Kiefer, S. Gerischer, D. Slobinsky, and R. S. Perry. Dirac Strings and Magnetic Monopoles in the Spin Ice Dy2Ti2O7. *SCIENCE*, 326(5951):411–414, 2009.

[36] O. Tchernyshyov. MAGNETIC MONOPOLES No longer on thin ice. *NATURE PHYSICS*, 6(5):323–324, 2010.

[37] R. F. Wang, C. Nisoli, R. S. Freitas, J. Li, W. McConville, B. J. Cooley, M. S. Lund, N. Samarth, C. Leighton, V. H. Crespi, and P. Schiffer. Artificial 'spin ice' in a geometrically frustrated lattice of nanoscale ferromagnetic islands. *NATURE*, 439(7074):303–306, 2006.

[38] J. P. Morgan, A. Stein, S. Langridge, and C. H. Marrows. Thermal ground-state ordering and elementary excitations in artificial magnetic square ice. *NATURE PHYSICS*, 7(1):75–79, 2011.

[39] N. Rougemaille, F. Montaigne, B. Canals, A. Duluard, D. Lacour, M. Hehn, R. Belkhou, O. Fruchart, S. El Moussaoui, A. Bendounan, and F. Maccherozzi. Artificial Kagome Arrays of Nanomagnets: A Frozen Dipolar Spin Ice. *PHYSICAL REVIEW LETTERS*, 106(5), 2011.

[40] G. Moeller and R. Moessner. Magnetic multipole analysis of kagome and artificial spin-ice dipolar arrays. *PHYSICAL REVIEW B*, 80(14), 2009.

[41] G.-W. Chern, P. Mellado, and O. Tchernyshyov. Two-Stage Ordering of Spins in Dipolar Spin Ice on the Kagome Lattice. *PHYSICAL REVIEW LETTERS*, 106(20), 2011.

[42] E. Mengotti, L. J. Heyderman, A. Fraile Rodriguez, A. Bisig, L. Le Guyader, F. Nolting, and H. B. Braun. Building blocks of an artificial kagome spin ice: Photoemission electron microscopy of arrays of ferromagnetic islands. *PHYSICAL REVIEW B*, 78(14), 2008.

[43] Y. Shen, O. Petrova, P. Mellado, S. Daunheimer, J. Cumings, and O. Tchernyshyov. Dynamics of artificial spin ice: a continuous honeycomb network. *NEW JOURNAL OF PHYSICS*, 14, 2012.

[44] P. Mellado, O. Petrova, Y. Shen, and O. Tchernyshyov. Dynamics of Magnetic Charges in Artificial Spin Ice. *PHYSICAL REVIEW LETTERS*, 105(18), 2010.

[45] William Fuller Brown. *Micromagnetics*. New York ; London : Interscience, 1963.

[46] A. C. F. Hoole, M. E. Welland, and A. N. Broers. Negative PMMA as a high-resolution resist - the limits and possibilities. *SEMICONDUCTOR SCIENCE AND TECHNOLOGY*, 12(9):1166–1170, 1997.

[47] I. Ziler, J. E. F. Frost, V. Chabasseur-Molyneux, C. J. B. Ford, and M. Pepper. Crosslinked PMMA as a high-resolution negative resist for electron beam lithography and applications for physics of low-dimensional structures. *SEMICONDUCTOR SCIENCE AND TECHNOLOGY*, 11(8):1235–1238, 1996.

[48] *Quantum Design, Physical Property Measurement System, Vibrating Sample Magnetometer (VSM) Option, User's Manual Feb 2008, Part Number 1096-100, A3.*

[49] *NanoMOKE^{TM}2 Manual, Durham Magneto Optics Ltd.*

[50] T. Tyliszczak, T. Warwick, A. L. D. Kilcoyne, S. Fakra, D. K. Shuh, T. H. Yoon, G. E. Brown, S. Andrews, V. Chernbrolu, J. Strachan, and Y. Acremann. Soft X-ray scanning transmission microscope working in an extended energy range at the advanced light source. In *SYNCHROTRON RADIATION INSTRUMENTATION*, 2004.

[51] T. Warwick, K. Franck, J. B. Kortright, G. Meigs, M. Moronne, S. Myneni, E. Rotenberg, S. Seal, W. F. Steele, H. Ade, A. Garcia, S. Cerasari, J. Delinger, S. Hayakawa, A. P. Hitchcock, T. Tyliszczak, J. Kikuma, E. G. Rightor, H. J. Shin, and B. P. Tonner. A scanning transmission x-ray microscope for materials science spectromicroscopy at the advanced light source. *REVIEW OF SCIENTIFIC INSTRUMENTS*, 69(8):2964–2973, 1998.

[52] A. Locatelli and E. Bauer. Recent advances in chemical and magnetic imaging of surfaces and interfaces by XPEEM. *JOURNAL OF PHYSICS-CONDENSED MATTER*, 20(9), 2008.

[53] Wolfgang Kuch. Magnetic imaging. In *Magnetism: A Synchrotron Radiation Approach*, 2006.

[54] David B. Williams and C. Barry Carter. *Transmission Electron Microscopy.* Springer, 2009.

[55] J. N. Chapman. The investigation of magnetic domain-structures in thin foils by electron-microscopy. *JOURNAL OF PHYSICS D-APPLIED PHYSICS*, 17(4):623–647, 1984.

[56] *Dimension 3100 Series, Scanning Probe Microscope, Instruction Manual, Digital Instruments.*

[57] Peter Eaton and Paul West. *Atomic Force Microscopy.* Oxford University Press, 2010.

[58] J. Fidler and T. Schrefl. Micromagnetic modelling - the current state of the art. *JOURNAL OF PHYSICS D-APPLIED PHYSICS*, 33(15):R135–R156, 2000.

[59] University of Hamburg SPM-Group. Implementation of temperature in micromagnetic simulations, 2002.

[60] M. J. Donahue and R. D. McMichael. Micromagnetics on curved geometries using rectangular cells: Error correction and analysis. *IEEE TRANSACTIONS ON MAGNETICS*, 43(6):2878–2880, 2007.

[61] S. Ingvarsson, L. Ritchie, X. Y. Liu, G. Xiao, J. C. Slonczewski, P. L. Trouilloud, and R. H. Koch. Role of electron scattering in the magnetization relaxation of thin Ni81Fe19 films. *PHYSICAL REVIEW B*, 66(21), 2002.

[62] H. W. Schumacher, S. Serrano-Guisan, K. Rott, and G. Reiss. Ultrafast magnetization dynamics probed by anisotropic magnetoresistance. *APPLIED PHYSICS LETTERS*, 90(4), 2007.

[63] A. Vansteenkiste and B. Van de Wiele. MuMax: A new high-performance micromagnetic simulation tool. *JOURNAL OF MAGNETISM AND MAGNETIC MATERIALS*, 323(21):2585–2591, 2011.

[64] S. K. Walton, K. Zeissler, W. R. Branford, and S. Felton. MALTS: A tool to simulate lorentz transmission electron microscopy from micromagnetic simulations. *IEEE TRANSACTIONS ON MAGNETICS*, 49(8), 2013.

[65] J. N. Chapman and M. R. Scheinfein. Transmission electron microscopies of magnetic microstructures. *JOURNAL OF MAGNETISM AND MAGNETIC MATERIALS*, 200(1-3):729–740, 1999.

[66] M. E. Hale, H. W. Fuller, and H. Rubinstein. Magnetic domain observation by electron microscopy. *JOURNAL OF APPLIED PHYSICS*, 30:789–791, 1959.

[67] A. Kundrotaite, J. N. Chapman, and M. Rahman. Lorentz microscopy analysis of arrays of rhombic elements. *IEEE TRANSACTIONS ON MAGNETICS*, 39(5, Part 2):2672–2674, 2003.

[68] Yi Qi. *Artificial Kagome Spin Ice*. PhD thesis, University of Maryland, 2008.

[69] S. McVitie and M. Cushley. Quantitative Fresnel Lorentz microscopy and the transport of intensity equation. *ULTRAMICROSCOPY*, 106(4-5):423–431, 2006.

[70] A. Masseboeuf, C. Gatel, P. Bayle-Guillemaud, A. Marty, and J.-C. Toussaint. Lorentz microscopy mapping for domain wall structure study in L1(0) FePd thin films. *ULTRAMICROSCOPY*, 110(1):20–25, 2009.

[71] S. P. Venkateswaran, N. T. Nuhfer, and M. De Graef. Anti-phase boundaries and magnetic domain structures in Ni2MnGa-type Heusler alloys. *ACTA MATERIALIA*, 55(8):2621–2636, 2007.

[72] C. Phatak, A. K. Petford-Long, and O. Heinonen. Direct Observation of Unconventional Topological Spin Structure in Coupled Magnetic Discs. *PHYSICAL REVIEW LETTERS*, 108(6), 2012.

[73] C. Phatak, M. Tanase, A. K. Petford-Long, and M. De Graef. Determination of magnetic vortex polarity from a single Lorentz Fresnel image. *ULTRAMICROSCOPY*, 109(3):264–267, 2009.

[74] D.-T. Ngo and S. McVitie. Visualization of vortex core polarity in NiFe nanodots by tilted Fresnel images. *ULTRAMICROSCOPY*, 111(8):1276–1285, 2011.

[75] N. Agarwal, H. Wang, D. J. Smith, and M. R. McCartney. Remanent states and magnetization reversal for nanopatterned co elements. *IEEE TRANSACTIONS ON MAGNETICS*, 42(10):2414–2416, 2006.

[76] A. Kovács, A. Kohn, J. Dean, T. Schrefl, A. Zeltser, and M. J. Carey. Reversal Mechanism of Exchange-Biased CoFeB/IrMn Bilayers Observed by Lorentz Electron Microscopy. *IEEE TRANSACTIONS ON MAGNETICS*, 45(10, SI):3873–3876, 2009.

[77] T. Kasama, R. J. Harrison, N. S. Church, M. Nagao, J. M. Feinberg, and R. E. Dunin-Borkowski. Ferrimagnetic/ferroelastic domain interactions in magnetite below the Verwey transition. Part I: electron holography and Lorentz microscopy. *PHASE TRANSITIONS*, 86(1, SI):67–87, 2013.

[78] J. F. J. Bryson, T. Kasama, R. E. Dunin-Borkowski, and R. J. Harrison. Ferrimagnetic/ferroelastic domain interactions in magnetite below the Verwey transition: Part II. Micromagnetic and image simulations. *PHASE TRANSITIONS*, 86(1, SI):88–102, 2013.

[79] T. Haug, S. Otto, M. Schneider, and J. Zweck. Computer simulation of Lorentz electron micrographs of thin magnetic particles. *ULTRAMICROSCOPY*, 96(2):201–206, 2003.

[80] Y. Aharonov and D. Bohm. Significance of electromagnetic potentials in the quantum theory. *PHYS. REV. SECOND SERIES*, 115:485–491, 1959.

[81] M. Beleggia, M. A. Schofield, Y. Zhu, M. Malac, Z. Liu, and M. Freeman. Quantitative study of magnetic field distribution by electron holography and micromagnetic simulations. *APPLIED PHYSICS LETTERS*, 83(7):1435–1437, 2003.

[82] S. Wang, D. Wei, and K.-Z. Gao. Limits of Discretization in Computational Micromagnetics. *IEEE TRANSACTIONS ON MAGNETICS*, 47(10):3813–3816, 2011.

[83] V. V. Volkov, Y. Zhu, and M. De Graef. A new symmetrized solution for phase retrieval using the transport of intensity equation. *MICRON*, 33(5):411–416, 2002.

[84] K. Zeissler, S. K. Walton, S. Ladak, D. E. Read, T. Tyliszczak, L. F. Cohen, and W. R. Branford. The non-random walk of chiral magnetic charge carriers in artificial spin ice. *SCIENTIFIC REPORTS*, 3, 2013.

[85] A. Pushp, T. Phung, C. Rettner, B. P. Hughes, S.-H. Yang, L. Thomas, and S. S. P. Parkin. Domain wall trajectory determined by its fractional topological edge defects. *NATURE PHYSICS*, 9(8):505–511, 2013.

[86] M. Feser, M. Carlucci-Dayton, C. Jacobsen, J. Kirz, U. Neuhausler, G. Smith, and B. Yu. Applications and instrumentation advances with the Stony Brook scanning transmission X-ray microscope. In *X-RAY MICROFOCUSING: APPLICATIONS AND TECHNIQUES*, 1998.

[87] M. Heumann, T. Uhlig, and J. Zweck. True single domain and configuration-assisted switching of submicron permalloy dots observed by electron holography. *PHYSICAL REVIEW LETTERS*, 94(7), 2005.

[88] M. Hayashi, L. Thomas, C. Rettner, R. Moriya, and S. S. P. Parkin. Direct observation of the coherent precession of magnetic domain walls propagating along permalloy nanowires. *NATURE PHYSICS*, 3(1):21–25, 2007.

[89] J. Yang, C. Nistor, G. S. D. Beach, and J. L. Erskine. Magnetic domain-wall velocity oscillations in permalloy nanowires. *PHYSICAL REVIEW B*, 77(1), 2008.

[90] J.-Y. Lee, K.-S. Lee, S. Choi, K. Y. Guslienko, and S.-K. Kim. Dynamic transformations of the internal structure of a moving domain wall in magnetic nanostripes. *PHYSICAL REVIEW B*, 76(18), 2007.

[91] M. T. Bryan, T. Schrefl, and D. A. Allwood. Dependence of Transverse Domain Wall Dynamics on Permalloy Nanowire Dimensions. *IEEE TRANSACTIONS ON MAGNETICS*, 46(5):1135–1138, 2010.

[92] E. R. Lewis, D. Petit, A. V. Jausovec, L. O'Brien, D. E. Read, H. T. Zeng, and R. P. Cowburn. Measuring Domain Wall Fidelity Lengths Using a Chirality Filter. *PHYSICAL REVIEW LETTERS*, 102(5), 2009.

[93] Y. Nakatani, A. Thiaville, and J. Miltat. Faster magnetic walls in rough wires. *NATURE MATERIALS*, 2(8):521–523, 2003.

[94] O. A. Tretiakov, D. Clarke, Gia-Wei Chern, Ya. B. Bazaliy, and O. Tchernyshyov. Dynamics of domain walls in magnetic nanostrips. *PHYSICAL REVIEW LETTERS*, 100(12), 2008.

[95] Jusang Yang. *Study of Static Spin Distributions and Dynamics of Magnetic Domain Walls in Soft Magnetic Nanostructures*. PhD thesis, The University of Texas Austin, 2013.

[96] K. Shigeto, T. Shinjo, and T. Ono. Injection of a magnetic domain wall into a submicron magnetic wire. *APPLIED PHYSICS LETTERS*, 75(18):2815–2817, 1999.

[97] R. P. Cowburn, D. A. Allwood, G. Xiong, and M. D. Cooke. Domain wall injection and propagation in planar Permalloy nanowires. *JOURNAL OF APPLIED PHYSICS*, 91(10, 2):6949–6951, 2002.

[98] D. McGrouther, S. McVitie, J. N. Chapman, and A. Gentils. Controlled domain wall injection into ferromagnetic nanowires from an optimized pad geometry. *APPLIED PHYSICS LETTERS*, 91(2), 2007.

[99] M.-F. Lai and C.-N. Liao. Size dependence of C and S states in circular and square permalloy dots. *JOURNAL OF APPLIED PHYSICS*, 103(7), 2008.

[100] D. K. Koltsov, R. P. Cowburn, and M. E. Welland. Micromagnetics of ferromagnetic equilateral triangular prisms. *JOURNAL OF APPLIED PHYSICS*, 88(9):5315–5317, 2000.

[101] T. H. P. Chang. Proximity effect in electron-beam lithography. *JOURNAL OF VACUUM SCIENCE & TECHNOLOGY*, 12(6):1271–1275, 1975.

[102] S. T. Bramwell, P. C. W. Holdsworth, and J. F. Pinton. Universality of rare fluctuations in turbulence and critical phenomena. *NATURE*, 396(6711):552–554, 1998.

[103] J. M. Kosterlitz and D. J. Thouless. Ordering, metastability and phase-transitions in 2 dimensional systems. *JOURNAL OF PHYSICS C-SOLID STATE PHYSICS*, 6(7):1181–1203, 1973.

[104] V. L. Berezinskii. Destruction of long-range order in one-dimensional and 2-dimensional systems having a continuous symmetry group 1 - classical systems. *SOVIET PHYSICS JETP-USSR*, 32(3):493–500, 1971.

[105] A. Taroni, S. T. Bramwell, and P. C. W. Holdsworth. Universal window for two-dimensional critical exponents. *JOURNAL OF PHYSICS-CONDENSED MATTER*, 20(27), 2008.

[106] C. A. F. Vaz, J. A. C. Bland, and G. Lauhoff. Magnetism in ultrathin film structures. *REPORTS ON PROGRESS IN PHYSICS*, 71(5), 2008.

[107] R. P. Cowburn. Property variation with shape in magnetic nanoelements. *JOURNAL OF PHYSICS D-APPLIED PHYSICS*, 33(1):R1–R16, 2000.

[108] G. S. Abo, Y.-K. Hong, J. Park, J. Lee, W. Lee, and B.-C. Choi. Definition of Magnetic Exchange Length. *IEEE TRANSACTIONS ON MAGNETICS*, 49(8, 2):4937–4939, 2013.

[109] N. Mikuszeit, E. Y. Vedmedenko, R. Wiesendanger, and H. P. Oepen. Multipole moments of in-plane magnetized disks. *JOURNAL OF APPLIED PHYSICS*, 97(10, 3), 2005.

[110] N. Mikuszeit, E. Y. Vedmedenko, and H. P. Oepen. Multipole interaction of polarized single-domain particles. *JOURNAL OF PHYSICS-CONDENSED MATTER*, 16(49):9037–9045, 2004.

[111] E. Y. Vedmedenko and R. Wiesendanger. Modulated multipolar structures in magnetic arrays. *PHILOSOPHICAL MAGAZINE*, 88(18-20):2683–2697, 2008.

[112] N. Metropolis, A. W. Rosenbluth, M. N. Rosenbluth, and A. H. Teller. Equations of state calculations by fast computing machines. *THE JOURNAL OF CHEMICAL PHYSICS*, 21, 1953.

[113] S. Chib and E. Greenberg. Understanding the Metropolis-Hastings Algorithm. *AMERICAN STATISTICIAN*, 49(4):327–335, 1995.

[114] A. Gelman and D. B. Rubin. Inference from iterative simulation using multiple sequences. *STATISTICAL SCIENCE*, 7:457–511, 1992.

[115] W. S. Rasband. Imagej. *U. S. National Institutes of Health, Bethesda, Maryland, USA*, http://imagej.nih.gov/ij/, 1997-2012.

[116] P. Thevenaz, U. E. Ruttimann, and M. Unser. A pyramid approach to subpixel registration based on intensity. *IEEE TRANSACTIONS ON IMAGE PROCESSING*, 7(1):27–41, 1998.

Appendices

APPENDIX A : ACRONYM SUMMARY

AFM: Atomic Force Microscopy

ALS: Advanced Light Source

ASI: Artificial Spin Ice

DW: Domain Wall

FC: Field Cooled

HPC: High Performance Computing

IPA: Isopropanol

LTEM: Lorentz Transmission Electron Microscopy

MALTS: Micromagnetic Analysis to Lorentz TEM Simulation

MCD: Magnetic Circular Dichroism

MFM: Magnetic Force Microscopy

MOKE: Magneto Optic Kerr Effect Lensing

OOMMF: Object Oriented Micromagnetic Framework

PEEM: Photo Electron Emission Microscopy

SEM: Scanning Electron Microscopy

SLS: Swiss Light Source

SQUID: Superconducting Quantum Interference Device

STXM: Scanning Transmission X-Ray Microscopy

TEM: Transmission Electron Microscopy

VSM: Vibrating Sample Magnetometry

ZFC: Zero Field Cooled

APPENDIX B : MICROMAGNETIC SIMULATION MAGNETISATION CONTRAST AND AXES

The key to the contrast in micromagnetic simulations in Chapters 2, 5, 6 & 7 is given in Fig. B.1 (a), and the key to the contrast in Chapter 4 is given in Fig. B.1 (b). Unless otherwise specified, the x and y axes of all figures in this thesis, micromagnetic simulations or otherwise, are oriented according to Fig. B.1 (c).

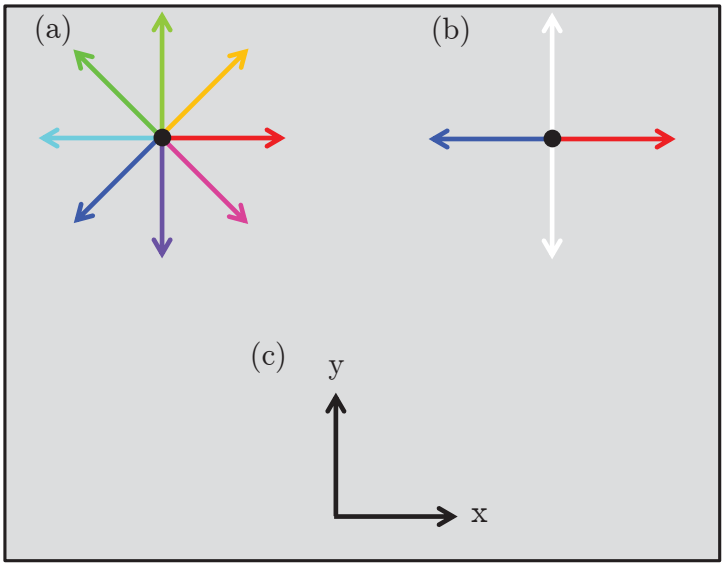

Figure B.1: (a) micromagnetic simulation contrast for simulations in Chapters 2, 5, 6 & 7, (b) micromagnetic simulation contrast for simulations in Chapter 4 and (c) axes for all figures in this thesis unless otherwise specified.